UC Irvine
UC Irvine Electronic Theses and Dissertations

Title

Multiplexing of electrospray sources for space propulsion and physical sputtering

Permalink

https://escholarship.org/uc/item/87z193nc

Author

Grustan Gutierrez, Enric Lluis

Publication Date

2015

Copyright Information

Peer reviewed|Thesis/dissertation

UNIVERSITY OF CALIFORNIA,
IRVINE

Multiplexing of electrospray sources for space propulsion and physical sputtering

DISSERTATION

submitted in partial satisfaction of the requirements
for the degree of

DOCTOR OF PHILOSOPHY

in Mechanical and Aerospace Engineering

by

Enric Lluís Grustan Gutiérrez

Dissertation Committee:
Associate Professor Manuel Gamero Castaño, Chair
Associate Professor Lorenzo Valdevit
Assistant Professor Timothy J. Rupert

2015

Dedication

To

Jessica Ho and my parents

"La paciència és la mare de la ciència"
Catalan proverb

Caminante, son tus huellas
el camino y nada más;
caminante, no hay camino,
se hace camino al andar.

Al andar se hace el camino,
y al volver la vista atrás
se ve la senda que nunca
se ha de volver a pisar.

Caminante no hay camino
sino estelas en la mar.

Antonio Machado
" Proverbios y cantares"

Table of contents

List of figures

List of tables

Acknowledgments

Even if only my name appears on this dissertation I feel that this has been a collaborative effort.

First of all, I would like to thank Prof Manuel Gamero-Castaño for his support and patience during the difficult moments of my PhD. His insight into electrospray atomization and his experimental expertise have been invaluable.

Prof. Lorenzo Valdevit, Prof. Timothy Rupert and Prof. Manuel Gamero-Castaño as members of my committee spent time revising the document and giving valuable suggestions during my Qualifying exam.

Little did I know when I applied to the Balsells Fellowship to which incredible endeavor I was signing up; none of my USA experience would have been possible without the support of Mr. Pere Balsells and the guidance of Prof. Roger Rangel.

A large part of my research has taken place inside the Integrated Nanosystems Research Facility. I would like to take this opportunity to praise their work, especially Mr. Jake Hess, Vu Phan and Dr. Mo Kebaili; everything I know about microfabrication is thanks to them.

I thank AIP Publishing LLC and IMAPS for providing their permission to include copyrighted material as part of my dissertation. Chapters IV andV of this thesis contain material from *Sputtering of Si, SiC, InAs, InP, Ge, GaAs, GaSb, and GaN by electrosprayed nanodroplets* and *Fast etching of microscale structures by bombardment with electrosprayed nanodroplets,* Rafael Borrajo-Pelaez and I are co-authors of these publications, the corresponding author is Prof. Gamero-Castaño. The Balsells Fellowship, the USA Air Force Office Of Scientific Research and the Defense Advanced Research Projects Agency funded my research.

My life as a graduate student definitely improved the day when Rafael Borrajo appeared in our lab, I have the honor of calling him my friend. Luckily for me he is not the only friend that made my stay in Irvine enjoyable, thanks Anna Papió, Michele Rosso, Nicolás Valle, Raúl Díaz, Alfred Grau, Joan Giner, Sergi Pérez, Julius Klein, the San Morosini gang and in general all the Italian and Catalan communities at Irvine. Back home thanks to all Les Berros (Marc Cortina, Ponti brothers, Sara Orgué, Maria Díaz de Quijano, Jordi Castells…) and Marc Contijoch for your support and for making me feel that I have a place waiting for me back in Catalonia.

During my stay in Irvine I not only gained new friends but also a new family, the Ho's made me feel welcome from the very first day and encouraged me through these years, thanks Gail, Lauren and Paul.

In Catalonia my family has always been patient and indulged in my world trotting instincts: Padrina, Mare i Pare gràcies per tot!

Last but absolutely not least thank you Jessica Ho: you are my home far away from home I don't know if this could have been possible without you.

Curriculum Vitae

Enric Lluís Grustan Gutiérrez

2005   B.Sc. in Mechanical Engineering, University of Padova, Italy

2007   M.Sc. in Aerospace Engineering, University of Padova, Italy

2008   B.Sc/M.Sc. in Industrial Engineering, Barcelona Tech

2013-15   Cleanroom Superuser, Integrated Nanosystems Research Facility, University of California, Irvine

2013-2014   Teaching Assistant, Department of Mechanical and Aerospace Engineering, University of California, Irvine

2015   Ph.D. in Aerospace and Mechanical Engineering, University of California, Irvine

FIELD OF STUDY

Microfabrication of arrays of electrospray sources MEMS and physical sputtering of semiconductors

PUBLICATIONS

R. Borrajo-Pelaez, E. Grustan-Gutierrez & M. Gamero-Castaño, "Sputtering of Si, SiC, InAs, InP, Ge, GaAs, GaSb, and GaN by Electrosprayed Nanodroplets", Journal of Applied Physics, 114, 184304 (2013)

E. Grustan-Gutierrez, R. Borrajo-Pelaez & M. Gamero-Castaño,"Fast etching of microscale structures by bombardment with electrosprayed nanodroplets", Proceedings IMAPS 2014 San Diego Conference

Abstract of the Dissertation

Multiplexing of electrospray sources for space propulsion and physical sputtering

By

Enric Lluís Grustan Gutiérrez

Doctor of Philosophy in Mechanical and Aerospace Engineering

University of California, Irvine, 2015

Professor Manuel Gamero Castaño, Chair

The present work explores what can be achieved when the fields of microfabrication and electrospray atomization intersect. The electrospraying of conductive liquids is a well documented technique used heavily for mass spectrometry but also for drug encapsulation or electric propulsion among other applications.

Chapters 2 and 3 of the dissertation focus on the development of a miniaturized array of sixty-four electrospray sources, determining the design requirements and how to adapt them to microfabrication processes. The prototypes response to mass flux and emitting voltage variations is characterized by recording the currents at the emitter, extractor and collector. To determine whether the source can run continuously for prolonged periods of time, it is left operating until malfunction; the maximum life span is 12 hours.

The most advanced prototype undergoes Time-of-flight spectrometry analysis to evaluate its capabilities for satellite propulsion; with resulting mass flux ranging from $2.07 \cdot 10^{-9}$ to $2.81 \cdot 10^{-8}$ kg/s, a total maximum thrust of 34 µN, an I_{sp} varying from 124 to

245s, with specific charge between 697 and 3142 C/kg and a maximum thrust efficiency of 70%.

In the final portion of the document we present the effects of bombarding Si, SiC, InAs, InP, Ge, GaAs, GaSb and GaN with high kinetic energy projectiles from a single emitter electrospray source. We investigate the structure of the damaged surface and sputtered volume by atomic force and scanning electron microscopy and stylus profilometry. The dependance of substrate nature, kinetic energy and projectile dosage on the final topography of the processed slice is discussed together with sputtering rate and yield. The maximum sputtering rates for the technologically interesting SiC and GaN are 220 and 630 nm/min respectively.

Gold, AZ4620 and Shipley 1827 photoresists layers are deposited on a silicon substrate and sputtered to find their adequacy as microfabrication masks. The sputtering rate selectivity between mask and substrate is calculated for different impact velocities; the maximum value for gold is 64.17, at low speeds Shipley and AZ selectivity is virtually infinite. Finally as proof of concept some intricate structures are carved on silicon using AZ4620.

Chapter I

Introduction

T he physics of electrospray atomization are not a recent discovery. Already at the beginning of the past century Zeleny [1], [2] reported on how a conductive liquid surface becomes unstable under an electric field forming a charged spray; later in 1952 Vonnegut & Neubauer [3] obtained monodisperse aerosols. In 1964 Sir G.I. Taylor published one of the most influential works in the field [4] when he first used a physical hypothesis to model the behavior of the electrospray formation. In this same decade some of the first technological applications of electrospray atomization started to appear, the ability of electrospray sources to emit particles at large velocities made them especially interesting as satellites thrusters [5][6]. However, the real technological breakthrough occurred during the 1980's when J.B. Fenn combined electrospray atomization with mass spectrometry for the study of biological macromolecules [7]. While mass spectrometry is the most popular use of electrospray sources there are other recent applications in drug encapsulation [8], combustion [9], physical sputtering [10]–[12], surface engineering [13] and fiber production through electrospinning [14]–[16].

I.1 Microfabricated array of electrospray sources for space propulsion

The early interest that electrostatic spraying gained during the 1960's for satellite propulsion quickly dwindled during the next decade due to: the general budget reduction of

space technology research, the small total thrust they provided (insufficient for the period technology), the high voltage power supplies demanded and the development of the simpler Kaufman ion engines.

The field of micropropulsion began with the popularization of small satellites and the need of another propulsive system, the efficiency of plasma discharge ion thrusters is very low when their input powers is below few kW while small satellites need low thrust (1-100 μN) delivered efficiently at low power. By the end of the 1990's the ability of colloid thrusters to provide low thrust in a very controllable and efficient manner (the typical thrust of a single emitter is of the order of a fraction of μN) made them an excellent candidate for miniaturization[17].

The range of thrust that standard colloid propulsion can provide is optimal for a wide range of satellite uses such as attitude control but the low flux of mass ejected that limits the maximum thrust makes it unsuitable for primary propulsion. For this purpose the characteristic low thrust of the single emitter must be scaled up to magnitudes of hundreds of μN [18]. In order to achieve this improvement in total thrust the intrinsic physical properties of electrospray atomization have to be taken into account; electrospray sources emitting particles with the charge to mass ratio required for space propulsion produce a narrow thrust. Therefore a reasonable scaling up of the system implies the use of multiple sources.

When the multiplexing of emitters is achieved by standard fabrication techniques [6], [18] the density of emitters per unit area is small; and if the thrust requirements demand for greater output or the area available is small (microsatellites or CubeSats) other fabrication approaches must be used. Since the abandonment of colloid propulsion

research during the 1970's the fields of electrospray science and microelectromechanical systems (MEMS) have fully matured. Electrospray atomization nature is better understood due to the research triggered by its use in mass spectrometry and the production of microscopic structures on silicon has become standard practice. The pairing between electrospray atomization and microfabrication technology to obtain large and dense array of emitters has become the natural approach [19]–[22].

Even if space propulsion is the driving force behind the research of microfabricated sources, it is not the only field that would benefit from it. Electrospray atomization is an excellent source of charged nanoparticles, its limiting factor being the small flux produced by a single emitter. An electrospray source delivering substantially larger mass flow rates could be used for physical sputtering [11], [12], mass spectrometry [7], microcombustion [23], insulin creation [24], synthesis of metallic glasses [25], production of ZnS particles [26], drug encapsulation [8] and photovoltaic cell production [27].

Chapter 2 introduces the design challenges to consider when fabricating an operational array. Some of the key parameters discussed are: the geometric aspect ratio of the emitters (emitter diameter against height ratio) responsible to set the minimum onset voltage and the flow impedance. The ability to create large impedance is one of the novelties of this dissertation, we developed a microfabrication process to carve a system of microfluidic channels onto the silicon substrate, this system guarantees that the liquid flux is highly controllable and its distribution uniform across the emitter array. The ideal design is contrasted with the fabrication limits to find the optimal operational compromise.

In chapter 3 four different prototypes (Proof of Concept, HC-1, HC-2 and HC-3) are tested. The performance of the devices is analyzed against increasing flow rates and

extracting voltages, an emphasis is made to minimize the fraction of particles trapped at the extractor. This fraction is well below 2% for HC-2 and HC-3 and to characterize whether this value is low enough to continuously operate the sources are subjected to an endurance test where the electrospray current is recorded for several hours. TOF analysis is also used on HC-3 to compute the important space propulsion parameters of thrust, specific impulse and thrusting efficiency at different liquid flows.

I.2 Physical sputtering by nanodroplet bombardment

Reactive plasma etching processes such as Reactive Ion Etching (RIE) or Deep Reactive Ion Etching (DRIE) are very efficient at carving structures on substrates susceptible to chemical attack such as the most popular semiconductor in MEMS, Silicon. Yet, the growing fields of microelectronics such as HEMTs, MESFETs, LEDs or JFETs rely on the use of semiconductors such as GaAs, SiC or GaN [28]–[34] which are resistant to chemical attack. The etch ratio of the traditional reactive procedures RIE and DRIE, when used for these materials, are significantly slower than for reactive substrates and close to those of physical sputtering methods[35]–[38].

The methods used to raise the etching rate for plasmas consist of complicated chemical multi-step processes or the use of high power plasmas and accelerating voltages. One of the main reasons why the etching rate is better at large powers is that the species in the plasma impact the surface at faster velocities and the material is removed by mechanical means. It is clear that if at some point, kinetic impact is the only contributor to the substrate etch,

specific physical sputtering systems such as Ion Beam Milling (IBM) or Gas Cluster Ions (GCI) can also be used for this purpose.

The size of the projectile has a strong effect on the physical sputtering rate: large molecules are much more efficient sputtering elements than monoatomic particles, their target penetration is much smaller thereby transferring their kinetic energy over a shallow volume.

Linear collision cascade theory explains the sputtering systems for atomic particles[39], the atoms ejected from the slice originate from a very thin surface layer (~5Å) and are due to indirect effects produced by the projectile instead of head-on collisions. More energetic projectiles penetrate deeper in the slice but their sputtering yield does not increase significantly. According to molecular dynamics simulations the sputtering produced by larger particles such as gas cluster ion beams and electrosprayed nanodroplets are driven by high density collision cascade and thermal evaporation[40], [41], as a result of these different mechanisms the sputtered material from the impact of a particle containing n atoms is greater than bombarding the target with n monoatomic projectiles.

Finally, larger projectiles have lower charge to mass ratios ξ. From Child-Langmuir law [42] we know that the mass rate of charged particles is proportional to $V_A^{3/2}$ (V_A is the accelerating voltage between two electrodes) and inversely proportional to the square root of ξ.. These physical arguments explain why the most limiting element of IBM for physiscla sputtering is the use of monoatomic projectiles (usually Argon); the mass flux is low because of the high charge to mass ratio and it cannot be modified by augmenting the acceleration voltage as it that would create problems of contaminating the substrate by

indentation of Ar atoms. It is believed that IBM can be used efficiently at rates below 10nm/min[43].

GCI has the same working principles as IBM but instead of monoatomic Ar ions uses clusters of atoms that later are charged and accelerated (most common GCI use clusters containing 2000 Ar atoms)[44]. This greatly increases mass output and at the efficency of the kinetic energy transfer. Gas cluster ions have a diameter limited to the few nanometers, the introduction of electrospray nanodroplets provides physical sputtering of a source of large and flexible projectile size. The diameter of the charged droplets can be controlled from the nanometers to macroscopic dimensions.

Chapter 4 presents the etching rates of electrospray bombardment on Si, SiC, InAs, InP, Ge, GaAs, GaSb and GaN and compares them to the other existing methods. The influence of accelerating voltage and projectile dosage is also discussed. In chapters 5 and 6 gold and photoresists Shipley 1827 and AZ4620 are used to mask certain regions of the target to selectively carve the desired slice.

I.3 Fundamentals of electrospray atomization

Electrospray atomization is based on the use of strong electric fields on capillary jets, the electric field imparts charge at the surface of the naturally occurring droplets. The simplest electrospray source consists of two electrodes: emitter and extractor. The emitter is usually a capillary or needle connected to a liquid reservoir while the extractor is a conductive surface placed perpendicular respect to the emitter at a set distance. A voltage difference is maintained between electrodes creating an electric field among them, the boundary
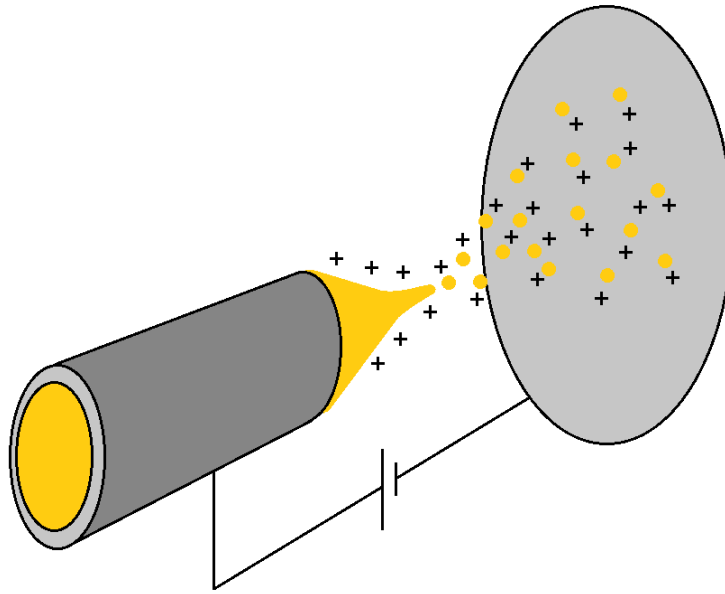
Figure 1. Schematics of electrospray atomization

conditions imposed by emitter and extractor placements result in a very intense electric field at the tip of the capillary.

Without an electric field the liquid flowing towards the end of the capillary would form a meniscus but under the stress of an electric field its shape is distorted and the convexity is greater, if the field is strong enough at the apex of the structure charged particle detach and accelerate towards the extractor [45]. The schematics of the electrospray source are shown in figure 1.

There are several modes in which the particles are discharged [46], [47] but probably the most interesting for its ability to produce charged nanoparticles with narrow charge to mass ratio distributions is what Cloupeau & Prunet-Foch named the Cone-Jet mode. In this spraying mode the main part of the misshaped meniscus deforms into a cone, around the apex, the cone opens into a jet of microscopic diameter; after attaining a certain distance,

instabilities break the jet into charged droplets [48]. For liquids with high conductivity K>0.8S/m ions evaporate at the apex region [49]–[51]. If the liquid has an extremely high conductivity as in the case of liquid metals [52] or the flow rates are low [53], the jet closes to itself emitting only ions.

In 1882 Lord Rayleigh modeled for first time the maximum charge a droplet of certain diameters can hold without undergoing a Coloumbic explosion [54]. If one considers the surface tension stress in a spherical drop

$$\sigma_\gamma = \frac{2\gamma}{r} \tag{1}$$

where γ is the surface tension and r the radius of the droplet and then the electric stress in a equipotential liquid

$$\sigma_E = \frac{1}{2}\varepsilon_0 E_n^2 \tag{2}$$

ε_0 is the vacuum permittivity and E_n the electric field normal to the surface of the droplet, equal to

$$E_n = \frac{Q}{4\pi\varepsilon_0 r^2} \tag{3}$$

substituting (3) in (2) and equaling it to (1), one obtains the Rayleigh limit, the maximum charge a droplet of radius r can hold

$$Q^2 = 64\gamma\pi^2\varepsilon_0 r^3 \quad . \tag{4}$$

In 1964 sir G.I. Taylor[4], was able to explain the conical shape of the electrospray meniscus by considering the interaction between electrostatic and surface tension forces at the surface of the meniscus, and simplified the problem by considering an hydrostatic and electrostatic system. In this case the surface stress on a given point of the cone is

$$\sigma_y = \frac{\gamma \cot(\alpha_T)}{r} \tag{5}$$

the electric stress is the same as in (2), and the electric field has to be obtained from the potential. For a conic behavior the electric potential can be expressed in terms of the Legendre polynomials

$$\Phi(r,\theta) = a r^\nu P_\nu(\cos\theta) \tag{6}$$

and derivating to obtain the electric field

$$E_n = \frac{1}{r} \frac{\partial \Phi}{\partial \theta} = a r^{\nu-1} \sin\theta \frac{dP_\nu}{d(\cos\theta)}(\cos\theta) = a r^{\nu-1} f(\theta) \quad, \tag{7}$$

then on the surface of the Taylor cone we will have that

$$\frac{\gamma \cot(\alpha_T)}{r} = \frac{1}{2} \varepsilon_0 a^2 f(\pi - \alpha_T)^2 r^{2\nu-2} \tag{8}$$

to guarantee that the stresses are equal at any point (r, α_T) of the cone the order of the Legendre polynomial needs to be 0.5 and the potential on the cone is

$$\Phi(r, \pi - \alpha_T) = a r^{1/2} P_{1/2}(\cos(\pi - \alpha_T)) \tag{9}$$

and to have a constant potential for any distance from the cone apex

$$P_{1/2}(\cos(\pi - \alpha_T)) = 0 \tag{10}$$

with a single solution when α_T=49.29°. These results shed some light on the problem and gives a good approximation of the shape of the meniscus on the region far from the apex where the hydrostatic and perfect conductivity assumptions hold. When the space charge is significant the angle of the cone is reduced with respect to the theoretical Taylor's angle, the electric "pressure" from the charges flattens the cone.

Since these earlier results several efforts have been made to find a more complete model of the Taylor cone in equilibrium structure and in which conditions the cone is

established [55]–[59]. The behavior of the apex in emitting cone-jets to determine the diameter of the jet and the resulting droplets as well as the current emitted is of special importance. The diverse physical models developed by Fernandez de la Mora & Loscertales [60] and an especiflic model of the one of Gañan Calvo[61] produce the widely accepted scaling law for cone-jet currents

$$I \propto Q^{1/2} \quad .$$
(11)

Gañan Calvo current is defined by

$$I = (\gamma K Q)^{1/2}$$
(12)

while Fernandez de la Mora reports

$$I = g(\varepsilon)\left(\frac{\gamma K Q}{\varepsilon}\right)^{1/2}$$
(13)

where $g(\varepsilon)$ is a function of the permittivity which value is found empirically and can be approximated to [62]

$$g(\varepsilon) = \begin{Bmatrix} 0.45\,\varepsilon\,;\,\varepsilon < 40 \\ 18\,;\,\varepsilon > 40 \end{Bmatrix}$$
(14)

However he different physical approaches result in dissimilar scaling laws for the jet diameter,

$$d_{jet} \propto Q^{5/6} \quad \text{and} \quad d_{jet} \propto Q^{1/3}$$
(15)

for Gañan Calvo and Fernandez de la Mora & Loscertales respectively.

Design and microfabrication of an array of electrospray sources

An array of electrospray sources operating uniformly in the cone-jet mode presents several design challenges. The geometric aspect ratio of the emitter (the ratio between height and thickness) must generate an electric field at the tip that is strong enough to form a stable Taylor Cone, this combined with the distance between emitter and extractor electrodes determines the minimum operating voltage (on a well designed source the voltage is smaller than the breakdown limit of vacuum).

The maximum emitter density is limited by two elements, the perturbation that the presence of neighboring emitters create on the electric field and the apertures of the extractor. To let the charged droplets hurtle outside the source some apertures must be placed on the extractor. Although narrow openings offer the opportunity to fabricate a dense population of sources, they will obstruct a large fraction of the electrospray beam.

Finally, it is imperative that the hydraulic impedance of each emitter is carefully tailored; the pressure drop across the array must remain constant to assure that all sources are engaged in the same electrospraying mode.

These design needs are discussed in detail in this chapter together with the microfabrication constrains to determine the final layout of the prototypes. Finally the fabrication and assembly strategies and work flow are outlined.

II.1 Preliminary design

To test the capabilities of the Integrated Nanosystems Research Facility (INRF), especially in regards to the aspect-ratio the DRIE system can attain uniformly, we fabricated a 9 by 9 matrix of emitters; each one with an external diameter of 70 μm, an inner diameter of 40 and a height of 300 μm and rises from the center of a well with 0.9 mm in diameter and a depth of 300 μm. Placing the emitters inside a depression isolates them electrically from the influence of the surrounding emitters, the radius of the well is large enough to have subtle influence on the electric field intensity at the tip. The extractor thickness is 350 μm, the diameter of the extractor orifice is 0.9 mm. The distance between the emitter and extractor is 250 μm. Figure 2 illustrates this basic configuration.
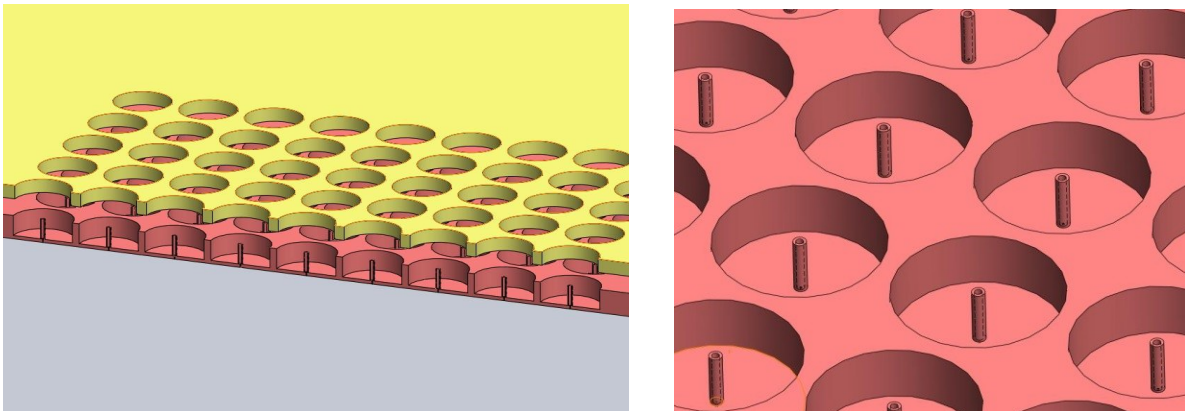
Figure 2. Left: Cut section of the preliminary design, emitter die (magenta) and extractor (yellow). Right: detail of the emitter array.

II.2 Fabrication of the emitter array

The emitters are carved on a highly doped Si wafer using an STS Advanced Silicon Etch DRIE Bosch system. The main challenge lies in microfabricating the array of emitters while obtaining vertical features and smooth surfaces. Bosch systems carve anisotropic structures by alternating between opposite steps: etching and passivation. During the etching step a flux of SF_6 and O_2 gases is introduced into the chamber where the wafer is located. Then, plasma is formed releasing F and O radicals. The plasma is later accelerated towards the silicon wafer vertically attacking the exposed surfaces. Some silicon is etched by physical sputtering of the ions impacting the surface but the main driving etching factor is the chemical recombination of the fluorine radicals with silicon. The addition of O_2 keeps the concentration of F radicals high (avoiding the recombination of SF_n with F), while also helping to maintain vertical and smooth surfaces[63].

During the successive step an inert substance is deposited on the recently etched surface; the INRF DRIE uses C_4F_8, a substance similar to Teflon. This product protects the exposed walls from chemical attack of the fluorine radicals but it is sputtered away by the direct impacts of ions on the perpendicular surfaces. The standard recipes available on the DRIE machine are presented below.

Table I. Standard DRIE recipes for STS ASE system at INRF

| | Process A | | Process B | |
	Etch	Passivation	Etch	Passivation
Time [s]	7	6	14	7
C_4F_8 [sccm]	$15 \rightarrow 0$	85	0	85
SF_6 [sccm]	130.0	0	130.0	0
O_2 [sccm]	13.0	0	13.0	0
Coil Power [W]	600	600	700	0
Platen Power [W]	15.0	15.0	20.0	20.0
APC	70°	70°	83.5°	83.5°

The flow of SF_6, O_2 and C_4F_8 control the different gas concentrations during the process; APC (Automatic Pressure Control) controls the exhaust valve angle, at smaller angles more exhaust gas flux can exit the chamber lowering the process pressure; coil power generates the plasma and the platen power is responsible for accelerating it towards the wafer. These parameters will affect the etching rate, smoothness, uniformity and angle of the profiles. Aggressive recipes over-etch the features creating angles greater than 90°, while on the other hand if the recipe tends to be too conservative the angle of the wall will be acute and we can also induce the appearance of silicon grass (silicon grass are pocket of un-etched silicon forming undesired needle-like structures with an appearance similar to grass), both undesired effects can be observed in figure 3.

The first carving test of the emitters array using Process A until a depth of 300 μm is reached results in a general loss of the needles along the array due to over etching. Using Process A as the starting point, different strategies were devised to obtain a recipe that could microfabricate an emitter while avoiding over-etch or the presence of silicon grass.
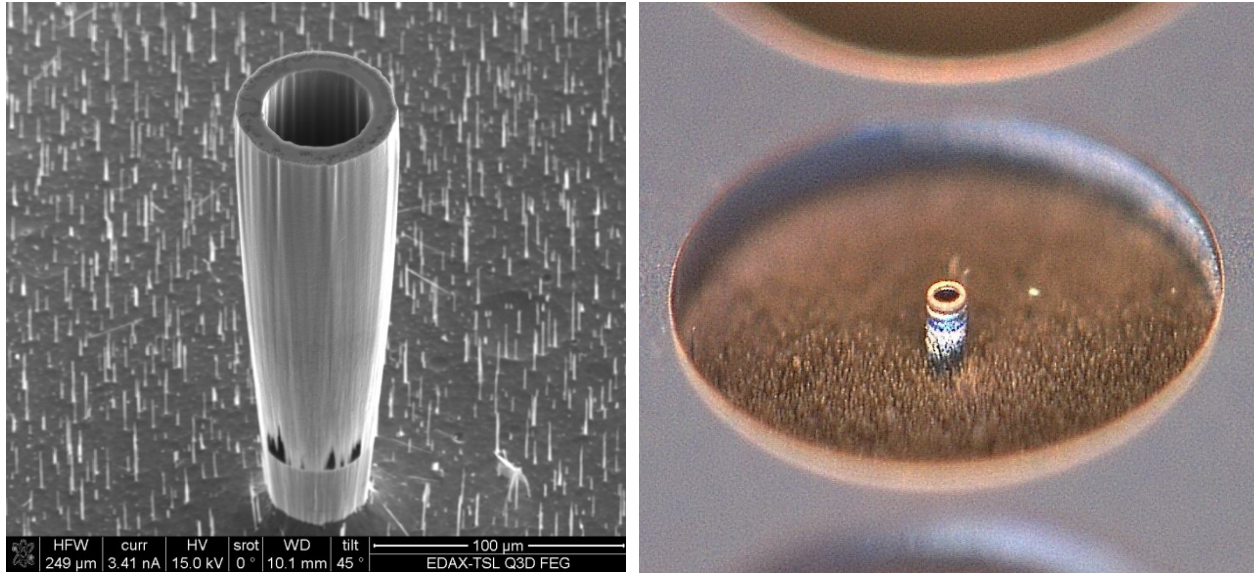
Figure 3. The left image shows the over-etch of an emitter structure. Some small pockets of silicon grass are present but unlike the image at the right the grass density is not enough to mask the surface.
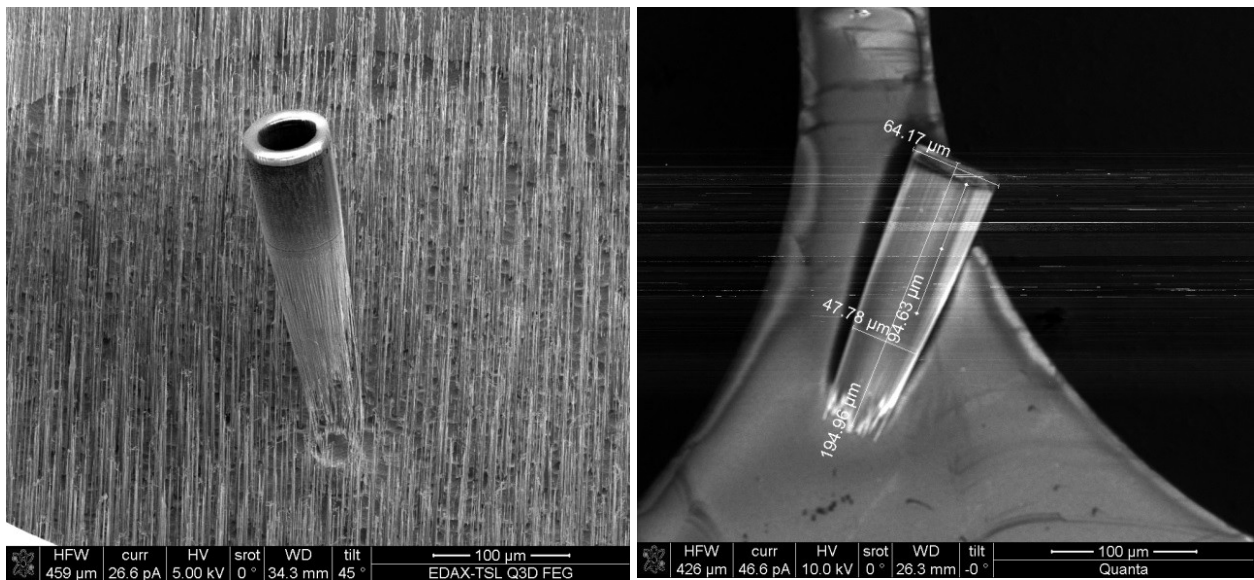
Figure 4. An over etched emitter barely stands up on a field dense silicon grass (left). A broken emitter laying flat on the surface of the wafer, after it has been etched for 100 µm the profile turns inwards (right).

Using the strategies found in [63]–[66] we modified the platen etch power, etch/passivation time ratio, APC aperture of the original recipe, in some cases we also included a flux of Ar. The fabrication outcome of each parameter change is summarized in Appendix A. The crucial discovery in the recipe development is the one observable in figure 4; for the desired high aspect-ratio and depth of the geometry the best that the DRIE system offers is an a priori paradoxical result. Broken needles (results of over etch) are present simultaneously with a heavy density of silicon grass. Meanwhile the angle of the emitter profile abruptly increases after the depth reaches 100 μm.

These facts leads us to conclude that at least some of the over etching is caused by the ions bouncing on the walls of the previously etched features thus creating a positive profile almost independent of the parameters controllable with the DRIE. Therefore the minimum diameter of the emitters is bounded by the DRIE system and the geometry needs to be altered. The diameter and height of the emitters will change according to the prototypes, but we found that the minimum diameter that is possible to carve effectively is 100 μm.

II.3 Flow resistance. Microfluidic channels

Even if an array of electrospray emitters could work by feeding each emitter directly from the ionic liquid reservoir, the introduction of enhanced flow impedance to increase the pressure drop needed for the liquid to flow offers some benefits.

First let's consider how the flux feeding an emitter (or array) is usually controlled. The ionic liquid is stored in a pressurized reservoir, a capillary connects it with the spraying

needle (figure 5). Ideally, the pressure difference between reservoir and the needle surroundings (ΔP) draws the fluid towards the tip at a fix volumetric flux (Q)

$$Q = \frac{\Delta P}{R} \qquad (16)$$

where R is the flow resistance [67]. If the liquid resistance is negligible any small pressure perturbation will produce large liquid flux variations making the operation difficult to control, potentially flooding the emitter array. The introduction of large flow impedance not only minimizes the effect of pressure fluctuations but offer a higher flux resolution with respect to the pressure.

Another factor to consider is the pressure drop due to surface tension. Once the electrospray is set we know that a meniscus is present at the tip of the emitter, surface tension forces create another pressure drop (ΔP_{ST}) proportional to the curvature radius (r) and the surface tension (γ)
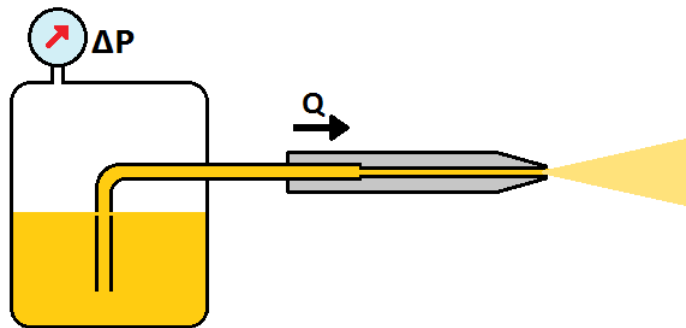
$$\Delta P_{ST} \propto \frac{\gamma}{r} \qquad (17)$$

Figure 5. Set-up of the flux control. The liquid is drawn from a reservoir to the needle by a pressure difference ΔP setting a flux Q

then the flux is effectively controlled by

$$Q = \frac{\Delta P - \Delta P_{ST}}{R}$$ (18)

and in case that of perturbations on the shape of the cone the flux variation is

$$\delta Q = \frac{-\delta \Delta P_{ST}}{R}$$ (19)

we cannot control ΔP_{ST} so to minimize the fluctuations a high resistance is suitable.

The placement of the impedance is also relevant; if all the emitters are perfectly equal the flux along the array will be uniform but small fabrication defects can carry significant imbalances. Doing another difference analysis the relative flux variation per emitter due to resistance variation is

$$\frac{\delta Q_{emitter}}{Q_{emitter}} = \frac{-\delta R_{emitter}}{R_{emitter}}$$ (20)

If we consider a cylindrical inner microfluidic channel the R$_{emitter}$ is

$$R_{emitter} = \frac{8 \mu L_{emitter}}{\pi r_{emitter}^4}$$ (21)

[67] where μ is the fluid viscosity, $L_{emitter}$ the emitter length and $r_{emitter}$ its radius, then the relative variation is

$$\frac{\delta Q_{emitter}}{Q_{emitter}} = \frac{-\delta L_{emitter}}{L_{emitter}} + 4 \frac{\delta r_{emitter}}{r_{emitter}}$$ (22)

As we can see, the fabrication defects are very taxing in the case of the diameter of the emitter, a 5% error will create a 20% flux variance. Therefore after the liquid has branched to feed every needle the resistance deviation due to fabrication defects must be much smaller than its nominal value.

Krpoun and Shea [68] and later other groups [69] solve this problem by filling each emitter with microbeads. This is not an easy task, one has to guarantee that each emitter is filled with a similar amount of beads creating a complex fabrication process [70], with emitters non uniformly filled [21], [71], [72]. It is also known that after long operating times that some of the beads separate. For these reasons Shea recently propose to use narrow channels on the emitter conduct [22], while this solution is more sturdy and efficient it ties the impedance to the emitter geometry, and the ratio between flow and diameter variance due to microfabrication defects remain 4.

We followed another approach forcing the ionic liquid through a system of microfluidic channels before each emitter. The pressure drop for each emitter due to the impedance of a rectangular channel is [73]:

$$R = \frac{12\mu L}{w h^3} \left[1 - \sum_{1,3,5}^{\infty} \frac{192 h}{w (n\pi)^5} \tanh\left(\frac{n\pi w}{2h}\right) \right]^{-1} \tag{23}$$

where *w>h* are the dimensions of the channels.

Two designs were tested, in the first one 10x10 μm channels 1200 μm long that produce the main pressure drop sprout from a 50 μm wide and 50 μm deep conduct (Figure 6).
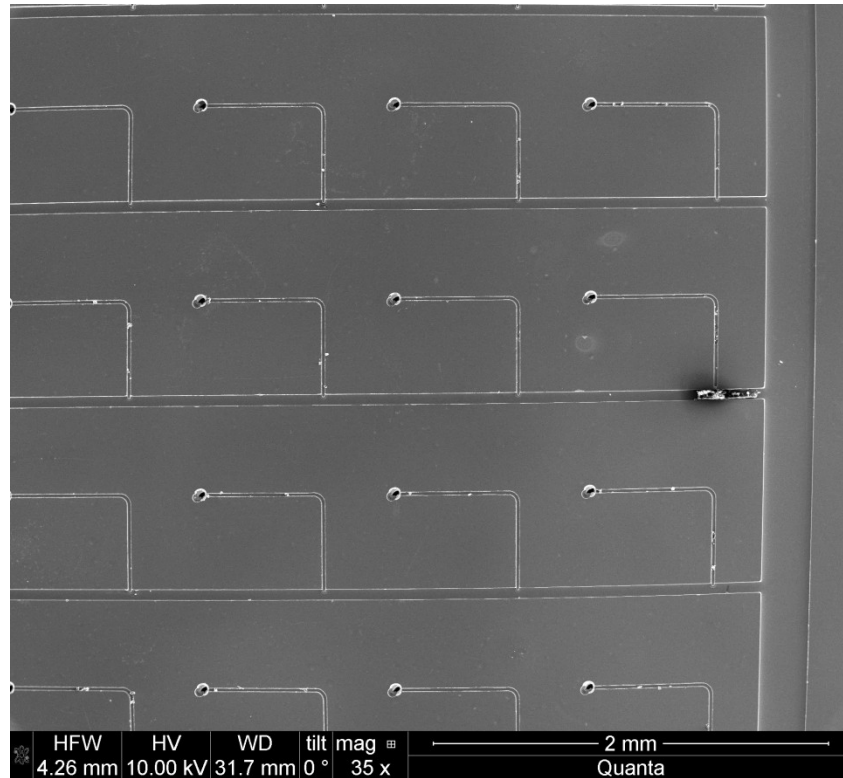
Figure 6. Detail of the array of 10 by 10 μm channels. Dust has deposited in one of the channels while loading it into the SEM

This method can only be achieved by twice etching the backside of the wafer. To simplify the fabrication to a single etching step a single channel systems of the same depth is sketched. The main channel connected to the liquid reservoir branches out successively until it forms a tree-like structure with 64 20 by 20 μm and 7500 μm length channels. This structure has the advantage that each branch measures the exact same length (figure 7). The channels are sealed by the anodic bonding of the silicon substrate to a borofloat wafer.
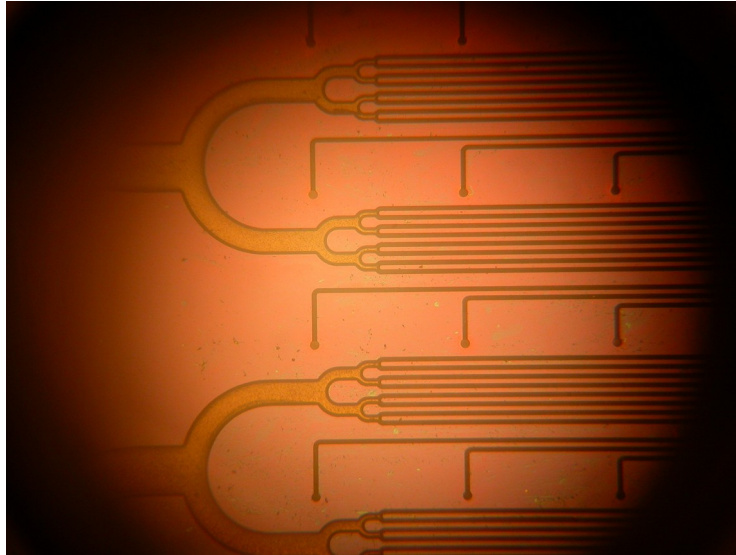
Figure 7. Detail of the branched structure, from the reservoir the channels are divided in two until 64 individual branches form.

The ionic liquid used is the 1-ethyl-3-methylimidazolium bis(trifluoromethylsulfonyl) imide (Emi-Im) with its physical properties shown in Table II. The flow resistance of the microchannel is $5.07 \cdot 10^{17}$ Pa·s/m³ or $3.80 \cdot 10^{15}$ Torr·s/m³.

Table II. Properties of ionic liquid Emi-Im. Molecular mass m_l [amu], density ρ [kg/m³]; surface tension γ [N/m], viscosity μ [cP] and conductivity K [S/m] from [85], [86]

Formula	m_l	ρ	γ	μ	K
$C_8H_{11}F_6N_3O_4S_2$	391.3	1520	0.035	38	0.88

II.4 Extractor fabrication

Once the extractor dimensions are decided its fabrication does not present significant difficulty; we begin with a highly doped double polished [100] and 250 μm thick silicon

wafer that undergoes a standard RCA-1 clean and a 30' dehydration process at 120°C; figure 8 (1). Afterwards a photolithographic process transfers the 0.9mm aperture pattern onto the AZ4620 photoresist layer (2). Finally the wafer is etched through using DRIE, the photoresist is stripped and the wafer is cleaned in a Piranha bath (3).
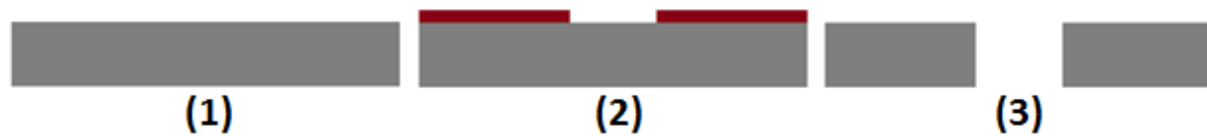
Figure 8. The silicon wafer is first cleaned under an RCA-1 bath (1), then the aperture pattern is transferred to the surface using photoresist (2) and is etched through in the DRIE (3)

In later iterations the extractor is slightly tweaked to allow its direct integration with the emitter dice and the fabrication process remains similar to the aforementioned one. After the initial cleaning process and dehydration (1) the double polished highly doped 1 mm thick silicon wafer is patterned with the 0.9 mm apertures on a AZ4620 photoresist layer (2), then etched on the DRIE until a depth of 275 μm is reached, the photoresist is then stripped and the wafer cleaned (3). On the back side large openings that clear the whole area of the emitter dice are patterned with with a thick layer of AZ4620 (4) etched for a depth of 750 μm (5) and finally cleaned in a Piranha bath (6).
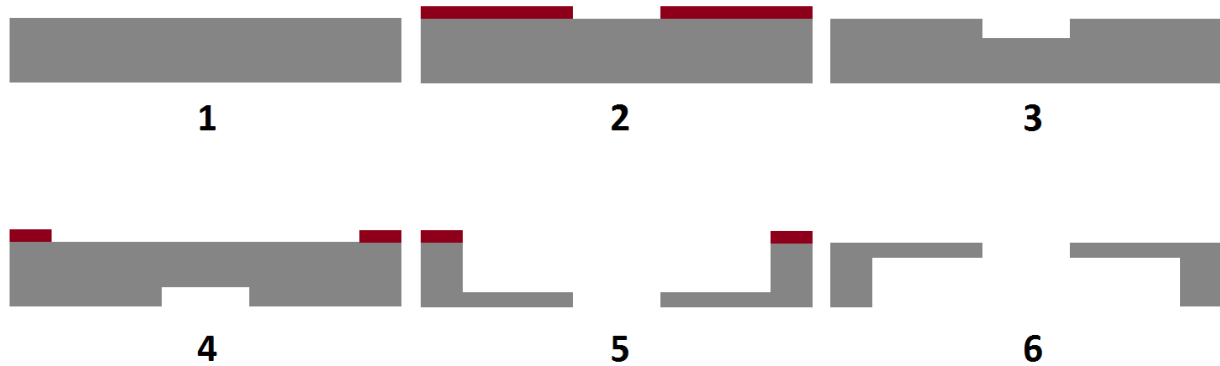
Figure 9. The silicon wafer is first cleaned under an RCA-1 bath (1), then the aperture pattern is transferred to the surface using photoresist (2) and is etched for 275 μm in the DRIE (3). Next, the wafer is flipped and the clearance pattern is developed (4) and is then etched until the remaining thickness is 250 μm (5) and cleaned (6),

II.5 Emitter array fabrication

As we have seen the emitter fabrication is critical. The emitters must be sturdy enough to withstand the electrospray for prolonged periods of time while the microfluidic channels must be as uniform as possible.

After a RCA-1 clean (1) the backside of our double polished side silicon [100] 4 inch and 450 μm thickness wafer is patterned with Shipley 1827 photoresist with the channels responsible for the hydraulic impedance (2). In the next step (3), the channels are carved to a total depth of 20 μm using DRIE and the photoresist is stripped. To protect the channels from damage and to smooth any small defect in the channels the substrate is steamed oxidized at 1100°C for 2 hours growing a layer of 1 μm of Silicon Dioxide (4). The wafer is

23

flipped and a 4 μm layer of plasma enhanced chemical vapor deposition (PECVD) oxide is deposited on the front surface (5). Then, the emitter pattern is transferred to a AZ4620 layer (6), the oxide layer layer is etched using RIE with a final dip in hydrofluoric acid (7). After stripping the photoresist with the emitter pattern a fresh AZ4620 coat is applied and developed to expose the emitters' center hole (8). To account for the slower etching rate of the more narrow structures the holes are etched for 250 μm by means of DRIE and the photoresist is removed (9). Then, the wafer undergoes its last DRIE etch to carve the 300 μm tall emitters (10). Finally the oxide layers are removed on a 20% hydrofluoric acid bath (11).
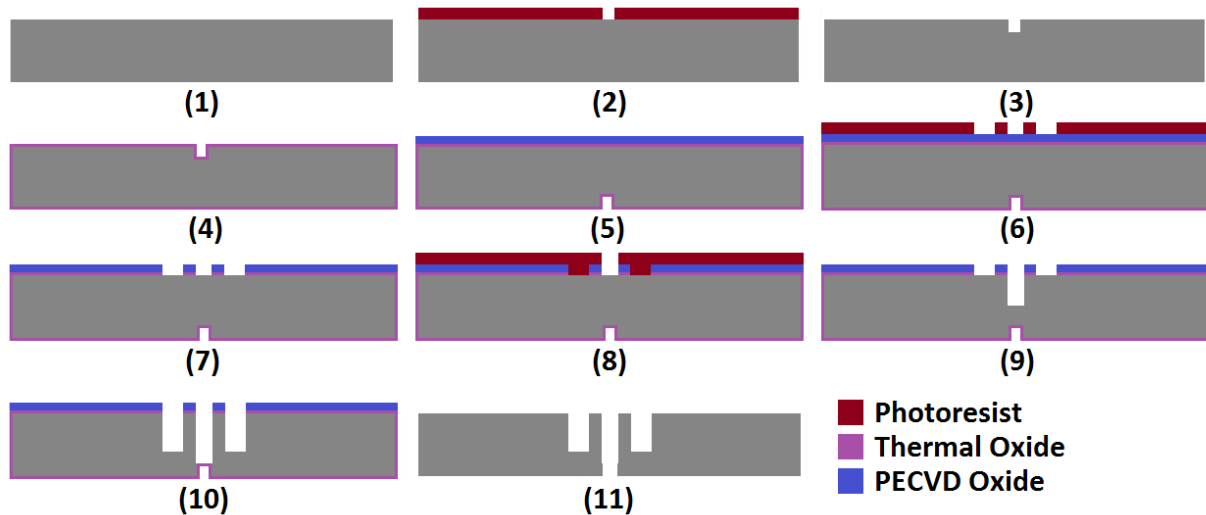
Figure 10. The silicon wafer is cleaned (1), then the channels pattern is transferred to a Shipley 1827 layer (2) and anisotropically etched for 20 μm (3), the wafer is oxidated, (4) flipped and 4μm of PECVD oxide deposited (5) the emitters are patterned (6) and both layers of oxide removed (7) the central hole is pre-etched (8), (9) and then carved for 300 μm (10). Finally the oxide is removed (11).

II.6 Glass cover fabrication

The glass covers seals the microfluidic channels and is where the silica capillary bringing the ionic liquid from the reservoir is fixed. The process flow is the following: after a Piranha clean (1) the borosilicate substrate is patterned with AZ 4620 photoresist (2). Its surface is then deposited with a nickel layer on a E-beam evaporator and then placed under an acetone bath for lift-off (3). Steps (1) (2) and (3) are repeated on the back side of the wafer (4), the slice is then placed on a 49% hydrofluoric acid bath to etch it through (5). Nickel is stripped in a nickel etch bath and the wafer is cleaned. Finally the hole for the silica thread is rectified mechanically with a diamond precision tip (6) and cleaned again in a Piranha bath.
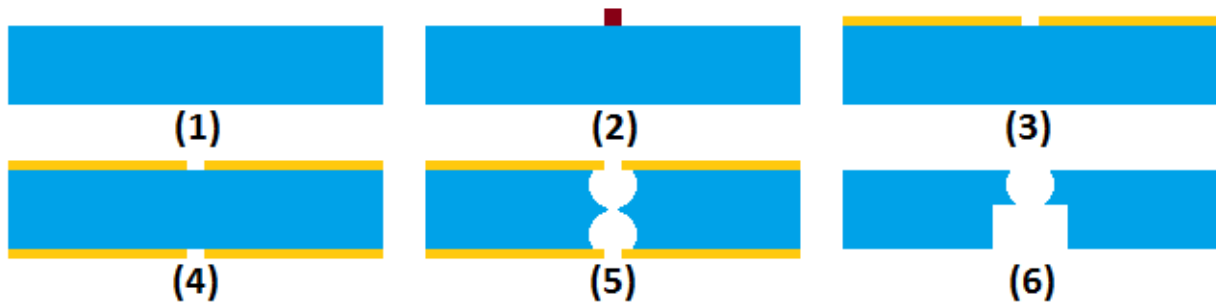
Figure 11. The clean Borofloat wafer (1), then the orifice masks are deposited on the surface by lift-off (2), (3) steps (1), (2) and (3) are repeated on the back side (4) and the glass is etched through in a 49% HF solution (5), lastly the hole is rectified mechanically and the wafer is cleaned (6).

II.7 Electrospray source head assembly and packaging

An often overlooked stage of MEMS fabrication is the assembly and packaging of the finished component; however, an incorrect assembly might render the final product unusable. The most critical feature for the electrospray source device is the proper alignment of both electrodes, the emitters and extractor apertures must be concentric. The extractor and emitter array of the earlier prototypes are held together mechanically allowing to change their distance and is also useful to observe the consequences of long operation. Further refinements of the design included the integration and permanent bond on the chip level of all parts.

Separable extractor and emitters models

Figure 12 shows how the channels carved on the back side of the emitter array die are sealed by the glass cover; the thoroughly cleaned emitter and glass dice (1) are aligned and anodically bonded by heating them up to 300°C and imposing a voltage difference of 0.5 kV between the bonding electrodes (2). When the bond is complete and the wafers returned to room temperature the silica capillary is set in place and fixed. To fix the silica capillary to the glass die different approaches have been used, in earlier stages the capillary was placed on the groove created on the borosilicate and then glued with a small amount of epoxy (3), unfortunately this task is delicate and it is prone to failure, the capillary jumps out of the groove and the epoxy leaks towards the microfluidic structure resulting in total failure of the device. To circumvent this problem, in posterior assemblies a two part in-house built

microfluidic port was used, removing the epoxy application from the proximity of the liquid input (Figure 15).
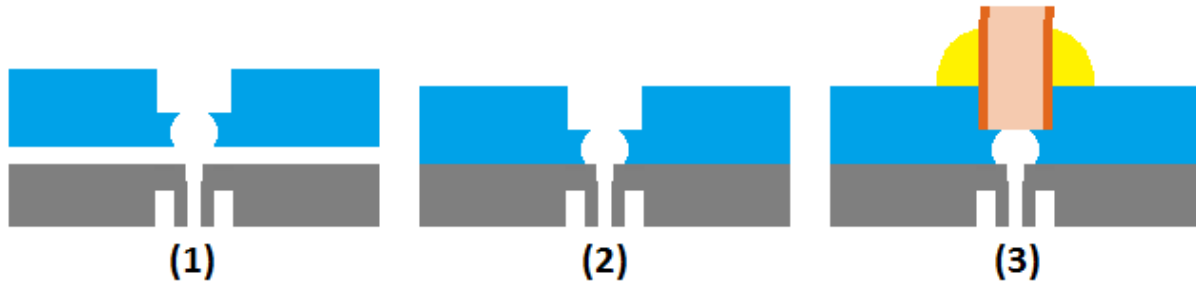
Figure 12. The clean silicon and glass dice are aligned (1), and held permanently together by anodic bonding(2) the silica capillary connecting the head to the reservoir is fixed to the thruster head (3).
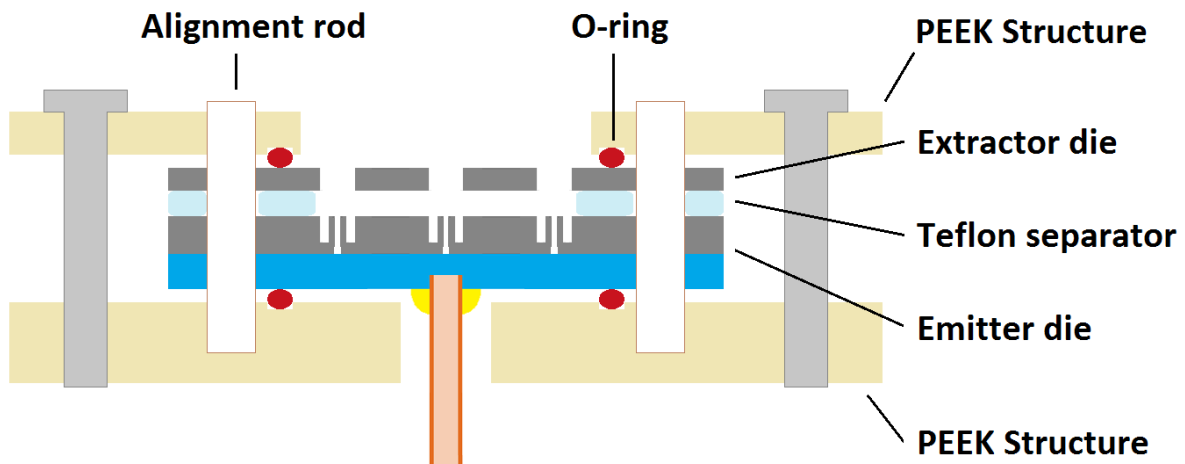
Figure 13. Extractor and emitter dice are compressed by a PEEK structure, a Teflon sheet separates both electrodes. Soft O-rings are used to make the contact between the dice and PEEK. The alignment is done by 4 Teflon rods.

Figure 13 presents the complete thruster head package; the glass-silicon emitter array, Teflon separator and extractor are compressed together by an in-house produced PEEK structure. Neither extractor nor emitter dice directly touch the PEEK surface, instead both sit on two rubber O-rings. During the compression of the components four Teflon rods are used for alignment and a torque wrench imposes a uniform force for each screw.

The silicon parts are brought in electrical contact with the high voltage power supply by compressing a Balseals Inc. steel spring between the electrode and a metallic screw connected to the power supply. Figure 14 shows the whole thruster package for two different versions of the separable emitter models.
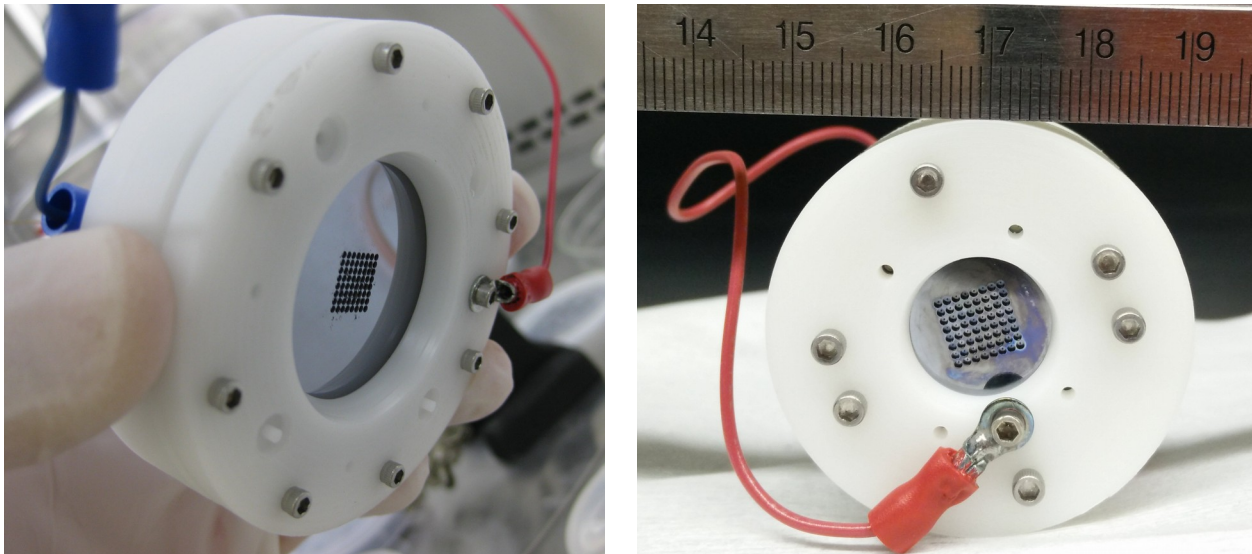
Figure 14. Two fully assembled electrospray sources heads. Left: The total diameter is 3.5" (9 cm), note the electric connections and 2 Teflon alignment rods are still in place. Right: Holder for a smaller dice, the total diameter is 1.6" (4 cm).

II.8 Integrated electrospary source head

Drawing from the insight gained testing the previous versions a fully integrated device is assembled. The etched and cleaned emitters and borofloat dice are aligned (1), put in contact and heated before imposing a voltage difference between them to form an anodic bonding at the contact interface (2). Then the cleaned dice with the extractor (3) is aligned
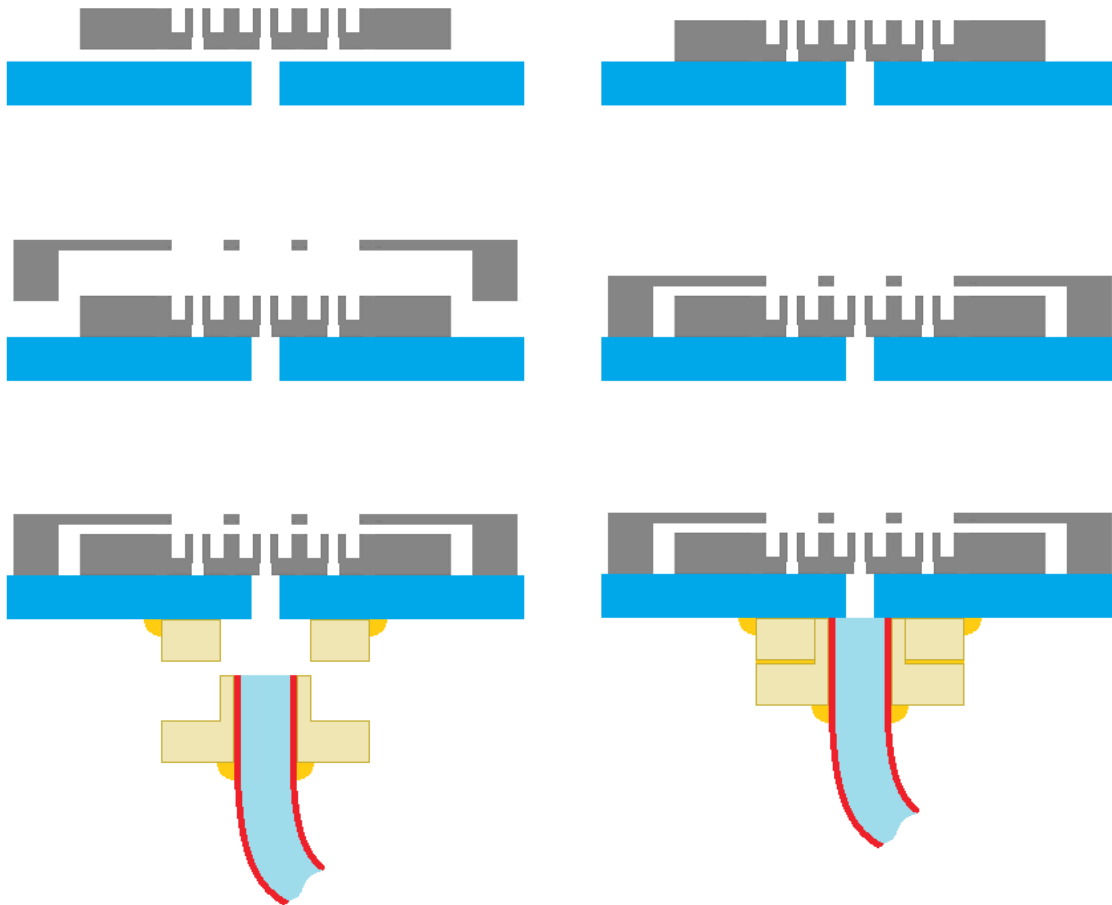
Figure 15. Assembly of the fully integrated electrospray head. First the emitter die is aligned and bonded to the Borofloat slice, then the extractor is also aligned and anodically bonded. Finally the microfluidic port is glued to the glass and the capillary to it.

with the extractor dice and bonded to the borofloat substrate (4). The microfluidic channels are connected with the reservoir by gluing the first part of the microfluidic interface into the borofloat with epoxy (5) and finally fixing the head of the port to the glued portion (6)

The actual integrated propulsive head is shown in figure 16, the capillary and microfluidic port are not yet attached to the glass slice, it can be seen that in some regions the anodic bond is not perfect by the presence of Newton rings, these minor gaps however does not affect the electrospray operation, the diameter of the glass slide is 2 inches.
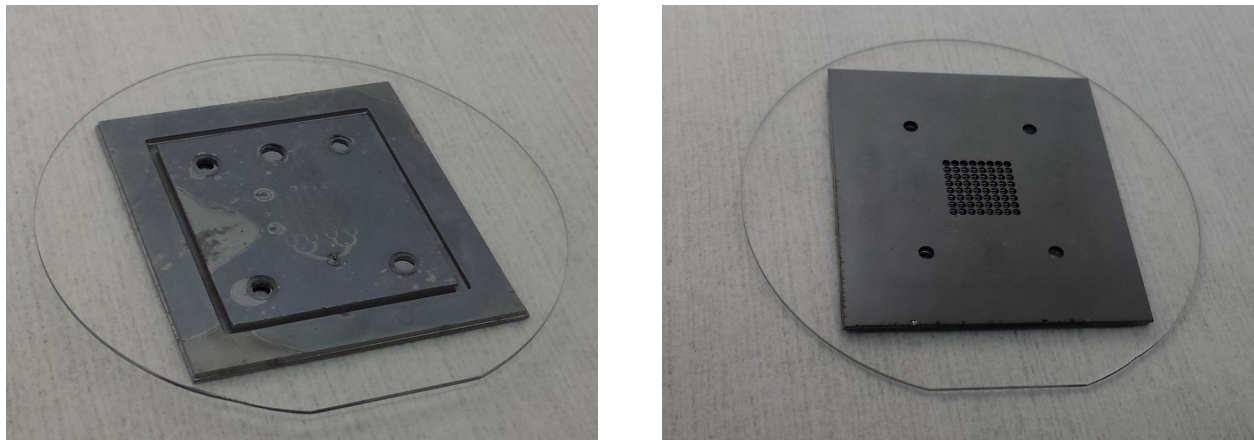
Figure 16. Fully integrated electrospray head. Left the back side with the sealed microfluidic channels and the extractors bonded. Right top view of the head.

II.9 Conclusions

The main results of the design discussion, microfabrication and assembly of the device are:

- The maximum aspect-ratio of the emitters is bounded to the DRIE system capabilities. The minimum feasible external diameter for a depth of 300 μm and an internal diameter of 40 μm is 100 μm.

- The solid angle determined by the tip of the emitter and the extractor aperture needs to be large enough to avoid trapping large fractions of the electrospray beam. Our target value is 45°

- A system of high flow resistance is required. The impedance for each emitter needs to be much higher than the variation due to microfabrication defects.

- The assembly of all the components must guarantee that misalignment between electrodes is avoided.

- Fully functional electrospray sources head are assembled.

Analysis of electrospray source head performance

A fter the assembly of the electrospray sources they are tested. In this chapter the reader will find the experimental results for four prototypes (Proof of Concept, HC-1, HC-2 and HC-3). The model microfabrication peculiarities and design are described; for example the extractor has been gradually thinned and the aspect-ratio of the emitters increases.

The experimental apparatus and methods used change gradually, as the refinement of the prototypes increases also do the number of detectors used. The standard tests performed include the dependence of the emitter and extractor current to the liquid flux and emitting voltage and endurance test.

For HC-3 an emphasis in the tests is made to analyze the prototype for electric propulsion. Using time-of-flight spectrometry the total thrust, mass flux, specific impulse and specific charge of the array are calculated. The maximum values are 34.19 μN, 2.81·10^{-8} kg/s, 245s and 3142 C/kg for thrust, mass flux, I$_{sp}$ and specific charge.

III.1 Single emitter proof of concept

After the challenges found during the microfabrication of the original geometry emitters the aspect ratio were reduced and a set of experiments were performed to determine if electrospraying in the cone-jet mode could be obtained by low aspect ratio emitters. The

emitter dimensions are 200 μm in height, an outer diameter of 120 μm and an inner diameter of 40 μm. This proof of concept does not present microfluidic channels carved on the back side.

The extractor is a 2 inch wafer, 350 μm thick; with a 0.9 mm hole through the center. Instead of the microfluidic channels the package presents an internal reservoir; an additional 2 inch wafer with a 360 μm hole through it has a silica capillary of 360 μm external diameter and 40 μm internal diameter inserted at the center of the hole and kept in place with epoxy. Between this surface and the emitter die there is a 0.005" thick polycarbonate spacer to create the actual reservoir for the ionic liquid. The emitter and extractor are separated by a Teflon spacer measuring 0.01 inch thick.
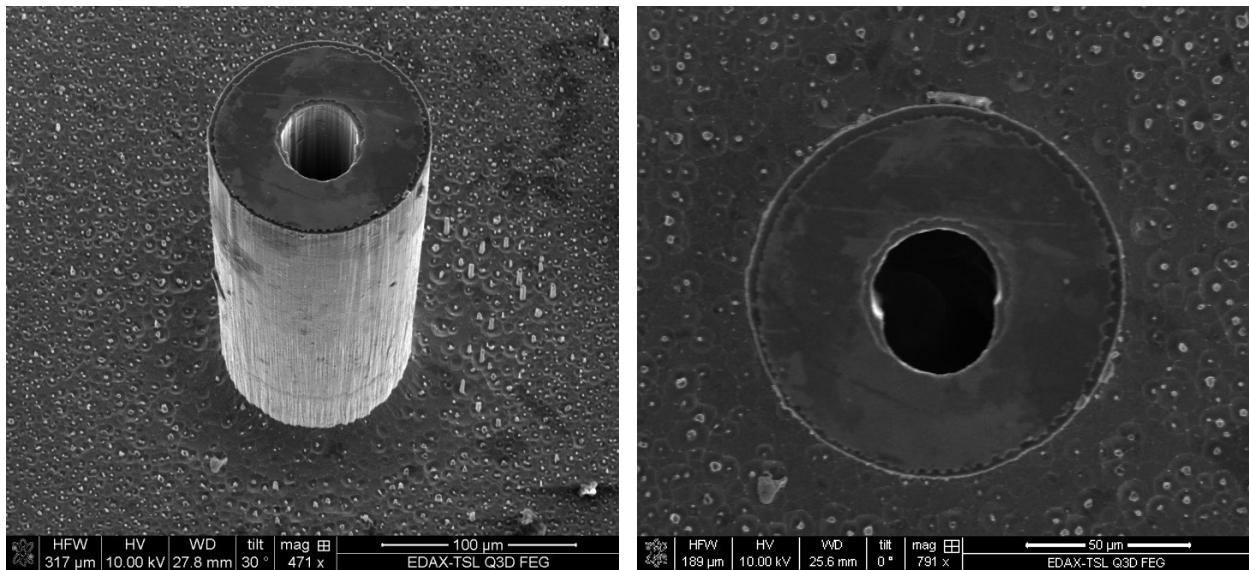
Figure 17. Detail of the single emitter; the external diameter of 120 μm and height of 200 μm.

Experimental setup
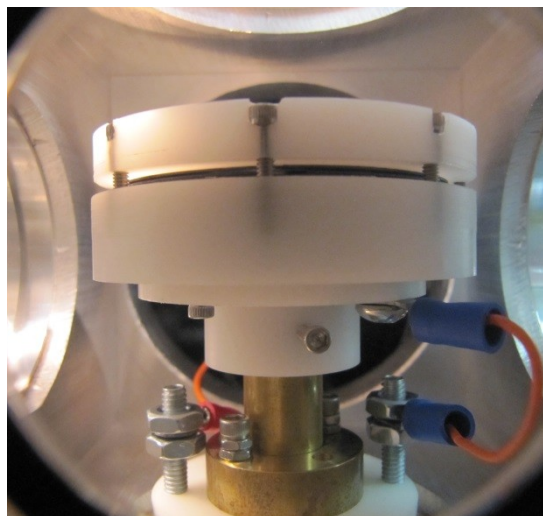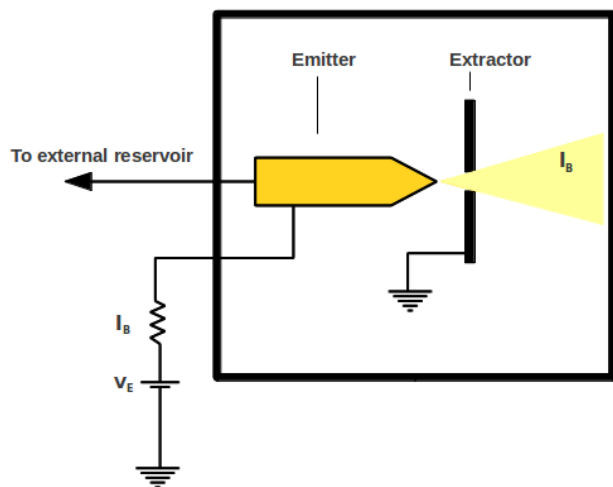
Figure 18. Schematics of the experimental set-up and the assembled head inside the vacuum chamber.

Figure 18(right) shows the PEEK structure inside the vacuum chamber where the atomization will take place; the image on the left there are the schematics of the experimental set-up; the vacuum inside the chamber is maintained below10-5 Torr. The capillary feeding the emitter is connected to the liquid reservoir outside the vacuum chamber. The pressure on the external reservoir can be controlled to sustain different flow rates. Once the voltage between extractor and emitter electrodes sets the cone-jet the current of the electrospray beam is measured with an electrometer.

We used the ionic liquid 1-ethyl-3-methylimidazolium bis(trifluoromethylsulfonyl) imide, Emi-Im [74], [75]. EMI-Im provides high electrical conductivity and low vapor pressure to generate a stable and reliable electrospray in vacuum. Another advantage using Emi-Im as a source is that its electrospraying characteristics are very well documented [75]. However, Emi-Im is not the only ionic liquid suitable for electrospray atomization, a wide range of ionic liquids with different physical properties are available

Experimental Results

In figure 19 we present the current going through the emitter as the pressure in the external reservoir and in consequence the mass flow changes. The currents through the emitter do not increase as the square root of the pressure as a cone-jet electrospray should, this discrepancy might be due to small pockets of air trapped inside the reservoir disturbing the stability of the cone-jet but from the experience gathered on later stages we suspect that considering the high currents emitted by the source the operating mode is not a stable cone-jet.

However we proved that emitters with low aspect ratio are still able to sustain an electrospray.
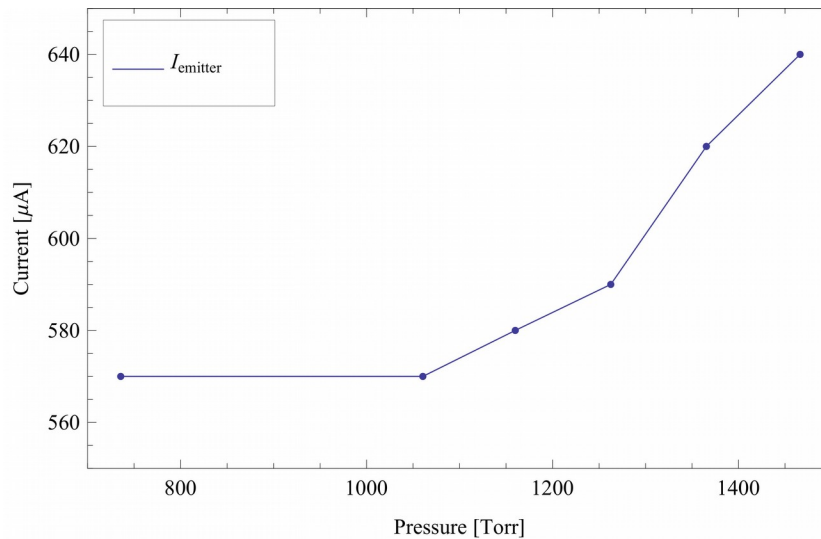
Figure 19. Results for a single emitter without micro-channels

III.2 Single emitter analysis (HC-1)

After the previous tests were finished with the stocky emitter, the DRIE system underwent an upgrade that increased the switching velocity of the gases improving the wall profile. Using the upgraded system and with the experience gathered in chapter 2 we microfabricated thinner emitters, where the external diameter is 100 μm, the internal 40 μm and the height 300 μm.

In this section, we characterize these new slender emitters, we include the microfluidic channels carved onto the back side to facilitate the analysis of the multiemitter head, we will be able to estimate the current that 64 emitters should emit for a given pressure drop. To achieve the device design a full array with its microfluidic channels is microfabricated, later all the emitters except one are plugged with epoxy, afterward, the electrospray head is assembled on the PEEK plastic structure. The extractor thickness is 450 μm and a Teflon separator of 250 μm maintains the distance between electrodes.

Experimental apparatus

The experimental set-up (figure 20) does not differ considerably from the previous one; the pressure difference between the external reservoir and chamber is still responsible for setting the Emi-Im flow feeding the emitter. The capillary connecting the reservoir and the propulsive head is 33 cm long with an internal diameter of 40 μm.

While the operational set-up remains the same, two new detectors are added:not only the current through the emitter is recorded but also the extractor is connected to an electrometer to measure the flow of the particles impacting its surface.
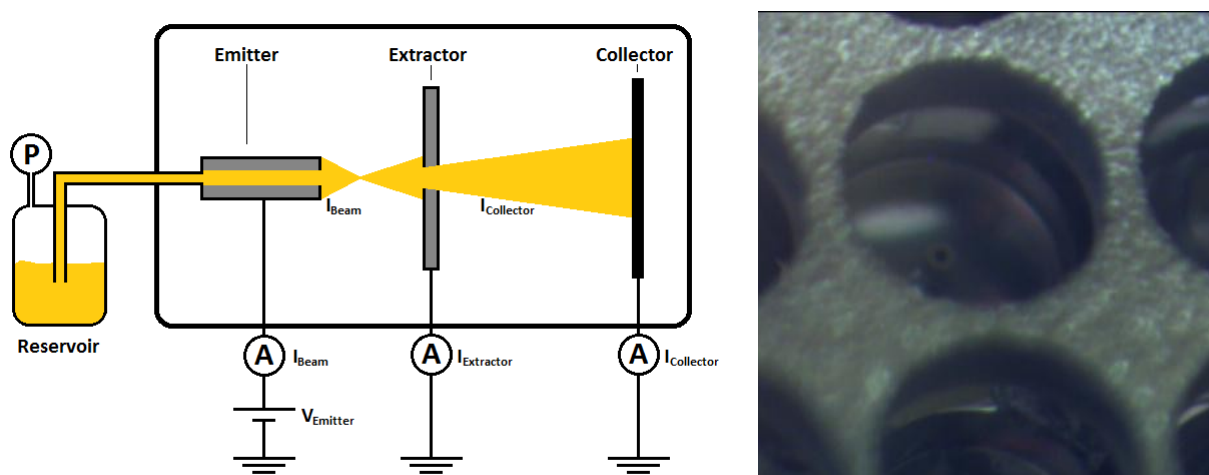
Figure 20. Schematics of the experimental set-up and detail of the emitter and extractor.

To ensure that the current measured in the extractor truly portrays the impact of charged droplets and is not caused by secondary ionization, a collector or Faraday cup is introduced inside the vacuum chamber to detect the current of the particles emitted by the electrospray source. Obviously if secondary ionization is negligible the currents should read: $I_{Emitter} = I_{Extractor} + I_{Collector}$

Results

In figure 21 the evolution over time of the emitter current and reservoir pressure is presented for three emitter voltages ($V_{emitter}$), -1650 V, -1750 V and -1850 V, the pressure is manually changed from 160 to 440 Torr. For each pressure jump the current through the emitter increases accordingly for all the voltages.

After 18 minutes spraying at -1850 V several bursts of current in the emitter appear. Although the collector and extractor were in place the signal noise was too high to offer any
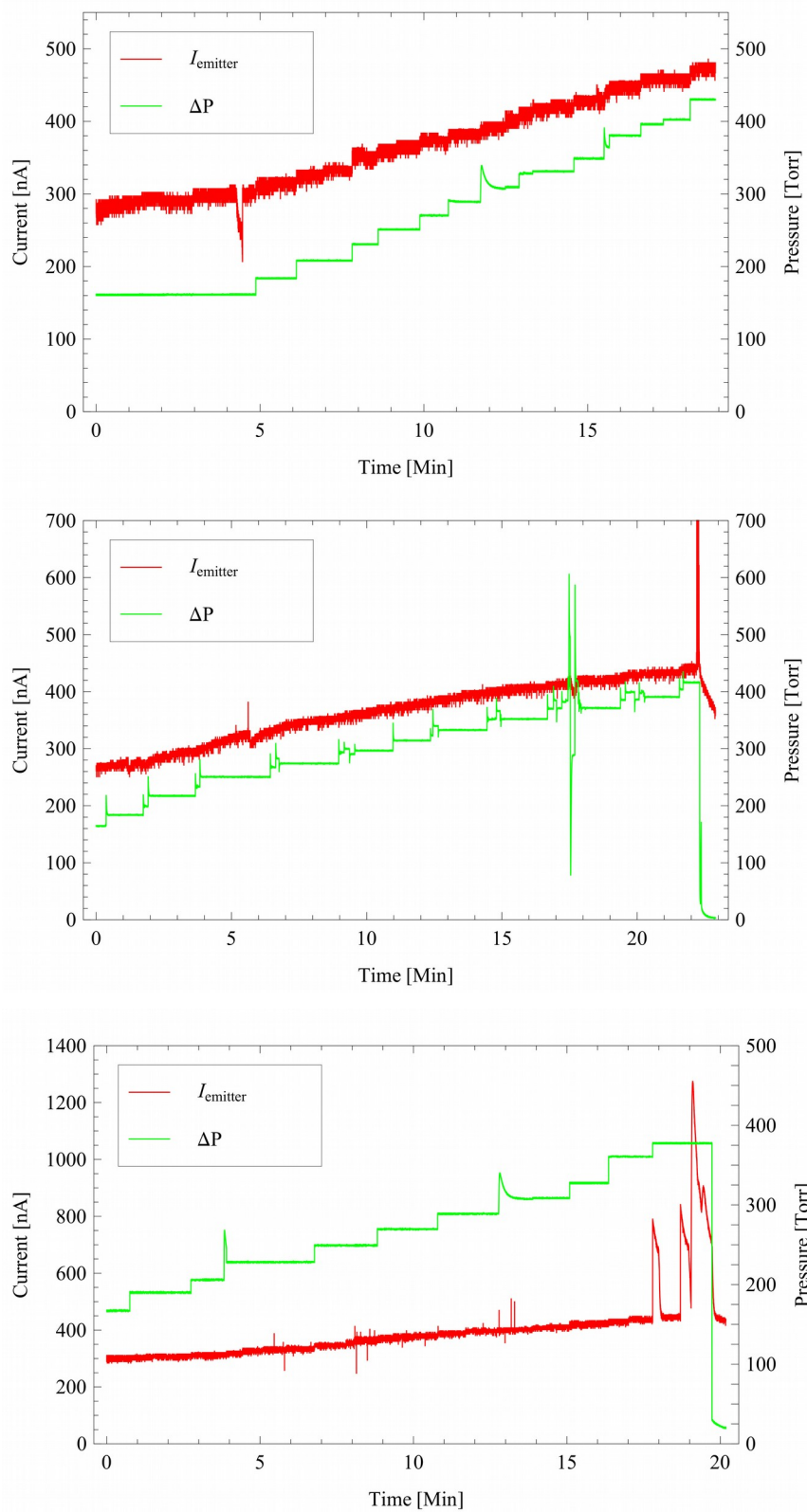
Figure 21. Results for a single emitter at -1650 V -1750V and -1850V for increasing pressure

relevant data, however the most plausible explanation for the sudden increase of current in the emitter is that the fraction of the jet impacting the extractor is high enough to accumulate enough liquid to short circuit the electrodes.

Figure 22 plots the beam current against the pressure, the points recorded during pressure transition and current bursts have been eliminated to have a clearer image of the electrospray behavior. Some conclusions can be drawn from this graph; the current grows with pressure as well as the consequent increase of flux but the pressure range is too narrow to determine if it grows as a function of the pressure square root[60]. Although one would expect that the current would be higher at larger voltage differences its effect during the cone-jet mode is small, while the temperature between runs have an effect on the liquid permittivity and the current emitted [60], at -1650V and -1850V the temperature was 20 °C the run performed at -1750 V had a temperature of 23 °C.
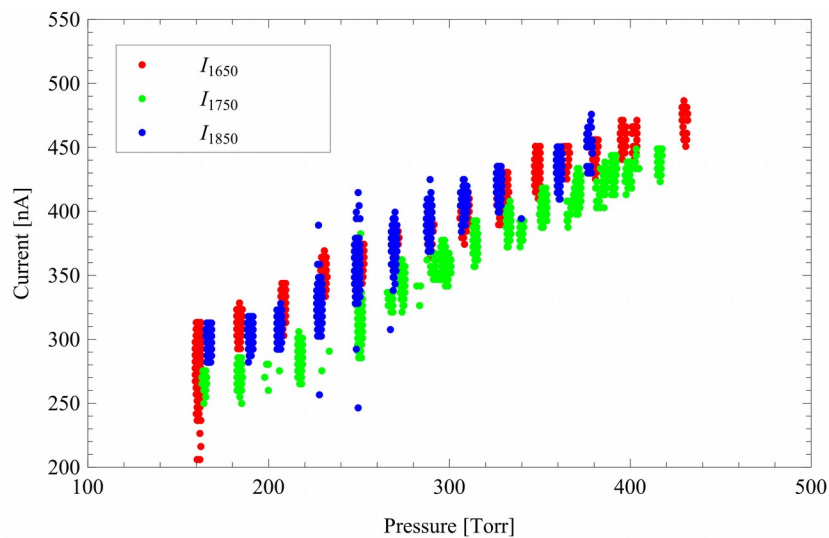
Figure 22. Current as function of the pressure for three different voltages

These results prove that the microfabricated emitter can electrospray in the negative mode, important for sputtering applications where the flux of electrons departing from the sputtering target needs to be minimized, if the flux of electrons creeping towards the emitters is high the Taylor cone becomes unstable. However satellite electric propulsion systems tend to work in positive mode. Producing electrons to neutralize the spacecraft is much easier than produce positive charges and can be done easily with a thermionic emitter.
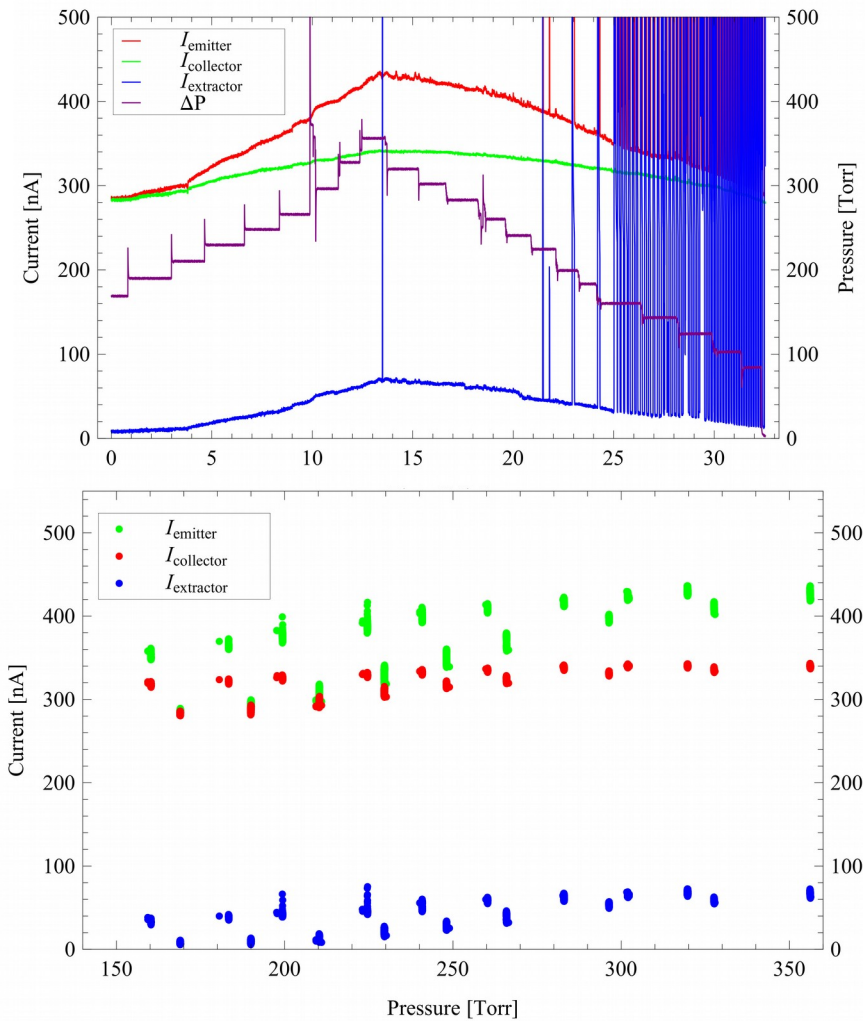
Figure 23. Evolution of the current at the emitter, extractor and collector over time and currents as a function of the pressure at a fix $V_{emitter}$ of 1650V

After putting in place RC circuits to filter the electrometers signal the emitter source was used in positive mode. Two sets of experiments are performed, first $V_{Emitter}$ is maintained at 1650 V and the pressure varies between 350 and 90 Torr, then with a fixed pressure of 100 Torr the voltage at the emitter is changed between 1220 and 2120 V.
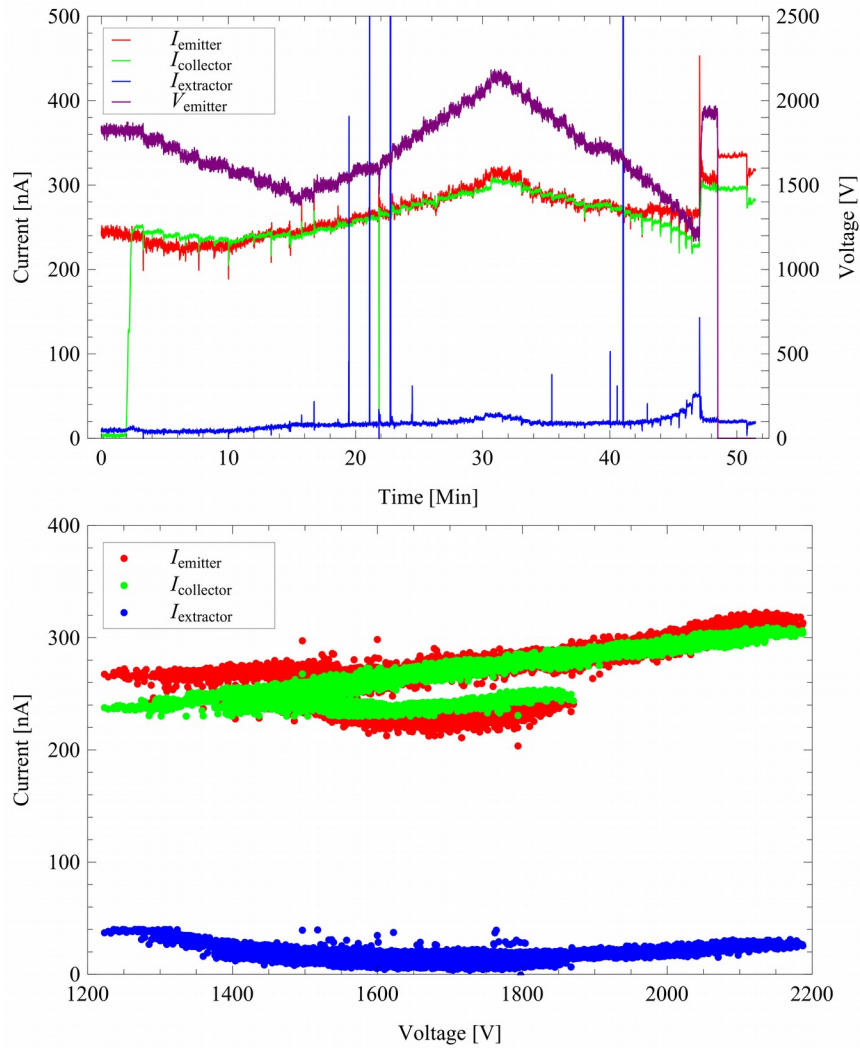
Figure 24. Evolution of the current at the emitter, extractor and collector over time and currents as a function of the voltage at a fix pressure difference of 100 Torr

The results are summarized by figure 23. The first image presents the time variation of all the parameters and in the second the emitter, extractor and collector currents are plot against pressure. The thickness of the extractor is large enough to trap a noticeable fraction of the beam specially at higher flows. After 25 min the electrodes are short-cut regularly, the use of three electrometers confirms that, the current at the extractor and emitter have considerable spikes but not the collector current.

The current is plotted as a function of the pressure after filtering the pressure transients and the regions with short-cuts in the image below. All three currents display some degree of hysteresis, looking at both plots we realize that the current has some hysteresis; in the pressure interval 150-275 Torr the current branches in two, we hypothesize that some air might have been trapped in the microfluidic channels restraining the flux, some time was required to arrive to steady-state operation.

The time evolution of the experiment for variable voltage is presented in the first plot of figure 24; after the cone-jet has been stabilized at 1850V the Faraday's cup is inserted in front of the source to collect the charged particles (after 2 minutes); after 43 minutes the extractor current starts to increase significantly, this ramp matches almost perfectly with the current difference between emitter and collector. This fact combined with the plateau that the emitter current presents leads us to conclude that a liquid bridge was formed in the separator, even in these circumstances the power supply could provide enough power to sustain the electrospray. After 48 minutes the experiment was stopped. On the current versus voltage plot there is a clear monotonic relation between them, however these runs also have hysteresis for currents at the emitter and collector, but in this case not for the

extractor. From the first figure seems that for some extent the current at the extractor is a function of the time but also voltage.

III.3 First multi-emitter analysis (HC-2)

After all the gathered experience characterizing the single emitter we proceed to the full array of 64 sources, the emitters are 100 μm in external diameter, 40 μm internal and their height is 300 μm. Like the previous single emitter device the array die is bonded to a boroflat substrate. Emitter and extractor components are sandwiched together using a PEEK structure, a 250 μm Teflon separator keeps the distance between them. Figure 25 are SEM pictures of part of the array and the detail of an emitter.
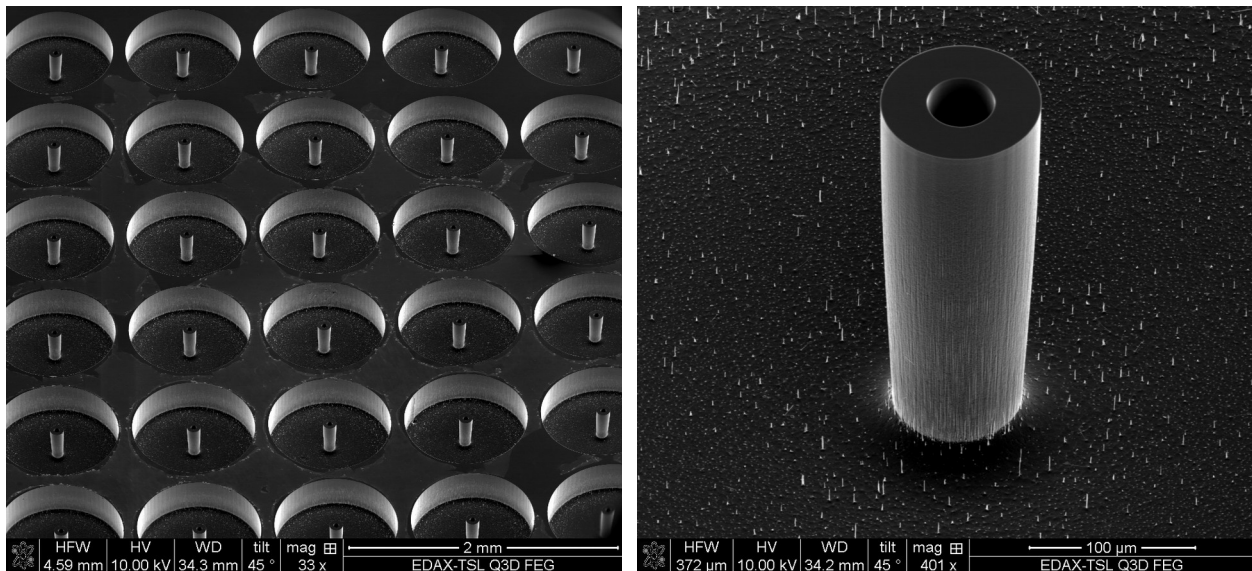
Figure 25 SEM image of the array of micro-emitters, 300 μm tall and 100 μm in diameter. Detail of a single emitter

Experimental set-up

The details on the experimental apparatus can be reviewed in the previous sections; the multiplexed electrospray source is placed inside a vacuum chamber maintained at a pressure lower than 10^{-5} Torr, the reservoir containing the ionic liquid is kept at a higher pressure to draw Emi-Im towards the tips of the silicon needles where the ionic liquid is atomized; three electrometers record the emitter, extractor and collector currents carried by the charged nanodroplets. The tests for the HC-1 single emitter device revealed that a significant part of the beam impacted the extractor, this limits the maximum running time, so to facilitate the flow of the beam exiting the extractor its thickness has been reduced to 350 μm. The silica thread has also been changed, now that the thruster head has 64 fully functional emitting sources the flux is expected to be 64 times larger, to avoid an extreme pressure drop in the capillary their inner diameter needs to be larger, knowing that the hydraulic resistance is a function of the inverse of D^4 the internal diameter that will provide
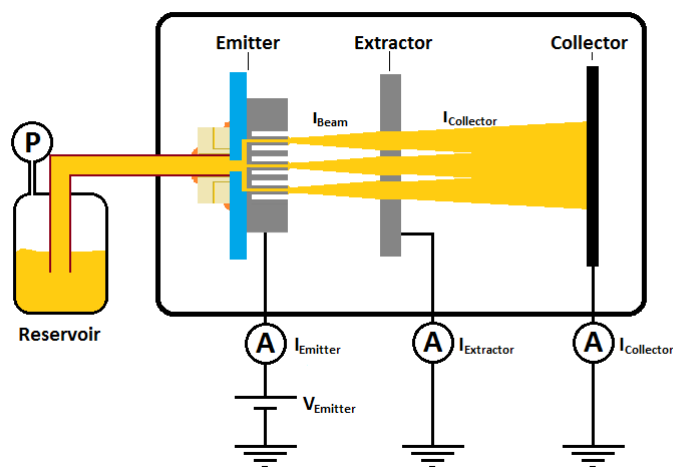
Figure 26. Experimental set-up, three electrometers measure the current emitted, current impacting the extractor and current at the collector.

the same pressure drop in the thread would be 100 μm. This does not take into account the pressure drop increase at the branching. To allocate for this extra pressure we use the next diameter readily available in our lab that is 200 μm. This diameter might seem excessive and possibly reduce the pressure resolution, however the maximum flow resistance is created by the microfluidic channels.
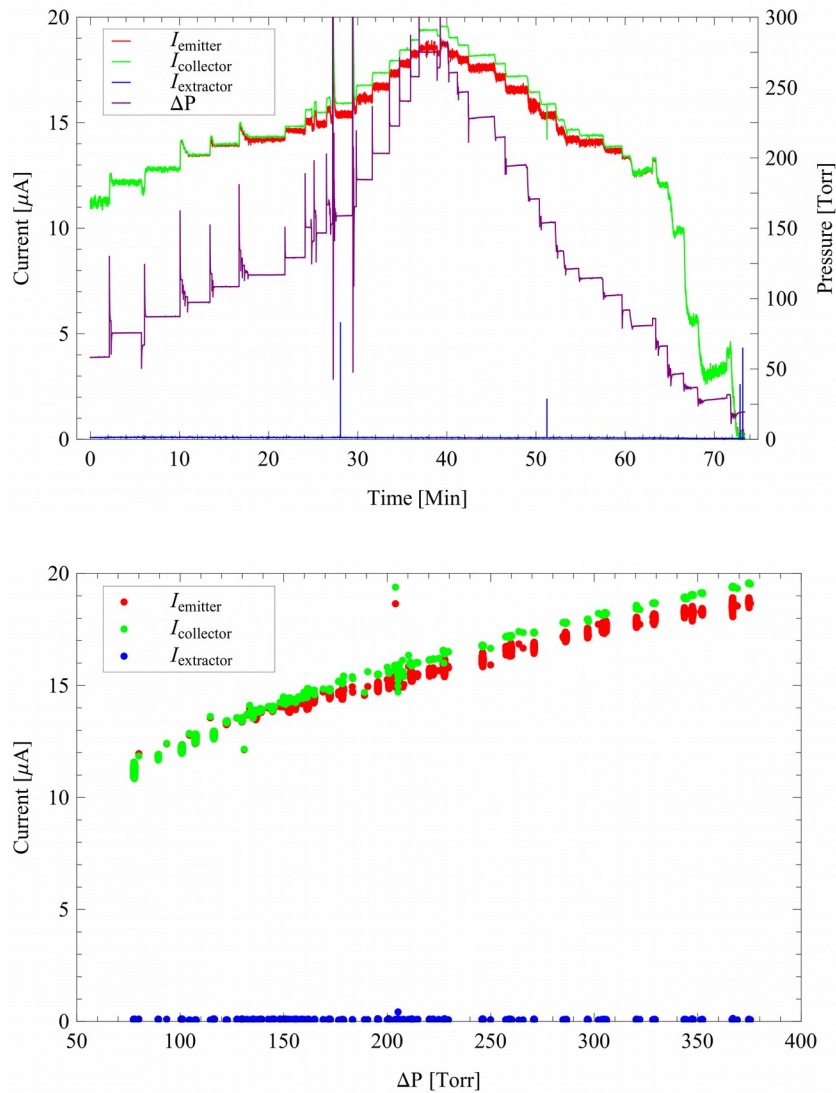
Figure 27. Evolution of the current at the emitter die, extractor and collector over time and currents as a function of the pressure at a fix $V_{emitter}$ of 1650V, for an array of 64 emitters.

Results

Again the currents in the emitters, extractor and collector and the pressure difference in the reservoir are plotted against the time in figure 27. The multisource emitted for more than 70 minutes; during this time, it is readily observed that there are not consistent short circuits and the current through the extractor is almost insignificant, this can be attributed to the 100 μm extractor thickness reduction.

At the same time the evolution for the currents are a slightly incongruous, for the middle section of the experiment the current at the emitter is considerably smaller than the one in the collector, we suspect that this discrepancy is caused by a faulty op-am in the electrometer (later it was observed how its offset jumped between values). Finally there is a dramatic drop on the current once the pressure goes below 50 Torr; even if some emitters are still operating on the cone-jet mode some are intermittent and others stop completely.

The filtered signal is plot against pressure, while extractor current remains floored for the whole pressure interval both collector and extractor currents grow as the factor of the square root of the pressure, strictly only the emitter current should follow this scaling law but because the current loss at the extractor is irrelevant the collector can be used to depict the multiplexer characteristics. If we do regress the current (in μA) for the pressure (in Torr) we obtain that $I_{EmitterT} = 4.52 + 0.78\sqrt{\Delta P}$ and $I_{CollectorT} = 5.44 + 0.69\sqrt{\Delta P}$ if we use the flow impedance to transform the regressions to have the value of the current emitted by each emitter as the volumetric flux of each emitter in [A] the result is $I_{Emitter} = 7.03 \cdot 10^{-8} + 0.32\sqrt{Q}$ and $I_{Collector} = 8.50 \cdot 10^{-8} + 0.28\sqrt{Q}$ which is close to the value that the scaling law of Fernando de la Mora and Loceratels [60] gives for Emi-Im

$I = 0.25\sqrt{Q}$ (there is no known value of the permittivity of Emi-Im so we used a value of 10[75].

The time response to start the electrospray once the liquid has filled all the channels is fast, it takes only 12 seconds to have all 64 emitters electrospraying in synchrony for a pressure step of 70 Torr (figure 28); on the other hand it takes almost four times to completely interrupt the nanodroplet emission. This is due, not only to a transitory on the pressure but also to the electric field, once the Taylor cone is established it keeps drawing some liquid towards the emitting apex.
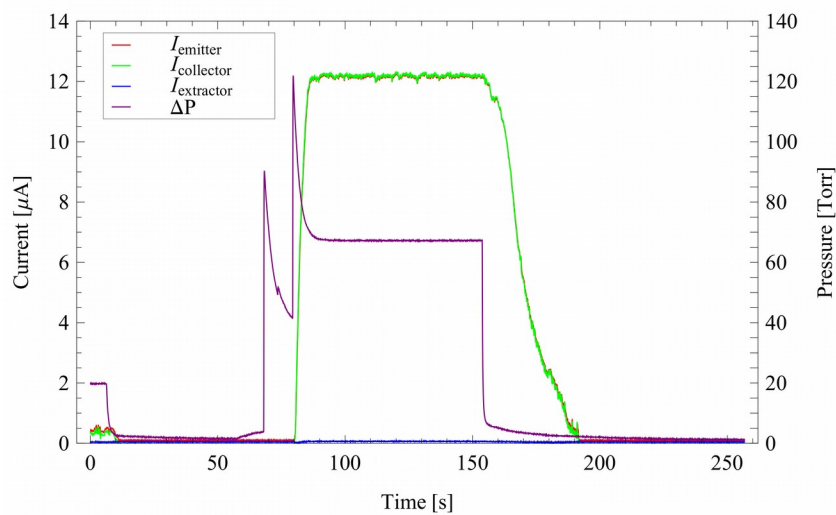
Figure 28. Time response of HC-2 to a pressure step. The emission interruption response is four times slower than the starting response.

The results of keeping the pressure at 60Torr while sweeping the emitting voltage between 1.4 and 2.35 kV are shown in figure 29. At this pressure and below 1.55 kV the current emitted starts to decrease signaling that at those conditions the cone-jet mode is

not stable for most of the emitters, also further decreases in tension result in great current drops, reinforcing the hypothesis that the vast majority of the array is on pulsing mode or not emitting. In the current versus voltage there is some hysteresis for a range of voltage two solutions are possible; the meniscus forms a Taylor cone or emits in a pulsating mode
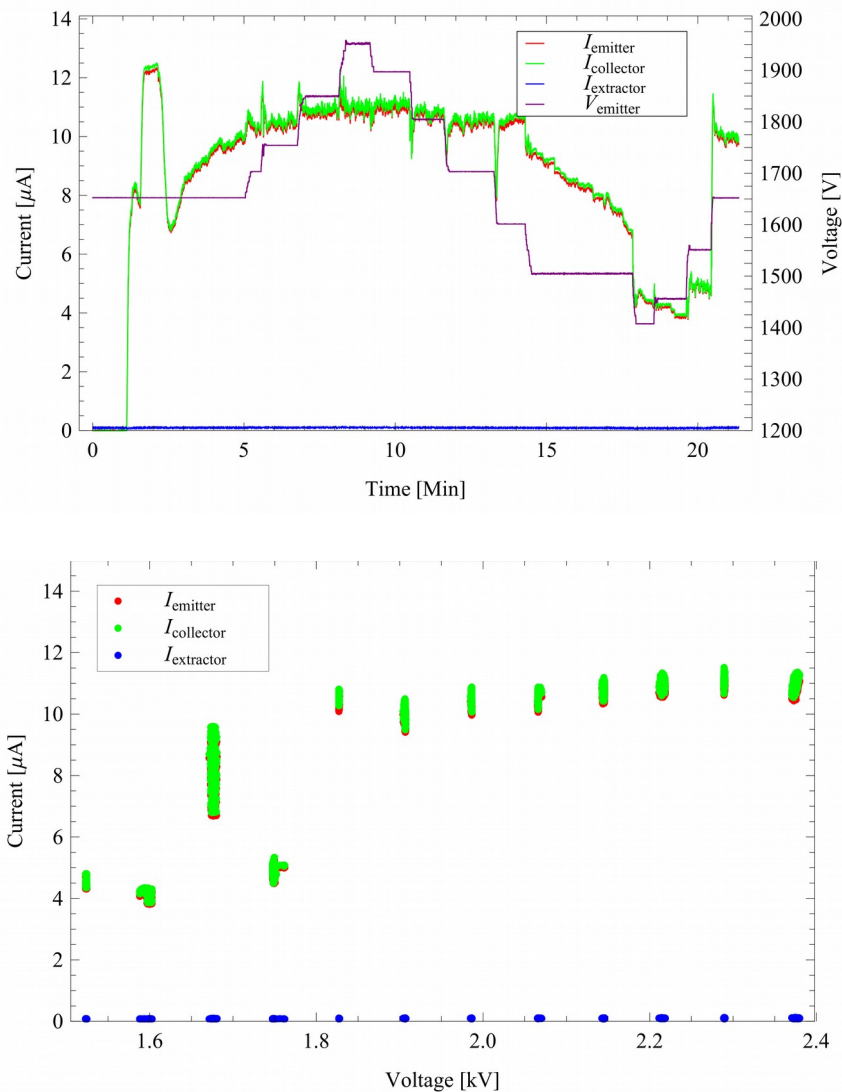
Figure 29. Evolution of the current at the emitter die, extractor and collector over time and currents as a function of the voltage at a fix ΔP of 60 Torr, for HC-2

[45] for higher voltages the influence of the voltage increase is of little significance for the current emitted.

Finally the electrospray head undergoes an endurance test (figure 30), the voltage is set at 1.65 kV and the pressure is maintained between 50 and 65 Torr the thruster head is left running without any interruption for almost 12 hours. During this time there are no significant currents leaking through the extractor. The emitted current stabilizes around 12 μA after 2h, from that point it fluctuates with the pressure adjustments. The pressure is recorded from the 1.5 hour mark onwards.
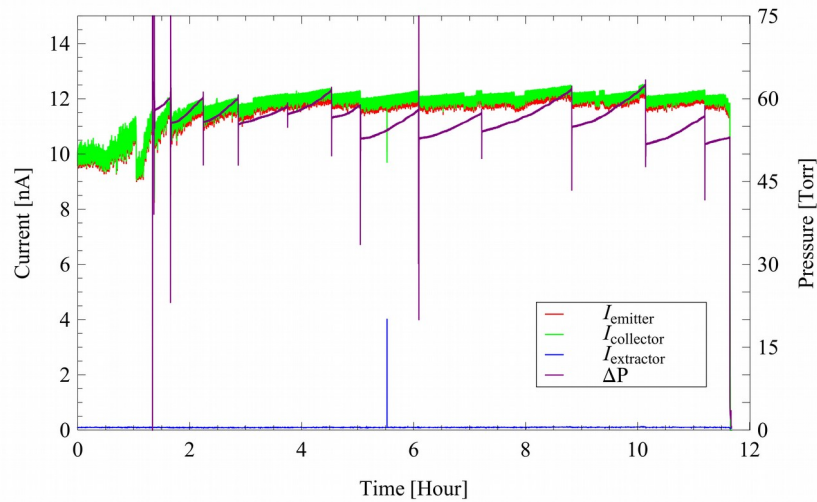
Figure 30. Endurance test: HC-2 runs continuously for 12h at a voltage of 1650 V and a pressure between 50 and 65 Torr.

III.4 HC-3 characterization

The last device that has been fully tested is a slight modification of HC-2. While the geometry of the emitter has not changed the dice size is reduced allowing for batch fabrication. One of the limitations of the original DRIE system was the non-uniformity of the etch ratio for the emitters along the wafer. With the upgraded system we can process 7 dice with a success yield close to 70%.

At the same time the thickness of the extractor is reduced another 100 μm to a final value of 250 μm that combined with the 250 μm Teflon separator results in the desired 45° solid angle between emitter tip and extractor aperture disk.

The final dimension of the assembled propulsive head (Fig. HC-3) are also smaller than the previous prototypes, the external diameter is now 1.6 inches.

Experimental set-up

While the general structure of the experimental set-up remains the same, the collector is substituted by a time-of-flight (TOF) detector consisting of a collector and a grid suppressor. The distance between the TOF collector and the extractor L_{TOF} is 129 cm and during TOF analysis the grid voltage is kept at -10 V to repel the electrons. When TOF analysis is not necessary, grid and collector are connected, the voltage is 0 V, and one electrometer is used to measure the combined currents, in essence we have the exact same apparatus used for HC-2.
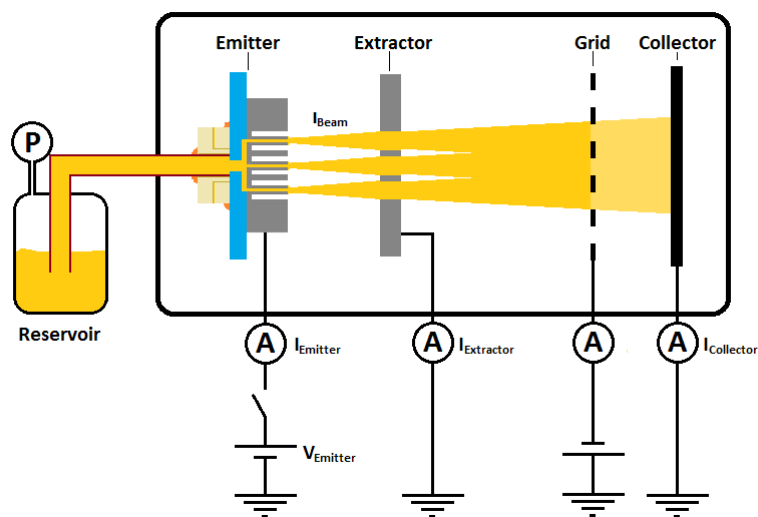
Figure 31. Experimental set-up, the collector has been replaced by a time-of-flight sensor

The silica capillary bringing the liquid to the multiplexed source has an inner diameter of 200 µm and a length of 45 cm.

Results

The first part of the HC-3 analysis replicates the experiments performed also on HC-2; figure 32 presents the current and pressure relation. While the voltage at the emitter is fixed at 1.8 kV the pressure range from 50 to 750 Torr; at the lowest pressures of 50 and 100 Torr the variance is considerable, the sources are not spraying in the cone-jet mode. After 2.5 hours of tests the extractor and emitter electrometers start to record current outbursts due to liquid a between them; however the voltage supply has enough power to maintain operation. If we filter the current signal removing the shortcuts and pressure transients and we plot it against the pressure it is clear that the emitted current grows with the square root of the pressure difference. For the fitting of the emitter current the
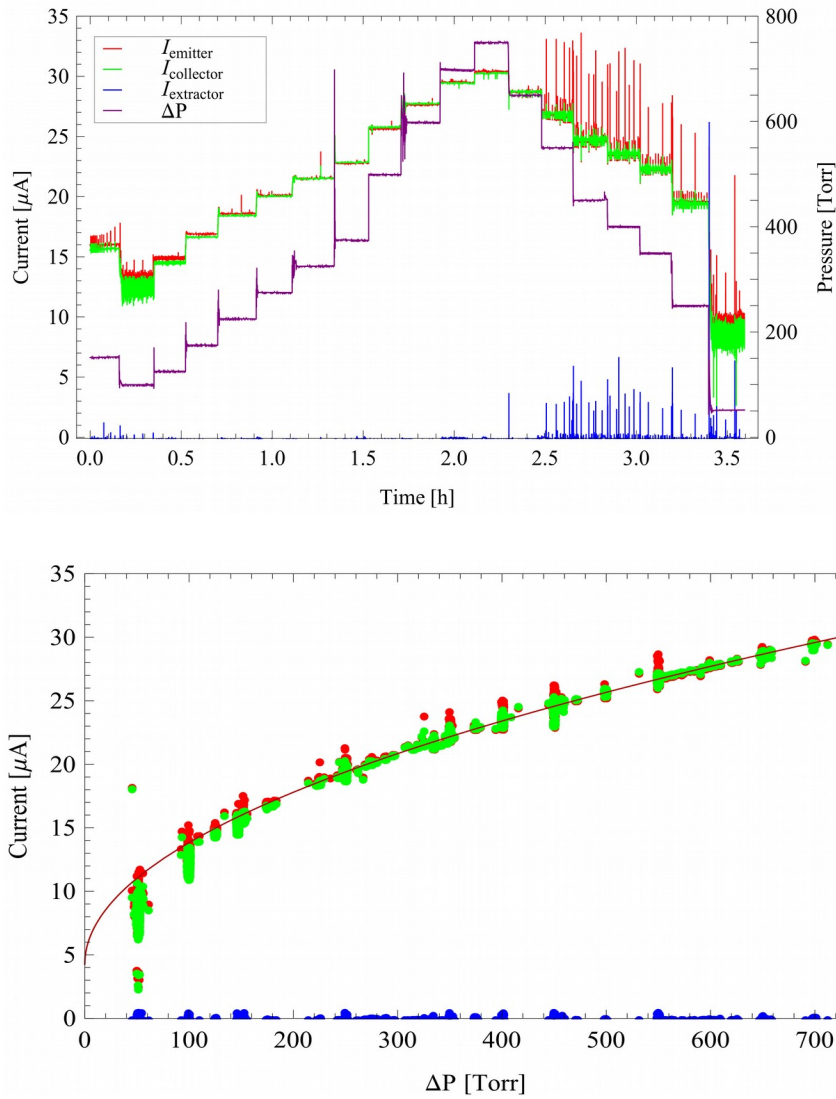
Figure 32. Evolution of the current at the emitter die, extractor and collector over time and currents as a function of the pressure at a fix $V_{emitter}$ of 1800V, for the thruster head HC-3.

pressures below 125 Torr have been ignored. The regression for the total current (in μA) as a function of the pressure difference (in Torr) is $I_{Total} = 4.27 + 0.96\sqrt{\Delta P}$ and the resulting current for a single emitter (A) as a function of the volumetric flux (in m³/s) is $I_{Emitter} = 6.67 \cdot 10^{-6} + .47\sqrt{Q}$ a result of the same order as $I = 0.25\sqrt{Q}$ (we must remember
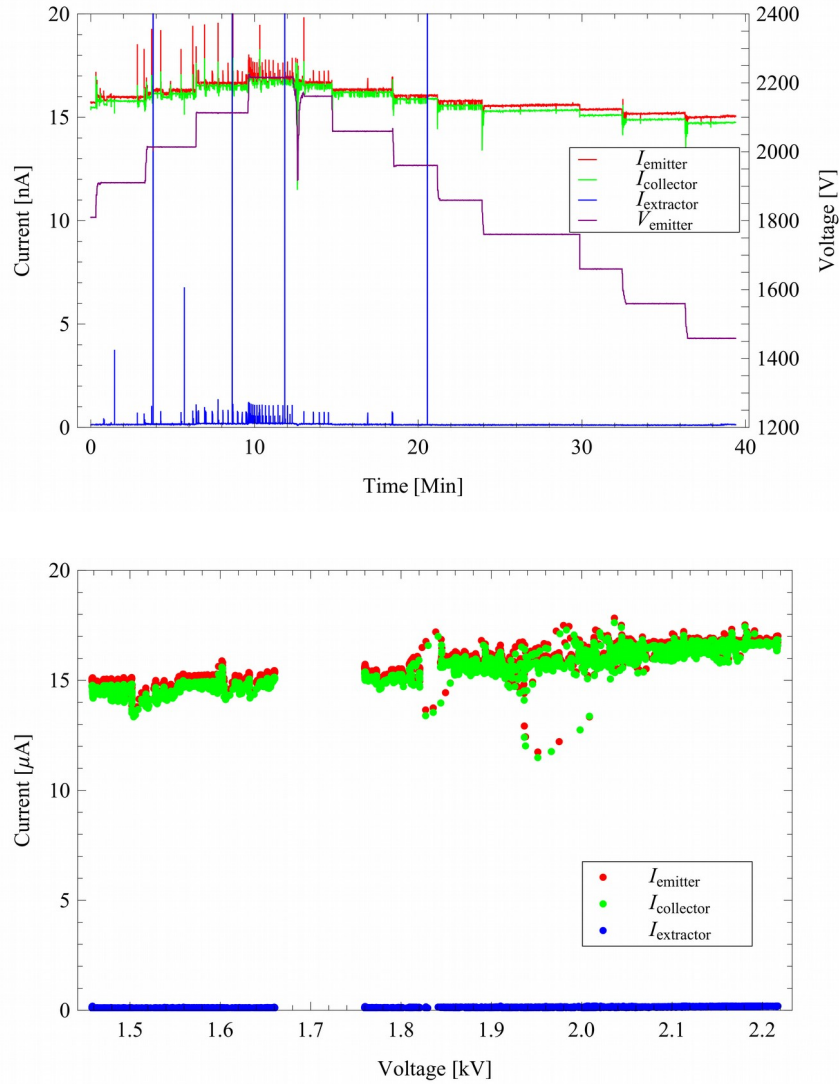
Figure 33. Evolution of the current at the emitter die, extractor and collector over time and currents as a function of the voltage at a fix ΔP of 150Torr, for the thruster head HC-3.

that we are using an estimate for ε of the Emi-Im and an approximation for the function g(ε) defined by [60].

The next experiment sets the pressure at 150 Torr, the voltage varies between 1.45 and 2.2 kV. For the first 15 minutes of the experiment the power supply is shorted regularly, later the liquid bridging the extractor and emitter probably evaporates and with it the

current bursts (figure 33). The filtered signal of current as a function of the voltage is shown after the time evolution, for the range used the emitter current seems to grow linearly. The extractor one also increases with voltage but it accounts for less than 2% of the total current emitted.

The following four diagrams (figures 34, 35, 36 and 37) are the result of the time of flight analysis. The time-of-flight detector on figure 31 measure the waves generated by periodically shorting the needle to ground with a high-speed, high-voltage switch. The spray is formed by a continuity of different species with different velocities. We can calculate the velocity (v) of the species arriving at the detector at certain time after the interruption of the spray, which is the time-of-flight (t_{TOF}) the value is:

$$v = \frac{L_{TOF}}{t_{TOF}} \tag{24}$$

The differential of mass flux (dṁ) at any given time can be written as

$$d\dot{m} = \frac{dI}{\xi} \tag{25}$$

where dI is the current differential. We know that there is no dissipation and the kinetic energy of a droplet it is equal to the electric potential energy when it is from at the end of the cone-jet

$$q V_A = \frac{1}{2} m v^2 \quad , \tag{26}$$

where V_A is the acceleration voltage, equal at the voltage difference between electrodes minus a loss associated with the cone jet separation, this loss has been found previously by retarding potential analysis. Then we can write the charge to mass ratio ξ as

$$\xi = \frac{L_{TOF}^2}{2 V_A t_{TOF}^2} \quad . \tag{27}$$

54

Then we integrate to obtain the mass flow

$$\dot{m}=\frac{2V_A}{L_{TOF}^{\,2}}\int t^2\,dI=\frac{2V_A}{L_{TOF}^{\,2}}\int t^2\,\dot{I}(t)\,dt \quad . \tag{28}$$

Using similar procedures the thrust is calculated with

$$T=\frac{2V_A}{L_{TOF}}\int t\,\dot{I}(t)\,dt \quad . \tag{29}$$

The specific impulse (I_{sp}), thrusting efficency (η) and average specific charge ($\langle\xi\rangle$) can be calculated as follows:

$$I_{sp}=\frac{T}{\dot{m}\,g}, \quad \eta=\frac{T^2}{2\,\dot{m}\,V_{Emitter}\,I}, \quad \langle\xi\rangle=\frac{I}{\dot{m}} \quad . \tag{30, 31, 32}$$

Figure 34 is the measurement of nine TOF waves for different fluxes emitting at a voltage of 1800 V. All waves have a sharp current decline once the electrospray has been interrupted. There is first a sharp decline on the current, ions are the species responsible for this narrow decline; as we have seen the velocity of the charged particles for an electrospray depends heavily on their charge to mass ratio, ions with their small mass are the particles with highest ξ of the spray and therefore the fastest particles in the mix, at the same time the variance of ξ for ions is very limited (the ions can carry only one unit charge and its mass is the one of Emi-Im cation, sometimes some solvated molecules can add to the mass) therefore the ion current decrease occurs first and along a very short period of time.

The charged droplets with smaller specific charge and a broader spectrum of charge to mass ratio result in slower current decay. The fraction of current carried by the droplets increases with the flux and also the specific charge variance.

The curves with higher flow present a distortion after the current has been interrupted, the cause could be used by capacitive coupling but then the distortion should
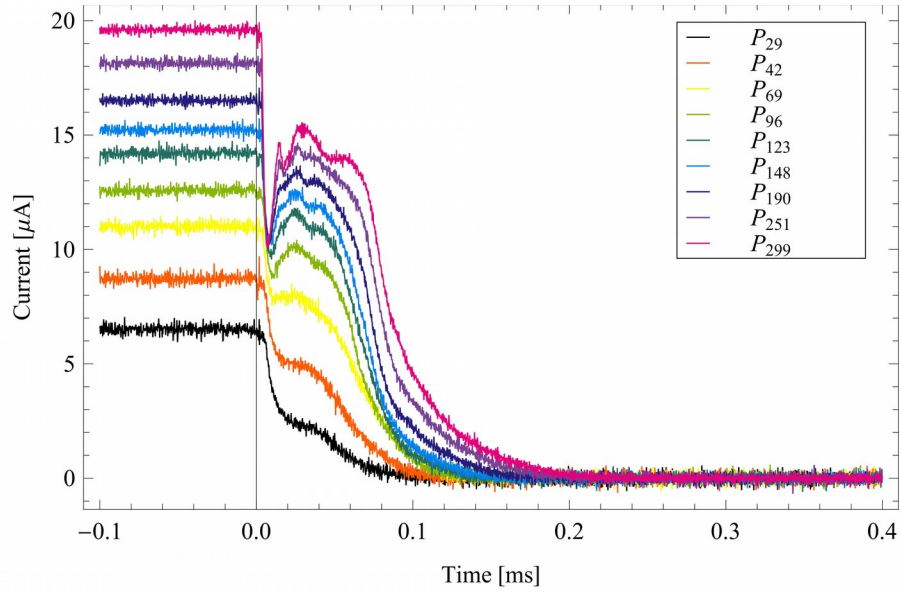
Figure 34. Time-of-flight analysis of HC-3 for 9 different pressures: 29,42 69, 96, 123, 148, 190, 251 and 299 Torr. The sharp decrease near the origin is caused by the ions, while the charged droplets produce the more gradual decrease. For the 6 higher pressures there is a perturbation after the spray is interrupted.
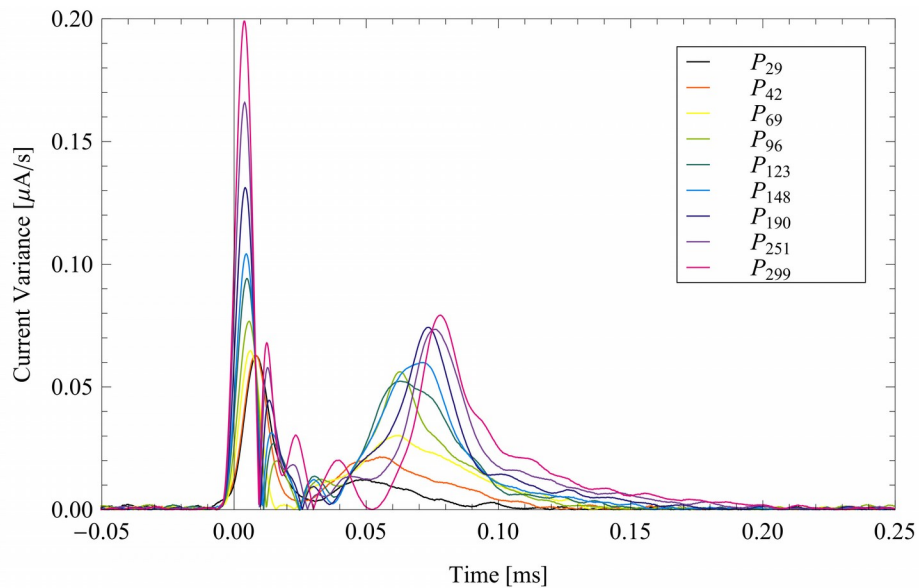
Figure 35. Density distribution of the species in the electrospray. The absolute of the total current derivative in figure 34. Note the narrow ion distribution compared to the scattered droplets distribution.

appear equally for all flows. We believe that the electrospray is not interrupted completely at time = 0, and for a short period of the droplets of the residual spray carry a higher current than the ones of the original electrospray creating the depression and later bump in the TOF curves. Despite this disturbance the effect while calculating the mass and thrust is negligible.

The presence of ions and droplets is more evident in the density distribution of figure 35, two peaks stand out for all curves, the first one, corresponds to the ions, with its narrow distribution and with the average TOF located at the same spot for all curves this is coherent with the previous argument that the charge of ions is fixed to one elemental charge and the variation in mass can only happen when there is solvation. The last peak with a larger variability is caused by the droplets, not only is the flux distribution is broadened but the average value is displaced. The other peaks appearing for certain fluxes have no significant physical meaning, they are a result of the disturbance at the interruption of the spray.

As expected the ions are responsible for a very small percentage of the mass of the electrospray figure 36 however as the mass flux is lowered the faster particles tend to represent more part of the electrospray mass.

While the ions are relatively insignificant in mass therms their contribution to the thrust is not, figure 37 shows how the thrust curve rises rapidly during the ion interval to increase more gradually afterward, until a plateau is reached; for the lowest pressure the thrust due to ions is almost 40% of the total.
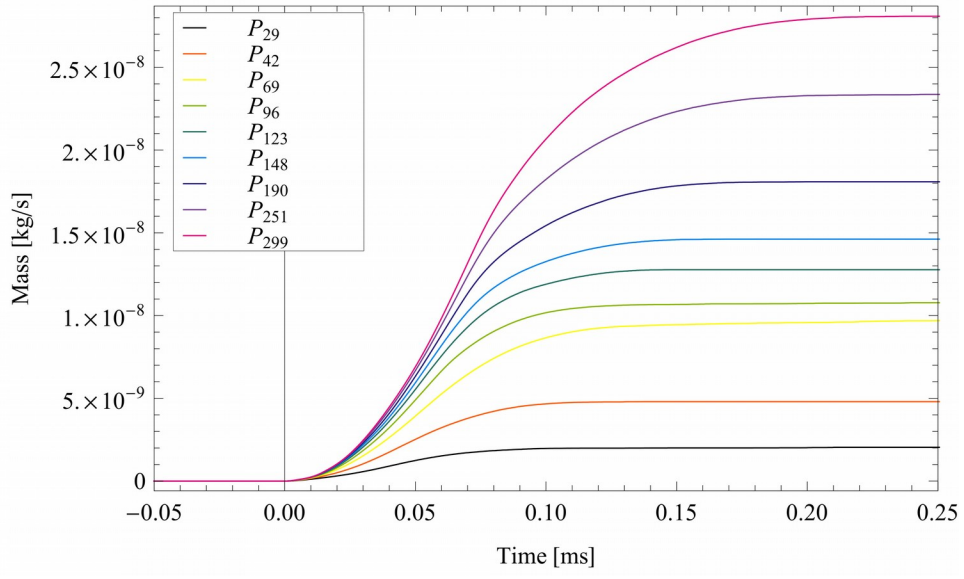
Figure 36. Cumulative mass flux
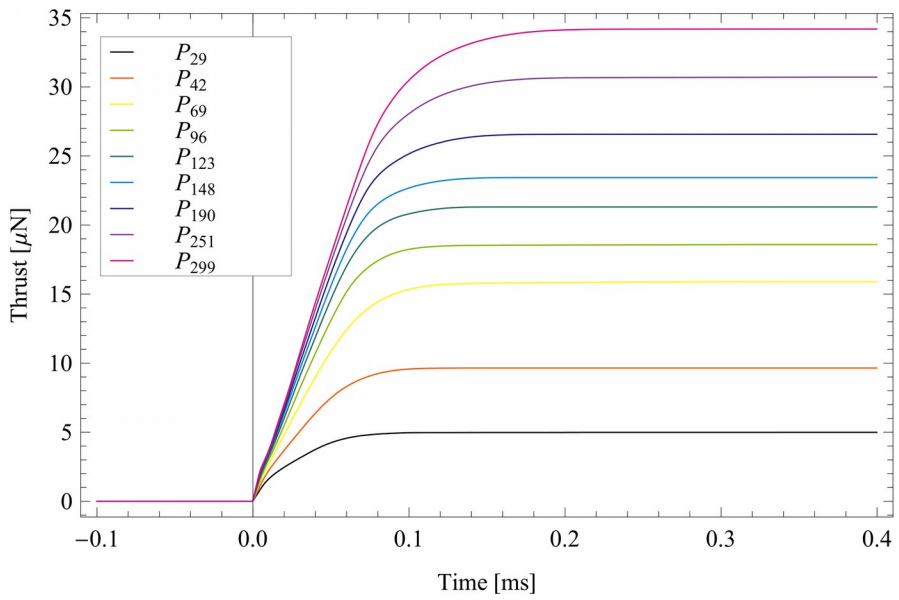
Figure 37. Cumulative thrust

All the relevant information about the characteristics of the electrospray are summarized in Tables III an IV, the thrust, I_{sp} and ξ are obtained using the flux obtained by TOF analysis.

On table III we can compare the values of mass flow for TOF analysis and using microfluidics, using the nominal depth of the channels (20 μm) the flux is overestimated. If instead of the nominal depth we use 17 μm, both flow estimates are very close. The possibility of having a swallower channel is plausible, the depth of the channels are time controlled and checked with a contact profilometer on the wider channels (we known that the etching rate of a DRIE system is geometry dependent, narrower features are etched at slower velocity).

The values of flux and current are comparable to previous characterization studies of the behavior of Emi-Im, Gamero-Castaño [75] reports that Emi-Im electrosprays emitting currents between 215-300 nA have a corresponding flow of $9.04 \cdot 10^{-14}$-$2.3 \cdot 10^{-13}$ m^3/s.

The results of I_{sp} and charge to mass ratio are typical for electrosprays where the ions are a small portion of the flux, the portion of ions can be increased by adjusting the flow and the voltage to promote the closing of the jet to reduce the creations of droplets and promote ion evaporation.

If we compare the array of thrusters to previous works the most notorious result is that the maximum propulsive efficiency of the thruster head is the maximum reported for microfabricated arrays [20]–[22], [68] and the maximum total thrust and thrust per emitter is only exceeded by arrays with a secondary acceleration grids that provide a total accelerating voltage four times the one used by our system [21] at the same time their configuration use microbeads to create flow resistance and the array have a significant

Table III. Flow properties of the electrospray head. Total mass flow rate from TOF analysis $\dot{m}_{TTOF}$ [kg/s], mass flow rate per emitter $\dot{m}_{TOF}$ [kg/s], total mass flow rate from microfluidic analysis $\dot{m}_{ch}$ [kg/s], total mass flow rate from microfluidic analysis with 17 μm deep channels $\dot{m}_{ch2}$ [kg/s], total volumetric flow rate (TOF analysis) Q_{Tot} [m^3/s] and volumetric flow rate per emitter $Q_{Emitter}$ [m^3/s]

ΔP	$\dot{m}_{TTOF}$	$\dot{m}_{TOF}$	$\dot{m}_{ch}$	$\dot{m}_{ch2}$	Q_{Tot}	$Q_{Emitter}$
29	2.07·10^{-9}	3.23·10^{-11}	3.88·10^{-9}	2.88·10^{-9}	1.36·10^{-12}	2.13·10^{-14}
42	4.8·10^{-9}	7.50·10^{-11}	5.62·10^{-9}	4.17·10^{-9}	3.16·10^{-12}	4.93·10^{-14}
69	9.82·10^{-9}	1.53·10^{-10}	9.24·10^{-9}	6.85·10^{-9}	6.46·10^{-12}	1.01·10^{-13}
96	1.09·10^{-8}	1..70·10^{-10}	1.29·10^{-8}	9.53·10^{-9}	7.17·10^{-12}	1.12·10^{-13}
123	1.28·10^{-8}	2.00·10^{-10}	1.65·10^{-8}	1.22·10^{-8}	8.42·10^{-12}	1.32·10^{-13}
148	1.46·10^{-8}	2.28·10^{-10}	1.98·10^{-8}	1.47·10^{-8}	9.60·10^{-12}	1.50·10^{-13}
190	1.81·10^{-8}	2.83·10^{-10}	2.54·10^{-8}	1.89·10^{-8}	1.19·10^{-11}	1.86·10^{-13}
251	2.53·10^{-8}	3.95·10^{-10}	3.36·10^{-8}	2.49·10^{-8}	1.66·10^{-11}	2.60·10^{-13}
299	2.81·10^{-8}	4.39·10^{-10}	4.00·10^{-8}	2.97·10^{-8}	1.85·10^{-11}	2.89·10^{-13}

Table IV. Physical properties of the electrospray for each pressure. Total current I_{tot} [μA], current per emitter $I_{emitter}$ [nA], total thrust T_{Tot} [μN], thrust per emitter $T_{emitter}$ [nN], average specific charge ξ [C/kg], specific impulse I_{sp} [s] and thrusting efficiency η

ΔP	I_{Tot}	$I_{emitter}$	T_{Tot}	$T_{emitter}$	ξ	I_{sp}	η
29	6.52	102	4.99	78	3142	245	51%
42	8.72	136	9.65	151	1816	205	62%
69	11	172	15.91	249	1119	165	65%
96	12.57	196	18.59	290	1152	174	70%
123	14.2	222	21.31	333	1112	170	69%
148	15.21	238	23.43	366	1041	163	69%
190	16.52	258	26.57	415	913	150	66%
251	18.14	283	30.71	480	772	133	57%
299	19.60	306	34.19	534	697	124	59%

amount of malfunctioning emitters. The specific impulse is in the lower range of the existing thruster heads, however Shea [22], [68] focused his research in obtaining a source of pure ions but up to this date this has resulted in poor thrust efficiency and extremely low thrusts.

In future works we also expect to integrate a secondary array to increase the total thrust, specific impulse and efficiency of our thrusting system, the importance of the voltage loss at the jet is reduced if we increase the total accelerating voltage using a secondary electrode.

III.5 Conclusions

We have analyzed two sets of devices, a single emitter: proof of concept device and HC-1 and fully functional 64 multiplexed sources HC-2 and HC-3. From the results we conclude:

- Electrospray atomization can be attained by microfabricated emitters, even if their geometric aspect ratio is close to 1

- The use of microfluidic channels is the optimal solution to create the desired flow resistance

- Our multiplexed array can operate continuously for 12h, the longest reported operating time for microfabricated arrays

- The maximum thrust, specific impulse, specific charge and thrust efficiency are 34 μN, 245 s, 3142 C/kg and 70%. The efficiency is also the highest reported for microfabricated arrays

Chapter IV

Physical sputtering of semiconductors by electrosprayed nanodroplet bombardment

T he size of the projectiles has important effects on how an ion beam interacts with a target, and extending the range of this parameter beyond atomic dimensions offers opportunities in both research and technological applications. For example, the size of gas cluster ions and their relatively low specific charge compared to atomic ions are credited with the high sputtering yields, dense energy deposition and shallow surface damage typical of cluster ion beams[44]; large projectile sizes are correlated with the ability to desorb large molecules in secondary ion mass spectrometry[76]; and the theoretical study of the energetic impact of cluster ions and larger nanoparticles has become a problem of interest[77]. Gas cluster ions are the largest projectiles available but, due to their low charging level (one elementary charge), their effective diameters are limited to a few nanometers (e.g. a large Ar^+_{2000} gas cluster ion has a diameter of 5.6 nm).

In this chapter we present how electrosprayed nanodroplets are efficient sputtering projectiles. Sputtering yields of 2.3, 1.5, and 2.3 atoms ejected per projectile molecule have been reported respectively for single-crystal silicon, poly crystalline silicon carbide and boron carbide. The associated sputtering rates of 448, 172 and 170 nm/min far exceed the physical sputtering of broad-beam ion sources[10]. Besides sputtering these energetic beamlets are known to amorphatize the surface of single crystal silicon, a phase transition

caused by the dissipation of energy in the area surrounding the impact, and the subsequent melting and ultrafast quench of the solid phase[13], [78]. This chapter extends the initial research on nanodroplet sputtering to other single-crystal semiconductors, including indium arsenide, indium phosphide, germanium, gallium arsenide, gallium antimonide, gallium nitride and silicon carbide. The chapter quantifies the sputtering yield, sputtering rate and surface roughness of these semiconductors as functions of the nanodroplet velocity. Anisotropic etching of single-crystal GaN and SiC at the high rates demonstrated in Si is especially attractive for these technologically important wide bandgap semiconductors, due to their remarkable chemical stability and resistance to etching[43]. The chapter also studies the influence of projectile dose on the sputtering yield and the surface roughness of single-crystal Si.

IV.1 Experimental apparatus and methods

Emi-Im, is electrosprayed to produce a beam of charged nanodroplets. This liquid has been employed in sputtering research[10], [11], and its electrosprays have been characterized in vacuum. Figure 38 shows a sketch of the experimental setup. The electrospray source is a platinum tube with an inner diameter of 0.16 mm and an outer diameter of 0.48 mm. The tip is chamfered at an angle of 45° to reduce the base of the Taylor cone down to the tube's inner diameter, which promotes the higher atomization stability associated with a reduced cone volume. The platinum tube is crimped to a fused silica tube that takes the fluid from an external bottle to the emission tip located inside the vacuum chamber, which pressure is kept in the low 10^{-6} Torr range. The fused silica tube, having an inner diameter of 40 μm,

also increases the hydraulic impedance so that a conveniently high pressure difference relative to the typical capillary and electrostatic pressures in the Taylor cone, as well as the resolution of the pressure gauge, must be used to drive the flow. The platinum emitter is connected to a high voltage power supply of negative polarity with respect to a grounded extractor electrode. A voltage difference of -2150 V between emitter and extractor, V_E, is used in every experiment to set the electrospray. A fraction of the beam is skimmed by an orifice in the axis of the extractor (0.64 mm in diameter, 3.0° half-cone angle aperture with respect to the emission point), and this beamlet is directed towards the sputtering target. The target is mounted on an XYZ positioner, its surface is normal to the beamlet axis and placed 4 mm from the extractor during the sputtering experiments, and is connected to a high voltage power supply of positive polarity. The potential of the target V_T can be increased up to 25 kV to accelerate the projectiles. The net acceleration potential V_A of the projectiles is the sum of the emitter and extractor potentials. All experiments are performed under identical electrospraying conditions: the pressure difference driving the flow is 200 Torr, yielding a total beam current I_E of 283±4 nA; the current of the beamlet I_B impacting on the target is 19 nA; the beamlet was characterized via time of flight to measure its mass flow rate, $\dot{m}_B$ = 1.65x10^{-11} kg/s, the percentage of the current carried by the droplets, 84%, and their average specific charge, $\langle\xi\rangle$ = 971 C/kg. The estimated droplet average diameter is 27 nm[79]. The average impact velocity is readily estimated with the average specific charge and the acceleration voltage $\upsilon = (2\langle\xi\rangle V_A)^{1/2}$. The typical kinetic energy of an Emi-Im molecule in the nanodroplet is $E_m = m_m \langle\xi\rangle V_A$, where m_m is the molecular mass of Emi-Im, 391.12 amu. The stagnation pressure of the projectile is $P = \rho \langle\xi\rangle V_A$, where ρ is the density of Emi-Im, 1520 kg/m^3. The acceleration voltage was varied between 6.1 and

26.6 kV, yielding impact velocities, molecular energies and stagnation pressures ranges of 3.4 km/s to 7.2 km/s, 24 eV to 105 eV, and 9.1 GPa to 39 GPa

All targets are single-crystal wafers purchased from El-Cat Inc. The Si, Ge, GaAs, GaSb, InAs and InP targets are 2" wafers with [100] orientation. The SiC targets are 10x10x0.43 mm hexahedrons of the 6H polytype, and [0001] orientation. The GaN target is a 100 μm thick epilayer of this semiconductor with a [0001] orientation, grown on a 2" sapphire wafer.

The sputtering yields are calculated with the formula:

$$Y = \frac{m_m}{\dot{m}_B \tau} \frac{n_c \rho_C V}{m_C}$$
(33)

where ρc is the density of the crystal; V is the volume of the target carved by the beamlet, which is measured with a profilometer; n_c is the number of different chemical elements present in the crystal, and m_c is the sum of their masses; τ is the time during which the beam strikes the surface. The sputtering rate is defined by:

$$R = \frac{V}{A \tau}$$
(34)

where A is the area of the spot carved by the beamlet. The sputtering yield and rate, as well as the surface roughness, are measured in areas carved by the beamlet during 600 s. The target is repeatedly moved while resetting the target potential, to generate an array of spots carved at different acceleration voltages. In a second type of experiments designed to study the effect of projectile dose the bombardment is varied between 10s and 600 s. The roughness of the bombarded surface is measured with an Atomic Force Microscope, AFM. The roughness is computed as the root mean square of the heights of the surface points.
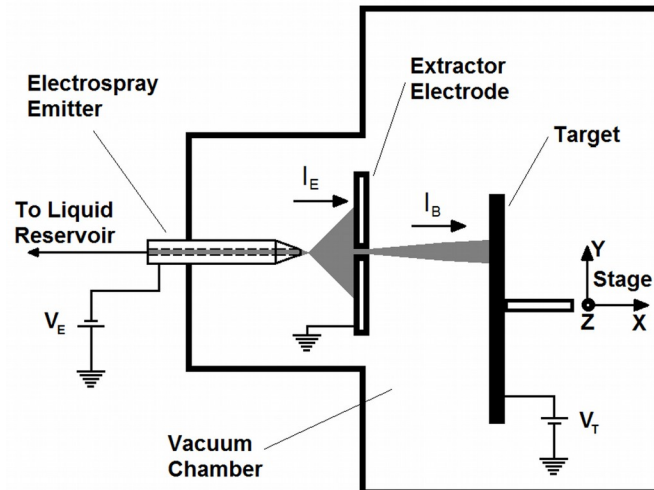
Figure 38. Diagram of the experimental setup. An electrospray source operating inside a vacuum chamber atomizes a liquid into charged nanodroplets, a fraction of which is accelerated by an electrostatic field and directed against a sputtering target. *Reprinted with permission from R. Borrajo-Pelaez, E. Grustan-Gutierrez and M. Gamero-Castaño, Sputtering of Si, SiC, InAs, InP, Ge, GaAs, GaSb, and GaN by electrosprayed nanodroplets, Journal of Applied Physics, 114, 184304. Copyright 2013, AIP Publishing LLC*

IV.2 Results and discussions

Figure 39 shows photographs of the Si, SiC and Ge targets bombarded at several acceleration potentials, and surface profiles for the Si target. In all cases the beamlet carves a flat circular depression surrounded by a deeper ditch. The diameter of these macroscopic craters decreases at increasing acceleration voltage because the axial electric field between the extractor and the target, being proportional to acceleration voltage, reduces the polar angle of the particle trajectories exiting the extractor orifice. Typical crater diameters for low and high acceleration potentials are 1 mm and 0.3 mm respectively. The depth of the

craters augments with acceleration voltage because of the positive correlation between sputtering yield and molecular kinetic energy, and the reduction of the crater area at increasing acceleration potential. For example, the depths of the Si, SiC and Ge targets are 0.9, 0.7 and 5.6 ㎜m at 14.6 kV acceleration voltage, and 3.7, 5.8 and 22.4 ㎜m at V_A = 24.6 kV. Besides these trends common to all target materials there are substantial differences between the Si surfaces in one hand, and the surfaces of SiC and Ge (all other semiconductors behave like SiC and Ge). First, the Si craters are surrounded by substantial deposits in the form of circular iridescent rings forming a Newton color series, which are much less noticeable in other materials. These and similar experiments with other liquids suggest that the projectile's imide group has an affinity for associating with Si into charged compounds, which are pushed back to the target by the electric field. The roughness of the surfaces is also markedly different. The AFM profiles for Si show surfaces covered by micrometric craters with sizes that increase with the acceleration voltage up to 15 kV. These craters are large, e.g. the typical diameter and depth at V_A=14.6 kV are 2-3 μm and 0.5 μm respectively, orders of magnitude larger than the average diameter of the nanodroplets. These micrometric and intertwined craters produce very rough surfaces, clearly noticeable in the photographs at 12.1 kV and 14.6 kV by the high scattering of light (the photographed samples are illuminated at a glancing angle). At still higher acceleration potential the surface of Si becomes specular, and is occasionally dotted by very large, isolated craters. The surfaces of all other materials also exhibit craters but these are significantly smaller, and their sizes and density do not vary with the acceleration voltage as much as in Si.
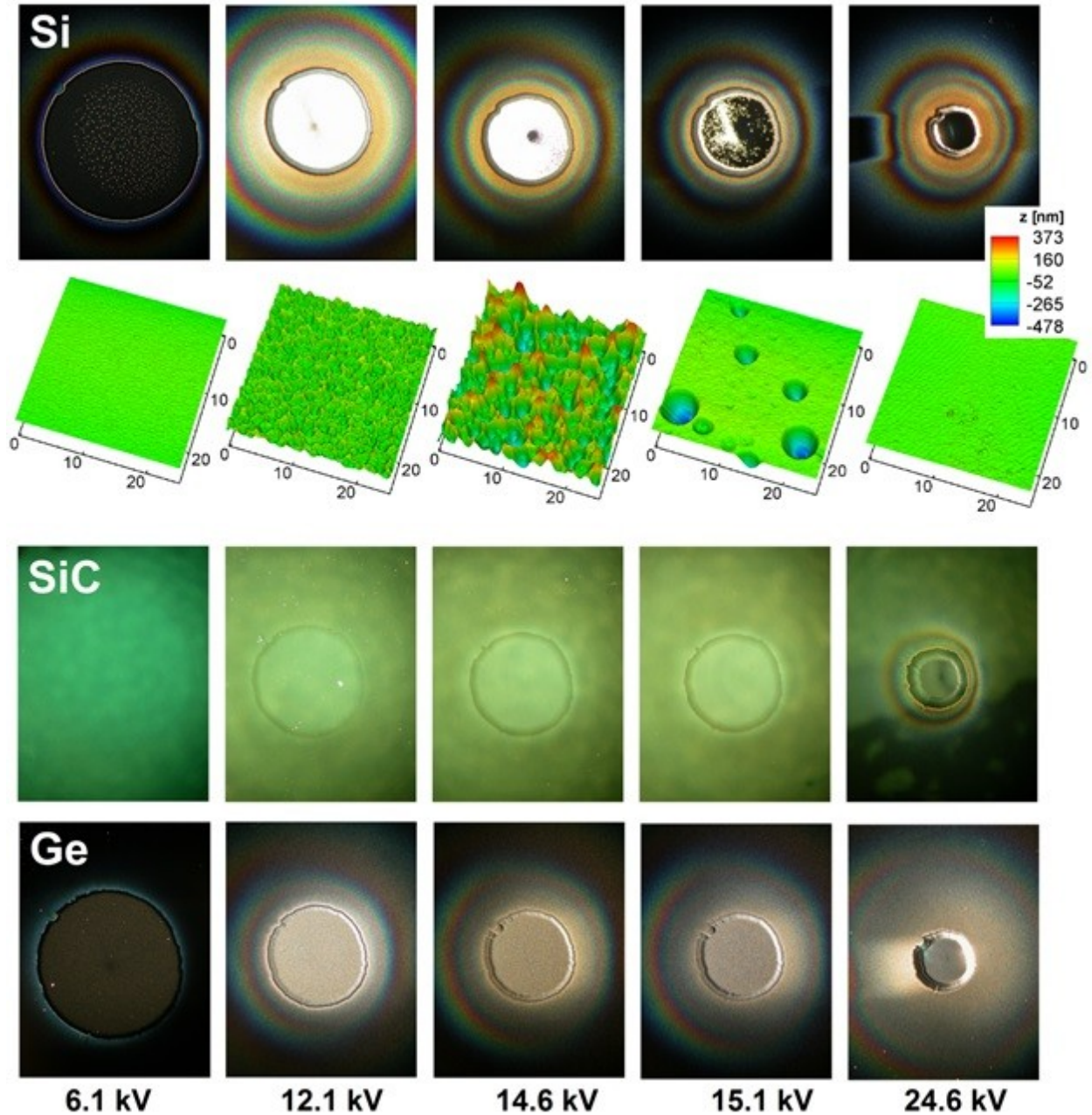
Figure 39. Photographs of Si, SiC and Ge target areas struck by the beamlet during 600 s, at varying acceleration potential. The Si photographs are complemented with atomic force microscopy of the bombarded surfaces. *Reprinted with permission from R. Borrajo-Pelaez, E. Grustan-Gutierrez and M. Gamero-Castaño, Sputtering of Si, SiC, InAs, InP, Ge, GaAs, GaSb, and GaN by electrosprayed nanodroplets, Journal of Applied Physics, 114, 184304. Copyright 2013, AIP Publishing LLC*

Figure 40. Roughness of the bombarded samples as a function of acceleration potential. Silicon behaves differently from all other materials. *Reprinted with permission from R. Borrajo-Pelaez, E. Grustan-Gutierrez and M. Gamero-Castaño, Sputtering of Si, SiC, InAs, InP, Ge, GaAs, GaSb, and GaN by electrosprayed nanodroplets, Journal of Applied Physics, 114, 184304. Copyright 2013, AIP Publishing LLC*
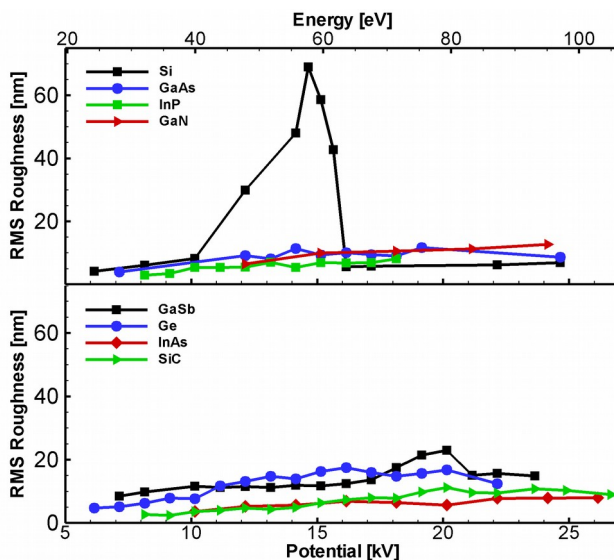
Figure 40 plots the roughness of the surfaces struck by the beamlet. The roughness of Si increases sharply with acceleration voltage, reaching a maximum value of 69 nm at 14.6 kV; at higher acceleration voltage the surface becomes much smoother. The roughness of all other materials increases slowly with acceleration voltage and, in some cases, levels off or slightly decreases at the highest acceleration voltages; the values are substantially lower than the peak roughness for Si. Note that germanium also follows this monotonic trend, despite being an element closely related to silicon. The maximum roughness for GaN, GaAs, GaSb, InP, InAs, Ge and SiC are 12.7, 11.7, 19.5, 8.1, 7.9, 17.5 and 11.2 nm respectively. The AFM profiles in figure 41 show the patterns of impacts behind the surface roughness of different materials, and the singular behavior of Si. The surfaces of GaN, SiC and Ge in the bottom row are typical of all semiconductors except for Si: the surfaces have small

indentations with diameters of the order of 0.1 mm and depths of a few tens of nanometers, and which must be the dimples left by individual droplets impacting on the surface. The Si targets also display this pattern of small indentations, but at acceleration voltages between 10.1 kV and 15.1 kV these small marks are superimposed over an additional pattern of much larger craters, which dominate the surface roughness. Each large crater must be
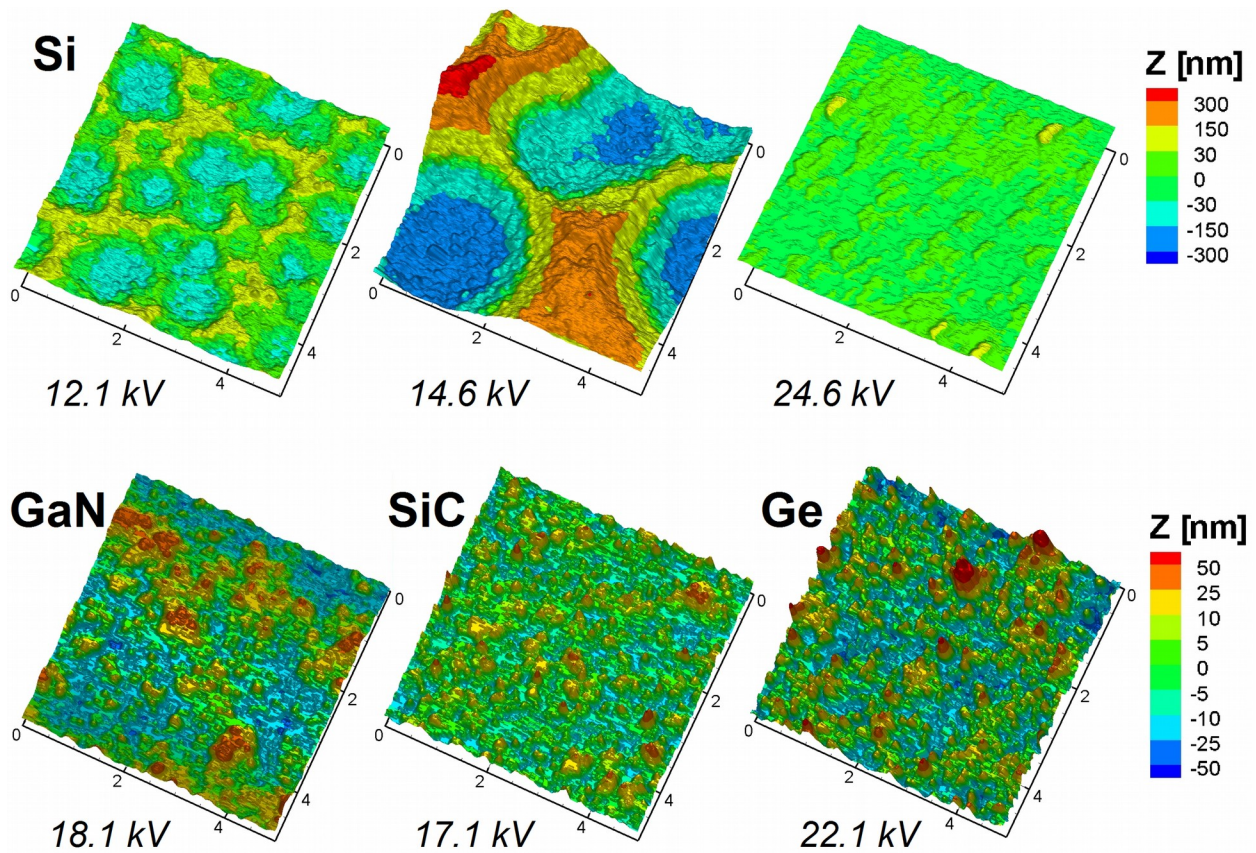
Figure 41. Atomic force microscope measurements of Si, GaN, SiC and Ge samples. The impacts of individual droplets produce a pattern of small indentations in all surfaces. In addition, a very few number of impacts produce large craters in Si, at acceleration potentials between 10 kV and 15 kV. *Reprinted with permission from R. Borrajo-Pelaez, E. Grustan-Gutierrez and M. Gamero-Castaño, Sputtering of Si, SiC, InAs, InP, Ge, GaAs, GaSb, and GaN by electrosprayed nanodroplets, Journal of Applied Physics, 114, 184304. Copyright 2013, AIP Publishing LLC*

produced by the single impact of a projectile that is not much larger than the average droplet (2 orders of magnitude smaller than the large craters): we have never detected large droplets in these beams despite a thorough investigation with an induction charge detector[79]; and large droplets, far exceeding the Rayleigh charge limit at the required specific charge, would be unstable.

Figure 42 shows sputtering yields as a function of acceleration voltage, and projectile's molecular kinetic energy. The sputtering yields increase monotonically with molecular energy, leveling off at approximately 70 eV in most materials. The yields for GaAs, InAs and GaSb decrease slightly at the highest acceleration voltages. The maximum sputtering yields for Si, GaN, GaAs, GaSb, InP, InAs, Ge and SiC are 2.2, 2.2, 4.2, 4.1, 4.1, 3.6, 4.5 and 1.9 atoms per projectile's molecule respectively. These values are similar to the maximum sputtering yields of atomic projectiles, and significantly higher than those of gas cluster ions. For instance, the sputtering yields of Si and SiC bombarded by atomic argon at normal incidence and 500 eV, approximately one order of magnitude over the range of projectile energy in the present work, are 0.4 and 0.8 [80], [81]; the sputtering yields of Si and SiC struck by Ar^+_{2000} gas cluster ions at 20 kV acceleration potential are 0.008 and 0.013 [82]. As in the case of the surface roughness, the dependence of the sputtering yield on acceleration voltage differs significantly between Si and other materials. Rather than increasing monotonically with acceleration voltage, the sputtering yield of Si first increases with acceleration voltage, peaks at 12.1 kV, and abruptly decreases at 14.6 kV to remain nearly constant thereafter. The sharp drop in sputtering yield precedes the drop in surface roughness by 1 kV.
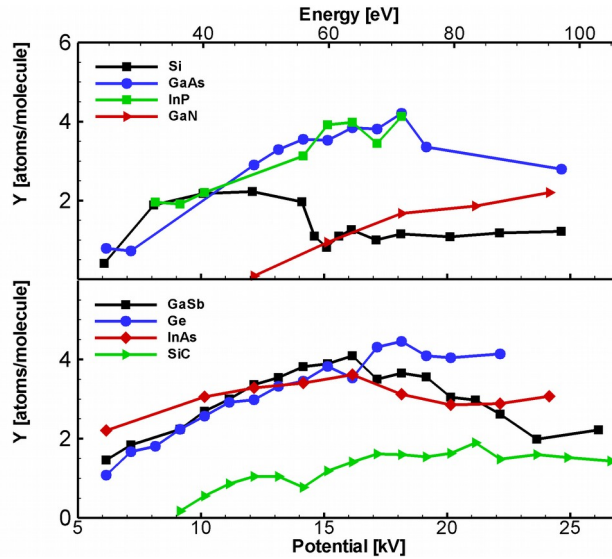
Figure 42. Sputtering yields as a function of acceleration potential. The maximum sputtering yields of all semiconductors are comparable. The maximum values between 2 and 4 atoms per projectile's molecule are substantially higher than those of gas cluster ions at similar acceleration potentials. *Reprinted with permission from R. Borrajo-Pelaez, E. Grustan-Gutierrez and M. Gamero-Castaño, Sputtering of Si, SiC, InAs, InP, Ge, GaAs, GaSb, and GaN by electrosprayed nanodroplets, Journal of Applied Physics, 114, 184304. Copyright 2013, AIP Publishing LLC*

Figure 43 shows sputtering rates, a figure of merit which, being proportional to the particle flux, depends on factors such as beam focusing, emitter density, etc. In our experiments the flux is only a function of the acceleration voltage, making it possible to compare the sputtering rates on different targets at constant acceleration voltage. The sputtering rate increases monotonically with acceleration voltage because both the particle flux and the sputtering yield increase with this parameter. The sputtering rates for Ge, GaSb and GaAs at 20 kV exceed $1\mathrm{mm/min}$, a value typical of reactive ion etching and orders of magnitude higher than what is achievable with ion beam milling. The maximum sputtering rates for SiC and GaN, 0.41 and 0.63 $\mathrm{mm/min}$, are similar to the best rates possible with

reactive ion etching (0.97 ㎜m/min for SiC, 1.3 ㎜m/min for GaN), and significantly higher than the rates associated with the more comparable ion beam milling technique (below 0.01 ㎜m/min for GaN)[43].

In an ongoing molecular dynamics study of the impact of an isolated nanodroplet on single-crystal Si we have determined that thermal evaporation is the main sputtering mechanism. The simulations show how a thin layer of Si starts melting at a projectile molecular energy of approximately 18 eV, and that the temperature and thickness of the layer increase with the velocity of the projectile[83]. The atoms emitted from this molten surface have a Maxwellian distribution, their temperature is very near that of the surface, and the emission rate has the expected exponential dependence on temperature. Other
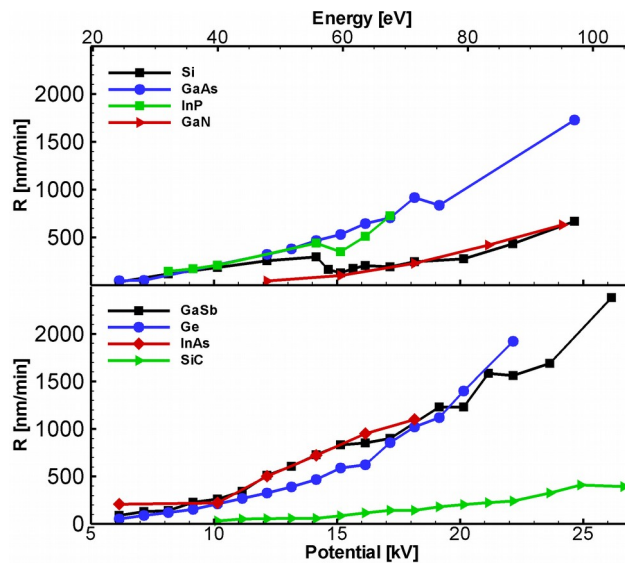
Figure 43. Sputtering rates versus acceleration potential. The sputtering rates in these experiments are similar to the values yielded by reactive ion etching, and orders of magnitude higher than in the more comparable ion beam milling process. *Reprinted with permission from R. Borrajo-Pelaez, E. Grustan-Gutierrez and M. Gamero-Castaño, Sputtering of Si, SiC, InAs, InP, Ge, GaAs, GaSb, and GaN by electrosprayed nanodroplets, Journal of Applied Physics, 114, 184304. Copyright 2013, AIP Publishing LLC*

mechanisms are likely contributing to the removal of material as well. In the case of Si it is apparent that, besides sputtering, the projectiles are damaging the target and that the accumulation of this damage leads to a sputtering yield higher than in the original target surface. The large craters in figures 39 and 41 support this idea: only a small number of impacts generate these large craters because otherwise the sputtering yield would be orders of magnitude higher than what is measured; and, since all projectiles are similar, the conditions of the surface where the large craters appear must be substantially different from that of the original target.

The effect of the projectile dose on the damage exacted on Si is further illustrated in Figure 44. In these experiments the beamlet strikes a spot during a predetermined time, which is varied between 10 s and 600 s. The projectile dose is proportional to this time. The experiments are done at 12.1 kV and 18.1 kV acceleration potentials, to produce conditions that cause intertwined microscopic craters with high surface roughness and a smooth specular surface, respectively (see Fig. 2). The droplet number fluxes are estimated at $3.8x10^{15}$ m^{-2}s^{-1} and $7.3x10^{15}$ m^{-2}s^{-1} and, with an average droplet diameter of 27 nm, it takes about 0.47 s and 0.25 s for the beamlet to uniformly strike the surface with at least one impact. The photographed samples are illuminated along the line of sight and, since a rough surface scatters light effectively in all directions, the rougher the surface the darker the bombarded area is. The photographs and the associated plots show how the surface roughness for the 12.1 kV beamlet increases with dose until it saturates at an exposure time of approximately 300 s, i.e. the formation of the large craters typical of Si requires exceeding a critical projectile dose. Conversely the roughness caused by the 18.1 kV beamlet, and the sputtering yields for either acceleration voltage, do not depend on the
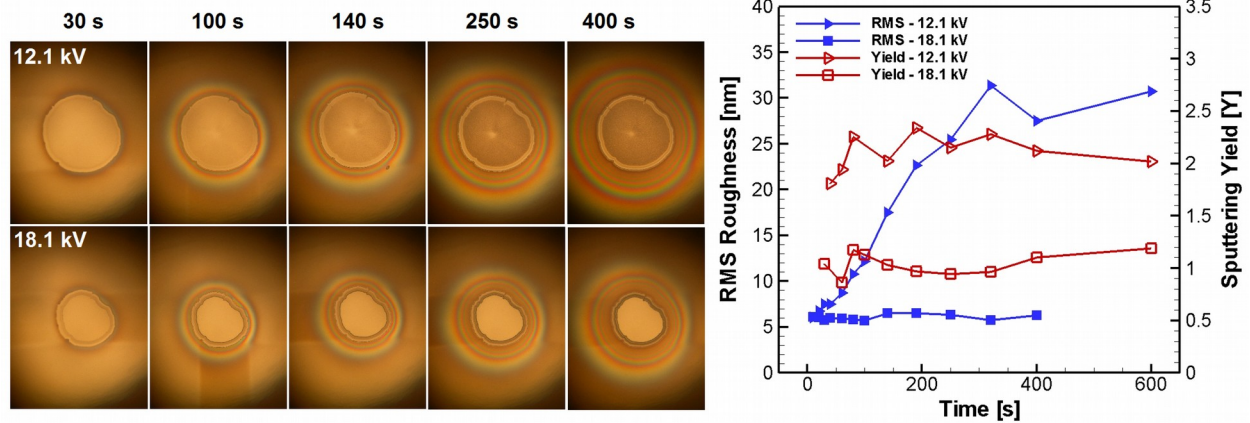
Figure 44. The effects of projectile dose on the surface roughness and sputtering yield of Si, at 12.1 kV and 18.1 kV beamlet acceleration potentials. *Reprinted with permission from R. Borrajo-Pelaez, E. Grustan-Gutierrez and M. Gamero-Castaño, Sputtering of Si, SiC, InAs, InP, Ge, GaAs, GaSb, and GaN by electrosprayed nanodroplets, Journal of Applied Physics, 114, 184304. Copyright 2013, AIP Publishing LLC*

projectile dose. These results suggest a link between the accumulation of damage induced by consecutive impacts, and the formation of the very large craters characteristic of Si, which dominate the surface roughness when present. Furthermore, since the ejection of Si from these large craters does not have a significant contribution to the sputtering yield, the frequency at which they form is much lower than the rate at which the projectiles impact.

IV.3 Conclusions

We have measured the sputtering yield and rate of several single-crystal semiconductors bombarded by a beamlet of electrosprayed nanodroplets at varying acceleration potential. We have also quantified the roughness of the target surfaces, and the effect of projectile dose in the case of Si. The main results are summarized as follows:

- The maximum sputtering yields for Si, SiC, Ge, GaAs, GaSb, GaN, InP and InAs are 2.2, 1.9, 4.5, 4.2, 4.1, 2.2, 4.1 and 3.6 target atoms per projectile's molecule, respectively. The corresponding sputtering rates are 0.25, 0.22, 1.02, 0.92, 0.85, 0.63, 0.39 and 0.95 μm/min.

- The surface roughness typically increases with the acceleration potential. The variation is gradual and narrow for most of the materials, with rms values between 2 nm and 20 nm. Silicon exhibits a singular behavior: the roughness peaks at 69 nm at an intermediate potential, and sharply drops at higher potentials; and some impacts produce craters several orders of magnitude larger than the projectile.

- The formation of the very large crater impacts typical of Si at acceleration potentials between 12.1 kV and 18.1 kV requires exceeding a threshold projectile dose. This suggests a link between consecutive projectile impacts and the accumulation of damage in the target.

Chapter V

Fast etching of microscale structures by bombardment with electrosprayed nanodroplets

C hemically driven dry etching processes such as Reactive Ion Etching (RIE) and Deep Reactive Ion Etching (DRIE) are industry standards due to their ability to produce anisotropic structures at a fast etching rate for a wide range of semiconductor substrates. However, reactive processes are much less efficient in the case of inert materials resistant to chemical attack such as the technologically interesting SiC and GaN [36], [37], [84]–[87]; physical sputtering is a comparable alternative for carving these chemically resistant substrates.

Ion Beam Milling (IBM) is a well-established technique that relies on physical sputtering, producing etching rates below 10nm/min [43]. The main reason for the limited etching rate is that the space charge density between the plasma and accelerator grids limits the number of particles hitting the target surface. Replacing the small atomic ions used in IBM by the bigger cluster ions increases the molecular flux and subsequently the etching rate [82]. The use of even larger nanodroplets as projectiles is a natural extension of the increased sputtering by gas cluster ions. Beams of charged droplets with diameters ranging from a few nanometers to tens of microns can be generated in a vacuum by electrospraying ionic liquids. The liquid atomization in the cone-jet mode results in droplets with narrow size and charge distributions [48], with average values that can be

controlled through the flow rate and the physical properties of fluid. These nanodroplets can be accelerated to velocities exceeding several km/s before impacting on a target. In prior works we have reported the effect of the impact velocity on the sputtering yield, surface roughness and etching rate of the process, obtaining rates over one order of magnitude higher than the ones typical of IBM, e.g. 667, 410 and 630 nm/min for Si, SiC and GaN respectively [10]–[12]; ongoing research using higher energies yields rates greater than some of the highest etching rates observed by reactive plasma [88], [89]. Besides sputtering, it has been observed that a thin layer of the substrate is amorphatized upon bombardment of the surface [13], [83]. This article introduces the use of masks to carve microscale structures by means of electrospray bombardment. The results obtained with organic and metallic masks are compared. We study the influence of the electric conductivity on the selectivity and wall profile. Silicon is used as a benchmark to test the capabilities of the present techniques to carve a wider range of inert substrates. We also discuss the non-linearity of the etching rate and selectivity for gold masks on silicon substrates as well as the applicability of this method to etch SiC and GaN. Finally a thick layer of photoresist is used as a mask to carve complex patterns.

V.1 Experimental apparatus and methods

Beams of charged nanodroplets are created by electrospraying the ionic liquid Emi-Im. The experimental setup is shown in figure 45. The electrospray emitter is placed inside a vacuum chamber maintained at a base pressure of $5 \cdot 10^{-6}$ Torr. The emitter is a platinum tube with 0.16mm and 0.48 inner and outer diameters; its tip has been chamfered at 45° to
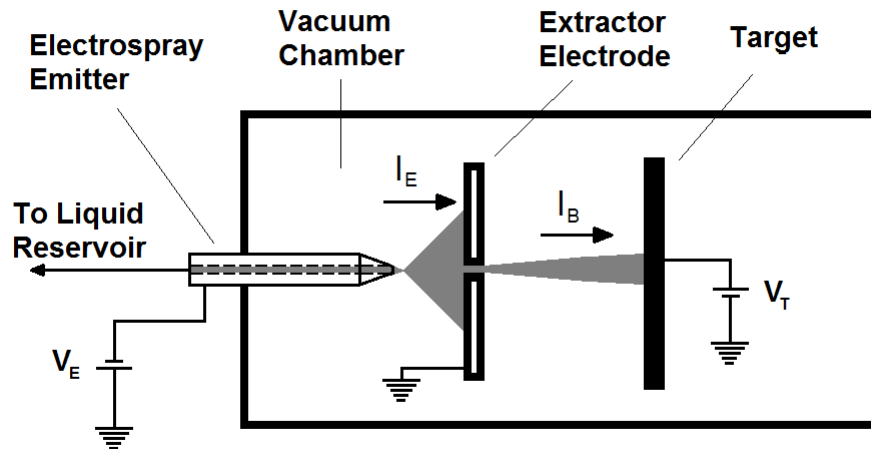
Figure 45. Experimental setup. An electrospray emitter inside a vacuum chamber atomizes an ionic liquid. A fraction of the beam is accelerated towards the target by the extractor and target electric potentials

reduce the dimensions of the Taylor cone. The emitter source is connected to an external reservoir containing EMI-Im through a 40μm inner diameter silica tube. A more detailed description of the experimental setup can be found in the previous chapter.

In order to set the ionic liquid flow and consequently the current of the electrospray, I_E, a higher pressure is applied inside the external reservoir. The platinum emitter is connected to a voltage supply while the facing extractor electrode is grounded imposing a voltage difference V_E between them to set the electrospray.

A fraction of the beam, I_B, is sampled through an orifice at the center of the extractor and impacts the surface of the intended target. The target is placed at 4 mm from the extractor and connected to a high voltage power supply. The V_T target potential further accelerates the projectiles prior to the impact. The total accelerating voltage is therefore

$$V_A = V_T + V_E \tag{35}$$

The etching rate, yield and surface roughness can be modified by adjusting the projectile velocity which is determined by

$$v_d = \sqrt{2 \langle \xi \rangle V_A} \qquad (36)$$

where ξ is the charge to mass ratio of the droplet. The kinetic energy of an Emi-Im molecule is then

$$E_m = m_m \langle \xi \rangle V_A \qquad (37)$$

with a molecular mass mm of 391.12 amu.

Two sets of experiments are performed with different electrospraying conditions; in the first a pressure difference of 360Torr yields a total current of 384±5nA; the voltage difference between emitter and extractor is V_E =-2220V, and the average specific charge $\langle \xi \rangle$ is 499 C/kg. The target is kept at 10kV (V_T) for a total accelerating voltage (V_A) of 12.2kV yielding a kinetic energy of 20 eV per molecule, calculated using (27). The beamlet bombards the surface of a single crystal [100] silicon target. The silicon surface has been patterned with a 2.5μm photoresist layer obtained by spinning Shipley 1827 at 4500rpm for 30". The patterns consist of 3 by 3 matrices of 10, 20 and 60 μm diameter photoresist disks, and are bombarded for 60min.

In the second set of experiments the pressure in the reservoir produces a total current of 251±3nA; the voltage of the emitter (V_E) is -1910V and the specific charge 789 C/kg. In this case the target is a single-crystal [100] silicon slice patterned by lift-off of 50nm chromium and 500nm gold layers deposited by means of E-beam evaporation. The nanodroplets are accelerated by total voltages of 12, 16, 20 and 24kV equaling 38, 51, 64

and 77 eV, striking the untreated and gold covered parts of the substrate for 10, 10, 7 and 5 minutes respectively.

To calculate the sputtered volume carved by the beamlet (V) a profilometer is used and the sputtering rate (R) is measured by

$$R = \frac{V}{A\tau} \tag{38}$$

A being the sputtered area and τ the total bombarding time.

V.2 Results and discussions

When the first incoming wave of charged nanodroplets hit the silicon slice they lose their electrical charge upon contact with the bare conductive surface while sputtering the target; however, if the projectiles arrive to a zone covered by the non-conductive photoresist the ionic liquid deposits on its surface without losing the electrical charge. Therefore the selectivity in the absence of chemical reaction between the mask and the ionic liquid (as it happens in the case of Emi-Im and Shipley1827) is virtually infinite. Furthermore, the electrically charged surface decelerates the incoming projectiles. As a consequence, liquid and sputtered debris accumulates on top of the patterned regions forming drops that shade the desired targeting areas. Eventually, the drops burst covering the surface of interest at the target with a layer of liquid, protecting the substrate from further sputtering. This phenomenon can be seen in Figure 46 and Figure 47; the features are covered with a layer of debris coming from the liquid accumulated on top of the mask. This crust coating the

features can be removed by a 30 min RCA-1 cleaning bath. However the wall profile, due to the shading produced by the droplets departs from the optimal 90° angle.

The maximum processing time at a rate of 244nm/min before the protective layer appears is 60min resulting in 15 μm high structures.

There are several options to increase the etching time and wall angle; the most direct is to find the optimal electrospraying mode and accelerating voltage that provides the fastest sputtering rate with the least amount of flux. Alternatively, a two-step process similar to the passivation and etching of the DRIE can also be pursued by physically removing the accumulated liquid on top of the mask periodically.
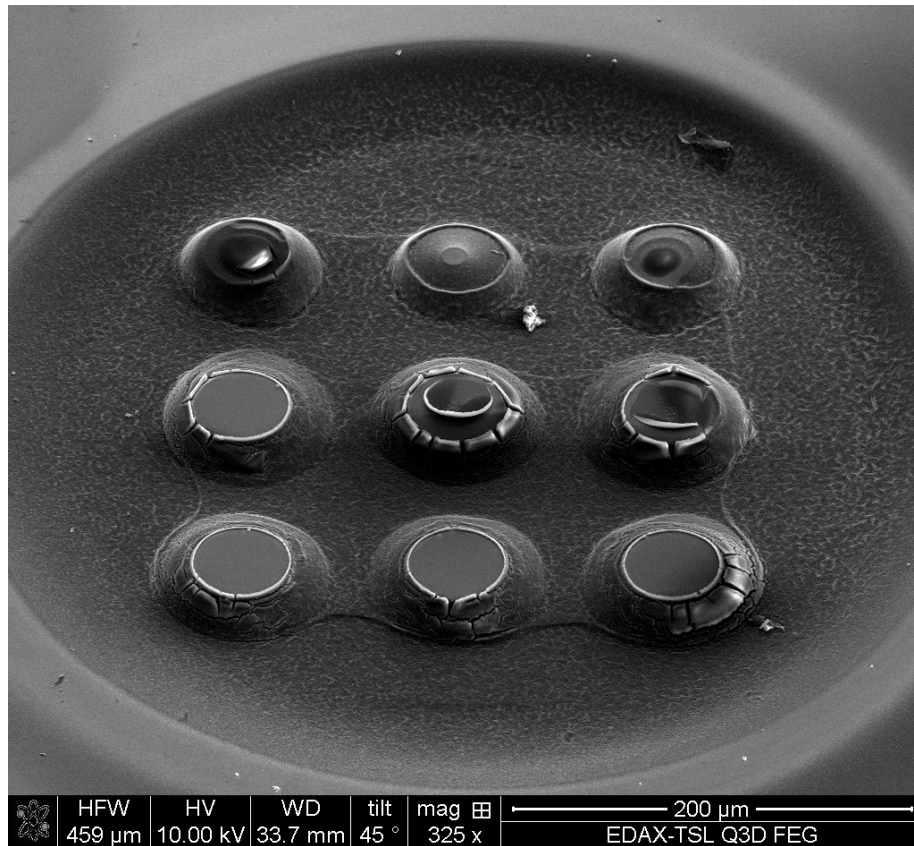
Figure 46. 3 by 3 matrix of 20 μm disks patterned using a 2.5 μm Shipley 1827 photoresist layer after being sputtered for 1h. The height of the resulting truncated cone is 15μm.
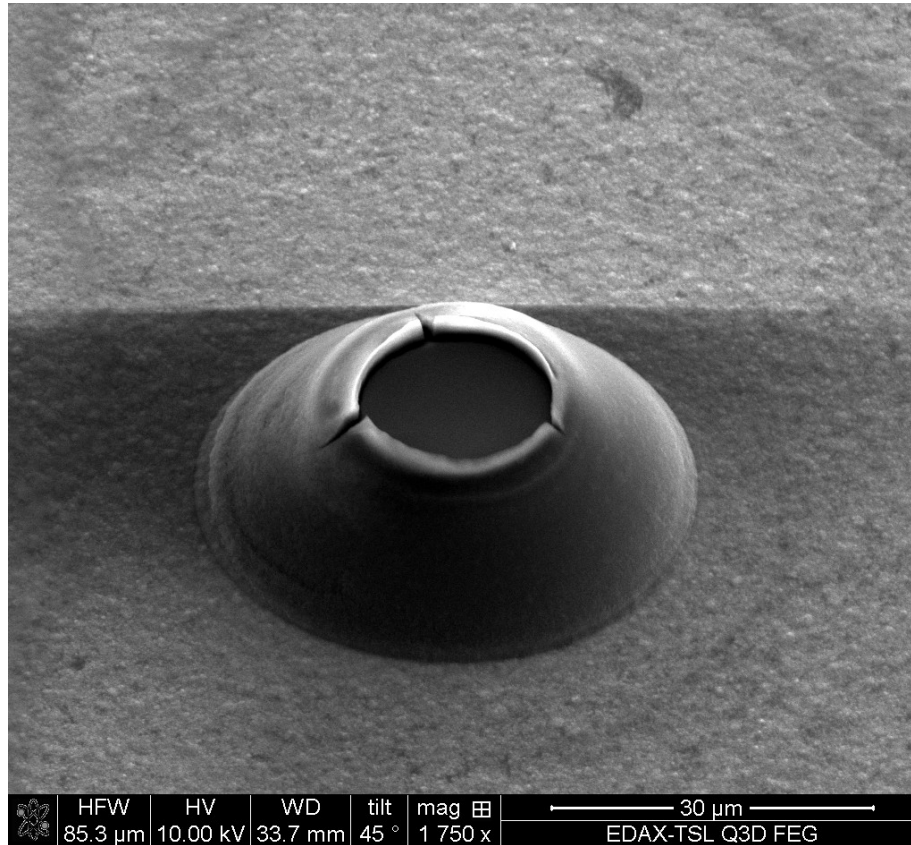
Figure 47. Detail of a 10 μm disk patterned using a 2.5 μm Shipley 1827 photoresist layer after being sputtered for 1h. The height of the resulting truncated cone is 15 μm

The use of an electrically conductive mask is another method to avoid the accumulation of liquid and the resulting shading; the mask does not offer a dielectric barrier to the incoming projectiles thus impacting the surface at their maximum kinetic energy. This clearly implies that the conductive mask will be ablated during the sputtering process; therefore, the optimal solution is to use a material that is conductive yet degrades at a much slower rate than our desired target.

Ongoing research suggests that one of the critical factors determining the sputtering velocity is the atomic mass of the target, materials with high atomic mass are etched at a slower rate; for its high atomic mass and availability gold was selected as an ablative mask.

Figure 48 presents photographs corresponding to different spots of the Au/Si target which have been carved by electrospray beams. Light is directed to the craters with low inclination with respect to the wafer surface. Hence, smooth areas of the surface appear as dark areas on the pictures, as they reflect most of the incident light away from the microscope objective with barely any normal reflection. On the contrary, rougher areas of the wafer look brighter, due to the light scattering induced by surface irregularity in random directions, including the normal from which the images are taken. At the lowest accelerating potential, and after 10 min of sputtering, the damage on the Au mask is hardly visible. In contrast the sputtered area of silicon is visibly carved and presents a rough surface. The following accelerating potential of 16kV produces noticeable contours on the processed gold (higher etching rates are found at the rim of the bombarded crater). From profilometer measurements we know that at 20 and 24kV the gold mask has been completely etched away; it is also clear how these high acceleration voltages result in dark

| 12 kV | 16 kV | 20 kV | 24 kV |
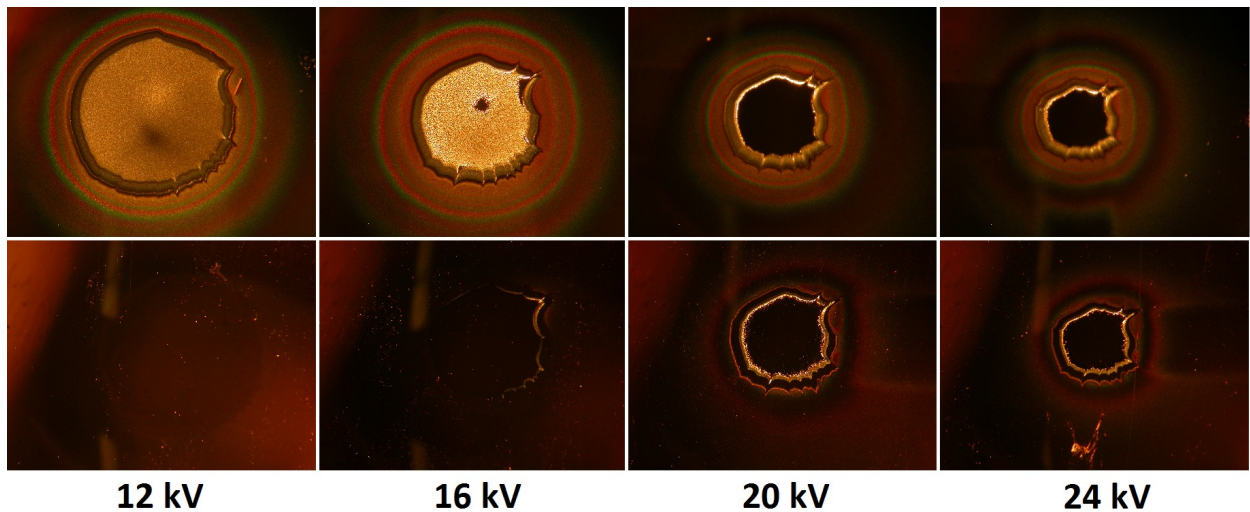
Figure 48. Comparison of the damage caused by different accelerating voltages in Si (top row) and Au (bottom row).

specular surfaces on the silicon craters, which have already been reported for this range of accelerating potentials

The silicon sputtering rates are 385, 635, 706 and 914 nm/min for 12, 16, 20 and 24 kV and for gold the results are 6, 47, 74 and 134 nm/min

The present method to suitability etch inert materials can be inferred from the results in the previous chapter. We estimate that the selectivity of gold for the range of accelerating voltages studied should improve when used in conjunction with GaAs, InP, GaSb, Ge or InAs and while for GaN the selectivity would likely be similar to the selectivity reported for Si. In the case of SiC and Au the etching rates are close to a 1 to 1 ratio.
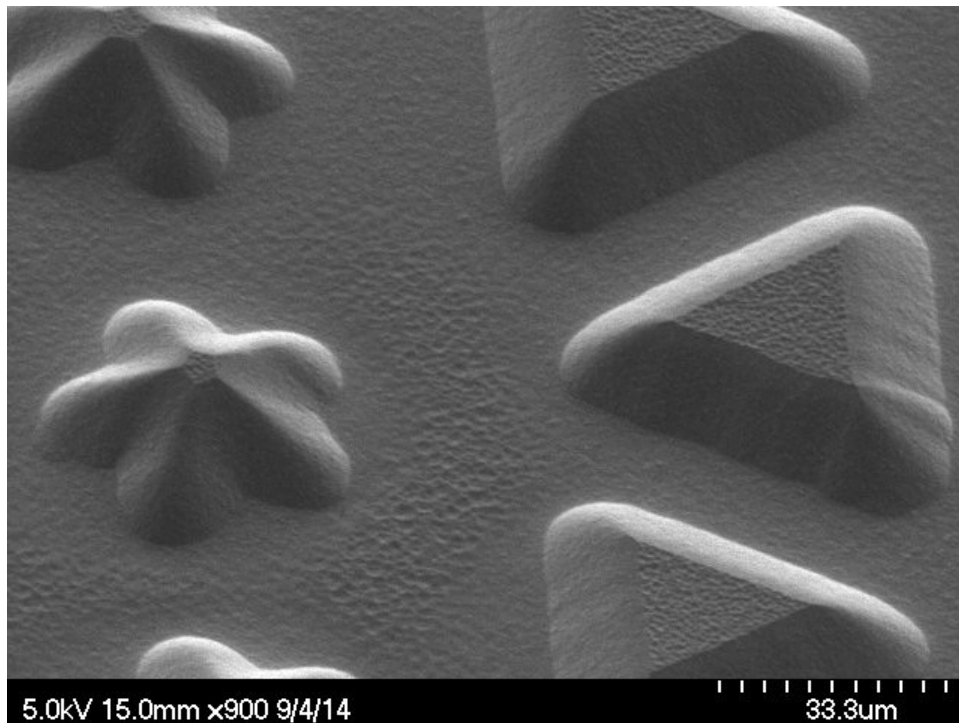
Figure 49. Detail of bomarding silicon with Shipley 1827 photoresist for 50 minutes. Notice the rounded edges of the triangles and stars.

To proof that complex patterns can be transferred to a semiconductor substrate we used photoresist as a masking layer. Figure 49 is the result of bombarding a 2.7 μm layer of Shipley 1827 patterned with stars and triangles for 50 minutes at an accelerating voltage of 12 kV (trying to avoid the accumulation of liquid we used the more energetic droplets of experiment 2). The bombarding time has been long enough to remove all the photoresist especially at the edge of the patterns. Despite this the patterns have been imprinted on the Silicon surface. The perimeter of the patterns are rounded due to the tilt in the wall profiles, in this case no liquid accumulated permanently but the Shipley surface probably retained enough charge to deflect the droplets.
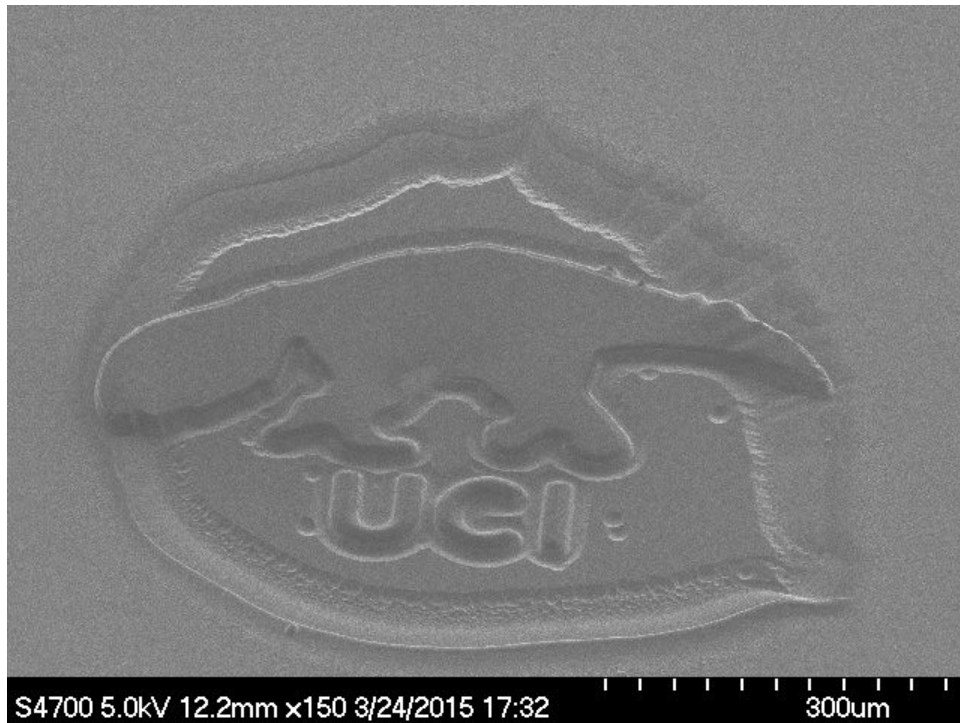
Figure 50. Full beamlet crater, with a pattern of Peter the Anteater, transferred with a mask of 12.5μm of AZ4620. The target has been bombarded for 15 minutes at 17 kV.

We also tested a thicker photoresist (AZ4620) to transfer features onto the substrate, at low voltages the liquid accumulated heavily on the surface and the etch could not continue. Figure 50 shows how an intricate pattern such the silhouette of UCI mascot Peter the Anteater can effectively be carved by electrospray bombardment and a photoresist mask. To avoid the excess of liquid the acceleration voltage is increased at 17 kv

V.3 Conclusions

During this chapter we proved the ability of electrospray sputtering to carve microstructures when combined with protective masks.

A summary of the essential results is:

- The use of electrically non-conductive masks such as Shipley 1827 photoresist results in a virtually infinite selectivity between substrate and mask at the cost of non-perpendicular feature profiles and limited time of continuous operation.

- The alternative conductive masks such as gold prevent the deposition of debris avoiding its related disadvantages. The selectivity for gold when used as a mask on a silicon substrate is 64.17, 13.51, 9.54 and 6.83 for accelerating voltages of 12, 16, 20 and 24kV.

- Intricate patterns can be imprinted on a semiconductor substrate using electrospray bombardment.

The etching rate is not a monotonic function of the accelerating voltage. The ratio between materials etching rates increases with higher accelerating voltages [12]; further works will focus on the research of conductive masks that provide optimal selectivity for

different electrospraying modes and accelerating voltages. The photoresist and gold masks will be used to establish experimentally maximum depth and selectivity when carving structures on SiC and GaN.

The use of a multi-emitter electrospray source to increase the bombarded surface combined with the present work will provide a process suitable for industrial applications, reducing the manufacturing time and expanding the range of semiconductors available to be used in microelectromechanical systems

Bibliography

[1] J. Zeleny, "The Electrical Discharge from Liquid Points, and a Hydrostatic Method of Measuring the Electric Intensity at Their Surfaces," *Phys. Rev.*, vol. 3, no. 2, pp. 69–91, Feb. 1914.

[2] J. Zeleny, "Instability of Electrified Liquid Surfaces," *Phys. Rev.*, vol. 10, no. 1, pp. 1–6, Jul. 1917.

[3] B. Vonnegut and R. L. Neubauer, "Production of monodisperse liquid particles by electrical atomization," *J. Colloid Sci.*, vol. 7, no. 6, pp. 616–622, Dec. 1952.

[4] G. Taylor, "Disintegration of Water Drops in an Electric Field," *Proc. R. Soc. A Math. Phys. Eng. Sci.*, vol. 280, no. 1382, pp. 383–397, 1964.

[5] C. D. Hendricks, "Charged droplet experiments," *J. Colloid Sci.*, vol. 17, no. 3, pp. 249–259, 1962.

[6] J. C. Beynon, E. Cohen, D. S. Goldin, M. N. Huberman, P. W. Kidd, and S. Zafran, "Present status of colloid microthruster technology.," *J. Spacecr. Rockets*, vol. 5, no. 11, pp. 1319–1324, Nov. 1968.

[7] J. B. Fenn, M. Mann, C. K. Meng, S. F. Wong, and C. M. Whitehouse, "Electrospray ionization for mass spectrometry of large biomolecules.," *Science (80-.).*, vol. 246, no. 4926, pp. 64–71, 1989.

[8] I. G. Loscertales, A. Barrero, I. Guerrero, R. Cortijo, M. Marquez, and A. M. Gañán-Calvo, "Micro/nano encapsulation via electrified coaxial liquid jets.," *Science*, vol. 295, no. 5560, pp. 1695–1698, 2002.

[9] D. C. Kyritsis, S. Roychoudhury, C. S. McEnally, L. D. Pfefferle, and A. Gomez, "Mesoscale combustion: A first step towards liquid fueled batteries," *Exp. Therm. Fluid Sci.*, vol. 28, no. 7, pp. 763–770, 2004.

[10] M. Gamero-Castao and M. Mahadevan, "Sputtering yields of Si, SiC, and B4 C under nanodroplet bombardment at normal incidence," *J. Appl. Phys.*, vol. 106, no. 5, 2009.

[11] M. Gamero-Castaño and M. Mahadevan, "Sputtering of silicon by a beamlet of electrosprayed nanodroplets," *Appl. Surf. Sci.*, vol. 255, no. 20, pp. 8556–8561, 2009.

[12] R. Borrajo-Pelaez, E. Grustan-Gutierrez, and M. Gamero-Castaño, "Sputtering of Si, SiC, InAs, InP, Ge, GaAs, GaSb, and GaN by electrosprayed nanodroplets," *J. Appl. Phys.*, vol. 114, no. 18, 2013.

[13] M. Gamero-Castaño, A. Torrents, L. Valdevit, and J. G. Zheng, "Pressure-induced amorphization in silicon caused by the impact of electrosprayed nanodroplets," *Phys. Rev. Lett.*, vol. 105, no. 14, pp. 1–4, 2010.

[14] A. L. Yarin, S. Koombhongse, and D. H. Reneker, "Bending instability in electrospinning of nanofibers," *J. Appl. Phys.*, vol. 89, no. 5, pp. 3018–3026, 2001.

[15] D. Li and Y. Xia, "Electrospinning of nanofibers: Reinventing the wheel?," *Advanced Materials*, vol. 16, no. 14. pp. 1151–1170, 2004.

[16] I. G. Loscertales, A. Barrero, M. Marquez, M. Márquez, R. Spretz, R. Velarde-Ortiz, and G. Larsen, "Electrically forced coaxial nanojets for one-step hollow nanofiber design," *J. Am. Chem. Soc.*, vol. 126, no. 17, pp. 5376–5377, May 2004.

[17] M. Martínez-Sánchez, J. Fernández de la Mora, V. Hruby, M. Gamero-Castaño, and V. Khayms, "Research on Colloid Thrusters," in *The 26th International Electric Propulsion Conference*, 1999, pp. 93–100.

[18] M. Gamero-Castaño, "Characterization of a Six-Emitter Colloid Thruster Using a Torsional Balance," *J. Propuls. Power*, vol. 20, no. 4, pp. 736–741, 2004.

[19] R. Krpoun, M. Räber, and H. R. Shea, "Microfabrication and test of an integrated colloid thruster," in *Proceedings of the IEEE International Conference on Micro Electro Mechanical Systems (MEMS)*, 2008, pp. 964–967.

[20] B. Gassend, L. F. Velasquez-Garcia, A. I. Akinwande, and M. Martinez-Sanchez, "A microfabricated planar electrospray array ionic liquid ion source with integrated extractor," *J. Microelectromechanical Syst.*, vol. 18, no. 3, pp. 679–694, 2009.

[21] G. Lenguito, J. Fernandez de la Mora, and A. Gomez, "Scaling up the power of an electrospray microthruster," *J. Micromechanics Microengineering*, vol. 24, no. 5, p. 055003, 2014.

[22] S. Dandavino, Ç. Ataman, C. Ryan, S. Chakraborty, D. G. Courtney, J. P. W. Stark, and H. R. Shea, "Microfabricated electrospray emitter arrays with integrated extractor and accelerator electrodes for the propulsion of small spacecraft," *J. Micromechanics Microengineering*, vol. 24, no. 7, p. 075011, 2014.

[23] W. Deng, J. F. Klemic, X. Li, M. A. Reed, and A. Gomez, "Liquid fuel microcombustor using microfabricated multiplexed electrospray sources," *Proc. Combust. Inst.*, vol. 31, no. 2, pp. 2239–2246, Jan. 2007.

[24] A. Gomez, D. Bingham, L. d. Juan, and K. Tang, "Production of protein nanoparticles by electrospray drying," *J. Aerosol Sci.*, vol. 29, no. 5–6, pp. 561–574, Jun. 1998.

[25] Q. An, S. N. Luo, W. A. Goddard, W. Z. Han, B. Arman, and W. L. Johnson, "Synthesis of single-component metallic glasses by thermal spray of nanodroplets on amorphous substrates," *Appl. Phys. Lett.*, vol. 100, no. 4, 2012.

[26] I. Lenggoro, K. Okuyama, and J. de la Mora, "Preparation of ZnS nanoparticles by electrospray pyrolysis," vol. 31, no. 1, pp. 121–136, 2000.

[27] B. R. Saunders and M. L. Turner, "Nanoparticle-polymer photovoltaic cells," *Advances in Colloid and Interface Science*, vol. 138, no. 1. pp. 1–23, 2008.

[28] H. Amano, N. Sawaki, I. Akasaki, and Y. Toyoda, "Metalorganic vapor phase epitaxial growth of a high quality GaN film using an AlN buffer layer," *Appl. Phys. Lett.*, 1986.

[29] H. Amano, M. Kito, K. Hiramatsu, and I. Akasaki, " P-Type Conduction in Mg-Doped GaN Treated with Low-Energy Electron Beam Irradiation (LEEBI) ," *Jpn. J. Appl. Phys.*, vol. 28, no. Part 2, No. 12, pp. L2112–L2114, 1989.

[30] S. Round, M. Heldwein, J. Kolar, I. Hofsajer, and P. Friedrichs, "A SiC JFET driver for a 5 kW, 150 kHz three-phase PWM converter," in *Conference Record - IAS Annual Meeting (IEEE Industry Applications Society) (2005)*, 2005, vol. 1, pp. 410–416.

[31] S. Binari, P. Klein, and T. Kazior, "Trapping effects in GaN and SiC microwave FETs," *Proc. IEEE*, 2002.

[32] C. Baack, G. Elze, and G. Walf, "GaAs MESFET: A high-speed optical detector," *Electron. Lett.*, 1977.

[33] T. Mimura, "The early history of the high electron mobility transistor (HEMT)," *IEEE Trans. Microw. Theory Tech.*, vol. 50, no. 3, pp. 780–782, Mar. 2002.

[34] A. Dadgar, A. Alam, T. Riemann, J. Bläsing, A. Diez, M. Poschenrieder, M. Strassburg, M. Heuken, J. Christen, and A. Krost, "Crack-Free InGaN/GaN Light Emitters on Si(111)," *Phys. status solidi*, vol. 188, no. 1, pp. 155–158, Nov. 2001.

[35] A. B. Goulakov, F. Zhao, I. Perez-Wurfl, J. T. Torvik, and B. Van Zeghbroeck, "Optimized reactive ion etch process for high performance SiC bipolar junction transistors," *J. Vac. Sci. Technol. A Vacuum, Surfaces, Film.*, vol. 25, no. 4, p. 961, 2007.

[36] L. Jiang, N. O. V. Plank, M. a. Blaw, R. Cheung, and E. van der Drift, "Dry etching of SiC in inductively coupled Cl2/Ar plasma," vol. 1809, 2004.

[37] S. A. Smith, C. A. Wolden, M. D. Bremser, A. D. Hanser, R. F. Davis, and W. V. Lampert, "Selective and non-selective etching of GaN, AlGaN, and AlN using an inductively

coupled plasma," *Compd. Semicond. 1997. Proc. IEEE Twenty-Fourth Int. Symp. Compd. Semicond.*, vol. 3631, no. 1997, pp. 23–26, 1998.

[38] D. S. Rawal, H. Arora, B. K. Sehgal, and R. Muralidharan, "Comparative study of GaN mesa etch characteristics in Cl2 based inductively coupled plasma with Ar and BCl3 as additive gases," *J. Vac. Sci. Technol. A Vacuum, Surfaces, Film.*, vol. 32, no. 3, p. 031301, 2014.

[39] P. Sigmund, "Theory of sputtering. I. Sputtering yield of amorphous and polycrystalline targets," *Phys. Rev.*, vol. 184, no. 2, pp. 383–416, 1969.

[40] T. Aoki, J. Matsuo, Z. Insepov, and I. Yamada, "Molecular dynamics simulation of damage formation by cluster ion impact," *Nucl. Instruments Methods Phys. Res. Sect. B Beam Interact. with Mater. Atoms*, vol. 121, no. 1–4, pp. 49–52, 1997.

[41] F. Saiz and M. Gamero-Castaño, "Atomistic modeling of the sputtering of silicon by electrosprayed nanodroplets," *J. Appl. Phys.*, vol. 116, no. 5, p. 054303, 2014.

[42] C. D. Child, "Discharge from hot cao," *Phys. Rev. (Series I)*, vol. 32, no. 5, pp. 492–511, 1911.

[43] V. Cimalla, J. Pezoldt, and O. Ambacher, "Group III nitride and SiC based MEMS and NEMS: materials properties, technology and applications," *J. Phys. D. Appl. Phys.*, vol. 40, no. 20, pp. 6386–6434, 2007.

[44] I. Yamada and N. Toyoda, "Nano-scale surface modification using gas cluster ion beams - A development history and review of the Japanese nano-technology program," *Surf. Coatings Technol.*, vol. 201, no. 19–20 SPEC. ISS., pp. 8579–8587, 2007.

[45] J. Fernández de la Mora, "The fluid dynamics of Taylor cones," *Annu. Rev. Fluid Mech.*, vol. 39, pp. 217–243, 2007.

[46] M. Cloupeau and B. Prunet-Foch, "Electrostatic spraying of liquids: Main functioning modes," *J. Electrostat.*, vol. 25, no. 2, pp. 165–184, 1990.

[47] M. Cloupeau and B. Prunet-Foch, "Electrohydrodynamic spraying functioning modes: a critical review," *Journal of Aerosol Science*, vol. 25, no. 6. pp. 1021–1036, 1994.

[48] M. Cloupeau and B. Prunet-Foch, "Electrostatic spraying of liquids in cone-jet mode," *Journal of Electrostatics*, vol. 22, no. 2. pp. 135–159, 1989.

[49] B. A. Thomson and J. V Iribarne, "Field induced ion evaporation from liquid surfaces at atmospheric pressure," *J. Chem. Phys.*, vol. 71, no. 11, p. 4451, 1979.

[50] I. G. Loscertales and J. Fernández de la Mora, "Experiments on the kinetics of field evaporation of small ions from droplets," *J. Chem. Phys.*, vol. 103, no. 12, p. 5041, 1995.

[51] M. Gamero-Castano and J. de la Mora, "Kinetics of small ion evaporation from the charge and mass distribution of multiply charged clusters in electrosprays," vol. 35, no. 7, pp. 790–803, 2000.

[52] M. Gabovich, "Liquid-metal ion emitters," *Physics-Uspekhi*, 1983.

[53] I. Romero-Sanz, R. Bocanegra, J. Fernandez de la Mora, and M. Gamero-Castaño, "Source of heavy molecular ions based on Taylor cones of ionic liquids operating in the pure ion evaporation regime," *J. Appl. Phys.*, vol. 94, no. 5, pp. 3599–3605, 2003.

[54] Lord Rayleigh, "XX. On the equilibrium of liquid conducting masses charged with electricity," *Philos. Mag. Ser. 5*, vol. 14, no. 87, pp. 184–186, Apr. 1882.

[55] G. Taylor, "Studies in Electrohydrodynamics. I. The Circulation Produced in a Drop by Electrical Field," *Proceedings of the Royal Society A: Mathematical, Physical and Engineering Sciences*, vol. 291, no. 1425. pp. 159–166, 1966.

[56] J. R. Melcher and G. I. Taylor, "Electrohydrodynamics: A Review of the Role of Interfacial Shear Stresses," *Annual Review of Fluid Mechanics*, vol. 1, no. 1. pp. 111–146, 1969.

[57] D. A. Saville, "ELECTROHYDRODYNAMICS:The Taylor-Melcher Leaky Dielectric Model," *Annual Review of Fluid Mechanics*, vol. 29, no. 1. pp. 27–64, 1997.

[58] F. J. Higuera, "Flow rate and electric current emitted by a Taylor cone," *J. Fluid Mech.*, vol. 484, pp. 303–327, 2003.

[59] F. Higuera, "Current/flow-rate characteristic of an electrospray with a small meniscus," *J. Fluid Mech.*, 2004.

[60] J. Fernández de la Mora and I. G. Loscertales, "The current emitted by highly conducting Taylor cones," *J. Fluid Mech.*, vol. 260, no. -1, p. 155, 1994.

[61] A. Ganan-Calvo, J. Davila, and A. Barrero, "Current and droplet size in the electrospraying of liquids. Scaling laws," *J. Aerosol Sci.*, 1997.

[62] L. F. Velásquez García, "A Microfabricated Colloid Thruster," MIT, 2001.

[63] H. Jansen, M. De Boer, R. Legtenberg, and M. Elwenspoek, "The black silicon method: a universal method for determining the parameter setting of a fluorine-based reactive ion etcher in deep silicon trench etching with profile control," *J. Micromechanics Microengineering*, vol. 5, no. 2, pp. 115–120, 1999.

[64] P. Dixit and J. Miao, "High Aspect Ratio Vertical Through-Vias for 3D MEMS Packaging Applications by Optimized Three-Step Deep RIE," *J. Electrochem. Soc.*, vol. 155, no. 2, p. H85, 2008.

[65] A. A. Ayón, R. Braff, C. C. Lin, H. H. Sawin, and M. A. Scmidt, "Characterization of a Time Multiplexed Inductively Coupled Plasma Etcher," *J. Electrochem. Soc.*, vol. 146, no. 1, p. 339, 1999.

[66] H. C. Liu, Y. H. Lin, and W. Hsu, "Sidewall roughness control in advanced silicon etch process," *Microsyst. Technol.*, vol. 10, no. 1, pp. 29–34, 2003.

[67] V. Kaajakari, *Practical MEMS: Design of microsystems, accelerometers, gyroscopes, RF MEMS, optical MEMS, and microfluidic systems*. 2009.

[68] R. Krpoun and H. R. Shea, "Integrated out-of-plane nanoelectrospray thruster arrays for spacecraft propulsion," *J. Micromechanics Microengineering*, vol. 19, no. 4, p. 045019, 2009.

[69] G. Lenguito and A. Gomez, "Development of a multiplexed electrospray micro-thruster with post-acceleration and beam containment," *J. Appl. Phys.*, vol. 114, no. 15, p. 154901, Oct. 2013.

[70] R. Krpoun, K. L. Smith, J. P. W. Stark, and H. R. Shea, "Tailoring the hydraulic impedance of out-of-plane micromachined electrospray sources with integrated electrodes," *Appl. Phys. Lett.*, vol. 94, no. 16, pp. 5–7, 2009.

[71] R. Krpoun, "Micromachined Electrospray Thrusters for Spacecraft Propulsion," vol. 4255, p. 144, 2009.

[72] S. Dandavino, Ç. Ataman, S. Chakraborty, H. R. Shea, C. Ryan, and J. P. W. Stark, "Design and fabrication of the thruster heads for the MicroThrust MEMS electrospray propulsion system," in *33rd International Electric Propulsion Conference*, 2013, pp. 1–8.

[73] N. Nguyen and S. Wereley, *Fundamentals and applications of microfluidics*. 2002.

[74] A. B. McEwen, "Electrochemical Properties of Imidazolium Salt Electrolytes for Electrochemical Capacitor Applications," *J. Electrochem. Soc.*, vol. 146, no. 5, p. 1687, 1999.

[75] M. Gamero-Castaño, "Characterization of the electrosprays of 1-ethyl-3-methylimidazolium bis(trifluoromethylsulfonyl) imide in vacuum," *Phys. Fluids*, vol. 20, no. 3, pp. 1–11, 2008.

[76] N. Winograd, Z. Postawa, J. Cheng, C. Szakal, J. Kozole, and B. J. Garrison, "Improvements in SIMS continue. Is the end in sight?," *Appl. Surf. Sci.*, vol. 252, no. 19, pp. 6836–6843, 2006.

[77] J. Samela and K. Nordlund, "Atomistic simulation of the transition from atomistic to macroscopic cratering," *Phys. Rev. Lett.*, 2008.

[78] F. Saiz and M. Gamero-Castano, "Amorphization of silicon induced by nanodroplet impact: A molecular dynamics study," *J. Appl. Phys.*, 2012.

[79] M. Gamero-Castaño, "Induction charge detector with multiple sensing stages," *Rev. Sci. Instrum.*, 2007.

[80] Y. Yamamura and H. Tawara, "Energy dependence of ion-induced sputtering yields from monatomic solids at normal incidence," *At. data Nucl. data tables*, 1996.

[81] T. S. Pugacheva, F. G. Jurabekova, Y. Miyagawa, and S. K. Valiev, "Computer simulation of SiC and B4C sputtering by Ar+ and He+ ions bombardment," *Nucl. Instruments Methods Phys. Res. Sect. B Beam Interact. with Mater. Atoms*, vol. 127–128, pp. 260–264, 1997.

[82] I. Yamada, "Low-energy cluster ion beam modification of surfaces," *Nucl. Instruments Methods Phys. Res. Sect. B Beam Interact. with Mater. Atoms*, vol. 148, no. 1–4, pp. 1–11, 1999.

[83] F. Saiz, R. Borrajo-Pelaez, and M. Gamero-Castaño, "The influence of the projectile's velocity and diameter on the amorphization of silicon by electrosprayed nanodroplets," *J. Appl. Phys.*, 2013.

[84] L. Ma, K. F. Adeni, C. Zeng, Y. Jin, K. Dandu, Y. Saripalli, and D. Barlage, "Comparison of Different GaN Etching Techniques," *CS MANTECH Conf.*, pp. 105–108, 2006.

[85] D. Gao, R. T. Howe, and R. Maboudian, "High-selectivity etching of polycrystalline 3C-SiC films using HBr-based transformer coupled plasma," *Appl. Phys. Lett.*, vol. 82, no. 11, pp. 1742–1744, 2003.

[86] M. Lazar, H. Vang, P. Brosselard, C. Raynaud, P. Cremillieu, J. L. Leclercq, a. Descamps, S. Scharnholz, and D. Planson, "Deep SiC etching with RIE," *Superlattices Microstruct.*, vol. 40, no. 4–6 SPEC. ISS., pp. 388–392, 2006.

[87] J.-M. Lee, K.-M. Chang, I.-H. Lee, and S.-J. Park, "Cl[sub 2]-Based Dry Etching of GaN and InGaN Using Inductively Coupled Plasma The Effects of Gas Additives," *J. Electrochem. Soc.*, vol. 147, no. 5, p. 1859, 2000.

[88] S. Zhou, B. Cao, and S. Liu, "Dry etching characteristics of GaN using Cl2/BCl3 inductively coupled plasmas," *Appl. Surf. Sci.*, vol. 257, no. 3, pp. 905–910, 2010.

[89] J. Hong, R. J. Shul, L. Zhang, L. F. Lester, H. Cho, Y. B. Hahn, D. C. Hays, K. B. Jung, S. J. Pearton, C.-M. Zetterling, and M. Östling, "Plasma chemistries for high density plasma etching of SiC," *J. Electron. Mater.*, vol. 28, no. 3, pp. 196–201, 1999.

Appendix A

Summary of recipe analysis for large aspect ratio emitters

Name	Characteristics	Process time	Depth	Results
Process A	No changes	120'		Over-etch (broken emitters)
Process A (1)	7" etch 7"pass	120'		Broken emitters
Process A (2)	6"/7" etch/pass	120'		Silicon grass
Process A2	Platen etch power 15W – 12W	1h 10' at 15W 2h 10' at 12W		Silicon grass
Process Ai	Platen etch power 15W – 12W	1h 30' at 12W 1h 30' at 15W	160-194 µm	Silicon grass
Process Miao	See [30]	90'		Broken emitters
Process Ams	Platen etch 12W 8"/6" etch/pass	160'	300-330 µm	Broken emitters
Process Ams 10	Platen etch 10W 8"/6" etch/pass	90'	120-190 µm	OK
Process A3s	Platen etch: 10W, 11W, 12 W 8"/6" etch/pass	30' at 10W 50' at 11W 80' at 12W	200-320 µm	Silicon grass and broken emitters. High variability
Switching processes (2 runs)	Process A: - Etch/pass: 8"/7" - Platen: 10W, 12W, 15W Process B	30' Process A at 10 W 10' Process A at 12 W 12' Process B 17' Process A at 12 W 12' Process B 20' Process A at 15 W 7' Process B 20' Process A at 15 W 12' Process B 20' Process A at 15 W	290-310 µm	Heavy presence silicon grass. Difficult control of the etching rate
Process A-Ar	6 sccm of Ar during etching	1h	100 µm	OK

Process A-Ar	6 sccm of Ar during etching	2h	200 µm	Broken emitters
Process A-Ar (15)	6 sccm of Ar, 15 sccm C4F8 during etching	2h		Silicon grass
Process A-Ar (10)	6 sccm of Ar, 10 sccm C4F8 during etching	2h		Silicon grass
Process A-Ar (5)	6 sccm of Ar, 5 sccm C4F8 during etching	2h		Silicon grass
Process A-Ar (2)	6 sccm of Ar, 2 sccm C4F8 during etching	2h	200 µm	Broken emitters. Flux of C4F8 not stable
Process A-Ar 2 st	6 sccm of Ar, 5 sccm C4F8 during etching Etch/pass 8"/4"-8"/5"	1h at 8"/4" 30' at 8"/5"	150 µm	Broken emitters
Process A-Ar 2 st	6 sccm of Ar, 5 sccm C4F8 during etching Etch/pass 8"/4"-8"/4.5"	1h at 8"/4" 30' at 8"/4.5"	150 µm	Broken emitters
Process A-Ar 5 st	6 sccm of Ar	50' of Process A-Ar 35' of Process A-Ar(5) 35' of Process A-Ar(5) at 8"/4.9" ratio 30' of Process A-Ar (5) at 8"/4.7" ratio 30' of Process A-Ar(5) at 8"/4.6" ratio	290 µm	Broken emitters and silicon grass
ProcessA-Ar 12W	6 sccm of Ar Platen etch 15 -12W	1h 15W 1h 12W	200 µm	Silicon grass
ProcessA-Ar APC	Process A-Ar APC 89º	2h	200 µm	Broken emitters